

**MULTIDIAGNOSTIC CHARACTERIZATION
OF ULTRASHORT AND SHORT PULSE
LASER PRODUCED PLASMA FROM
ALUMINIUM AND TUNGSTEN TARGETS**

Thesis

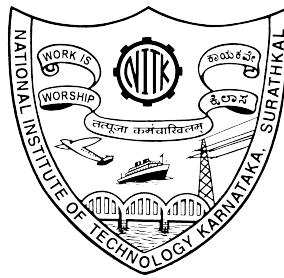
submitted in partial fulfillment of the requirements for the degree

of

DOCTOR OF PHILOSOPHY

by

PRANITHA SANKAR



DEPARTMENT OF PHYSICS

NATIONAL INSTITUTE OF TECHNOLOGY KARNATAKA,

SURATHKAL, MANGALORE-575025

October 2019

DECLARATION

(By the Ph.D. Research Scholar)

I hereby declare that the research thesis entitled “*Multidiagnostic Characterization of Ultrashort and Short Pulse Laser Produced Plasma from Aluminium and Tungsten Targets*” which is being submitted to the National Institute of Technology (NIT) Karnataka, Surathkal in partial fulfillment of the requirements for the award of the Degree of Doctor of Philosophy in Physics is a bonafide report of the research work carried out by me. The material contained in this Research Thesis has not been submitted to any University or Institution for the award of any degree.

Place: NITK, Surathkal

Date:

Pranitha Sankar

(Register No. 155020PH15P02)

Department of Physics,

NITK, Surathkal

CERTIFICATE

This is to certify that the Research thesis entitled “**Multidiagnostic characterization of ultrashort and short pulse laser produced plasma from aluminium and tungsten targets**” submitted by **Pranitha Sankar** (Register Number: **155020 PH15P02**) as the record of the research work carried out by her, is accepted as the research thesis submission in partial fulfilment of the requirements for the award of the degree of Doctor of Philosophy.

Research Supervisors

Dr. H. D. Shashikala

Professor

Dept. of Physics

NITK, Surathkal

Karnataka

Date:_____

Dr. Reji Philip

Professor

LAMP group

Raman Research Institute

Bangalore

Date:_____

ABSTRACT

The field of laser produced plasmas (LPP) has greatly attracted the research community because of its wide range of applications such as pulsed laser deposition, generation of light sources and ion beams, plasma-based acceleration etc. The present thesis reports space and time-resolved comparative studies of ultrashort and short laser pulse produced plasmas from Aluminium (Al) and Tungsten (W) targets at different ambient pressures.

The thesis starts with a brief introduction to LPPs and their fundamental properties. Experimental techniques used and instruments employed are described in the second chapter. The chapters that follow discuss results obtained from optical time of flight (OTOF), optical emission spectroscopy (OES), time-resolved ICCD imaging and ion dynamics studies of plasmas generated in the targets, irradiated by ultrashort (100 femtoseconds) and short (7 nanoseconds) laser pulses, in air ambient with pressures ranging from 10^{-5} to 760 Torr. Electron temperature and number density of the plasma have been calculated from optical emission spectra. The intensities of the plasma plumes, as well as the corresponding neutrals to ions ratios, are found to be different between ultrashort laser ablation (ULA) and short laser ablation (SLA) because of the relative differences in laser-matter and laser-plasma interactions. OTOF measurements, time-resolved ICCD imaging and Ion emission measurements reveal the presence of both fast moving as well as slow-moving species in SLA, while this distinction is not so obvious in ULA. Linear, shock wave and drag models are used to model plume and ion dynamics in the low, intermediate and high-pressure regions respectively. In addition, the expansion dynamics of the ULA aluminum plasma is investigated as a function of the laser beam size on the target, using a combination of the above-mentioned diagnostic tools. Optical emission spectroscopic analysis shows that higher emission intensities and ion populations are obtained for smaller beam sizes. Time-resolved ICCD imaging of the expanding plasma shows a spherical morphology for plumes produced by smaller beam sizes, and a cylindrical morphology for those produced by larger beam sizes.

A comprehensive comparison of X-ray emission from ULA and SLA plasmas also has been carried out for Al and W targets. The use of longer wavelengths with longer pulse durations leads to lower critical density LPP, which results in efficient laser-plasma heating. Enhanced X-ray emission can hence be achieved from laser-irradiated Ag and Au nanoparticle colloidal suspensions. A summary of the results and discussion, their significance and future scope are given in the final chapter.

Key words: Laser-produced plasma, Ultrashort laser, X-ray emission, Ambient effects.

Dedicated to my family and teachers...

ACKNOWLEDGEMENTS

*As a student I had never thought of doing a Ph.D., and even in my wildest fantasies I did not expect that one day I would write a doctoral thesis. There have been memorable contributions from many people towards the fulfilment of my research work, and my thesis would not be complete without acknowledging the important roles they played in my endeavour. I don't have words to express my heartfelt gratitude towards my guide **Prof. Reji Philip**. He agreed and took the initiative to provide me with a guideship at NITK, Suratkal. I appreciate all his contributions of time, ideas, and funding to make my Ph.D. experience productive and stimulating. Without your help, I could have not finished my thesis and especially my manuscripts. Sir, you taught me the methods of writing scientific text in English, by rifting through my papers sentence by sentence. I have been privileged to have Prof. Reji as my mentor. I want to thank him not only for being my guide, but also for showering fatherly affection on me, during my stay at RRI.*

*I extend the deepest sense of gratitude to my internal guide, **Prof. H. D. Shashikala**, Department of Physics, NITK, Suratkal for providing me with an opportunity to enrol for my doctoral degree under her supervision. Without her support and cooperation I would not have been able to start my Ph.D. work. I am indebted to her for the priceless suggestions and encouragement throughout the research period. I also wish to thank my other R-PAC committee members, **Dr. Ajith K M** and **Dr. Udaya Kumar Dalimba**, for their extensive support.*

*I came to RRI, first for doing my master project, which turned out to be a fabulous opportunity to start my career as a researcher. I started my research career in ultrafast optics initially as a visiting student, then as a Junior Research Fellow and finally as a Ph.D. student. During these stages, **Dr. N. Smijesh** introduced me to the experiments and he taught me to run the lasers and other major instruments in the lab. **Dr. Jijil J. J Nivas** was the best companion for me during experiments and he taught me the alignment of optical components. I have to appreciate him for the patience! I owe my thanks to **Muhammed Shafi Ollakkan**, who always helped me to troubleshoot the*

*failures during the experiments. I would like to express my special appreciation and thanks to **Dr. Anoop K. K**, former Research Associate at RRI, who helped me when I started my Ph.D. work. I cannot forget the support and care from **Dr. T. Priya Rose** who was a former research associate at RRI. These are the main pillars responsible for the growth of my career!*

I gratefully acknowledge two person, Dr. M. Sreejesh M and Mr. T. C. Sunilkumar for sending me a timely mail regarding Ph.D. admission at NITK. If not for them, I would not have been a Ph.D. student in India. I extend my thanks to Dr. K. P. Sibin for helping me throughout the Ph.D. programme. I am grateful to many others at NITK for making life easier; nice stay, delicious seafood and evening walk through the beach have been memorable. I remember Nimith, Rajani, Manju, Safir, Sterin, Sruthy, Anjana and many more with gratitude.

The members of the ultrafast and nonlinear optics lab at RRI have contributed immensely to my personal and professional growth. The group has been a source of friendships as well as good advice and collaboration. I am especially grateful for Anitta Rose, Gaurav K Tiwari, Agnes George, Anjali V Murali, Jyothis Thomas, Joel K Jose, Subam Rai, Nancy Verma, Nithin Joy, and Arjun K. K., who helped me in the work some way or other. I have to express my sincere gratitude to Jyothis and Joel as they were my project students from CUSAT. I thank my former lab mates in RRI, Dr. Suchand Sandeep, Dr. Jinto Thomas, Dr. Kishore Sreedharan, Dr. Binoy K Anand, Dr. Ann Mary, Dr. Nivya Roy, Dr. Tintu Kuriakose, Dr. Sreekanth Perumbilavil, Ms. Sarayoo Sasidharan, and Ms. Elizabeth, Kavya, Amrutha, Beryl, Priya, Hareesh, Sreelakshi, Aparna, Dhanya Teacher, Ajay, Dhibyaree, Ashley, Kiran, Anusree, Shahala, Alina and others.

I am grateful for the time spent with my room mates Anitta and Vrinda and my special thanks to Nidhin for his critical comments and suggestions during the thesis work. I would like to express my special thanks to them for being great soul mates. They were always ready to help me with a smile. And these people have made adorable changes in my personal and professional life.

I have had many close friends in Bangalore and every weekend was spectacular because of them. I would like to extend my thanks to Alfred, Sunilkumar, Suraj, Prajith, Shafeer, Praveen, Ajilesh, Arya, Silpa, Stella, Neethu, Shimna, Rohith Balakrishnan, Paul, Aravind, Elsu, Remya, Sherin, Prasanth, Arun, Rohith, Nandhini, Sanal, Hari, Aswathi and many more. They were my backpacking buddies and thank you so much for sharing the experience of trekking to many wonderful places.

Last but not the least, I would like to dedicate this thesis to my husband Jayasankar C B, my parents, and my sister. I am at a loss of words to thank you enough for the wonderful support and help in all matters pertaining to my Ph.D. programme. The love and encouragement you provided are beyond description. I extend my thanks to my husband's family too. Special thanks to my baby Ishaan Sankar for suffering along with me the hardships of finalizing and submitting the thesis.

In a nutshell, without you all, I could not have finished my thesis in time. I will indeed remember this precious period forever. Above all, I owe it to Almighty God for granting me the wisdom, health, and strength to undertake this voluminous task and enabling me to bring it to a successful completion.

Pranitha Sankar

Contents

ABSTRACT	i
LIST OF FIGURES	x
LIST OF TABLES	xix
NOMENCLATURE	xx
1 LASER-PRODUCED PLASMAS:	
AN INTRODUCTION	1
1.1 Laser-Produced Plasma	2
1.1.1 Optical field ionization mechanism	5
1.1.2 Timescales in plasma formation	7
1.1.3 Atomic process in a plasma	13
1.1.3.1 Absorption mechanisms	13
1.1.3.2 Emission mechanisms	16
1.1.4 Hot electrons and X-rays from laser produced plasma	18
1.2 The scope of the thesis	19
1.3 Objectives of the thesis	20
1.4 Outline of the thesis	21
2 EXPERIMENTAL TECHNIQUES AND INSTRUMENTATION	23
2.1 Introduction	24
2.2 Ultrashort pulse laser source	24

2.2.1	The ultrafast oscillator	25
2.2.2	The ultrafast amplifier	27
2.3	Short pulse laser source	28
2.4	Experimental environment	30
2.4.1	Vacuum chamber	30
2.4.2	Dry pump and Turbo Molecular Pump (TMP)	30
2.4.3	Solid target manipulator and Target motion controller	31
2.5	Detectors	32
2.5.1	Spectrometer	32
2.5.2	Digital Phosphor Oscilloscope	33
2.5.3	Intensified charge coupled device (ICCD) detector	33
2.5.4	Faraday Cup	34
2.5.5	X-ray detector	35
2.6	Laser pulse characterization	36
2.6.1	Spectral characteristics	36
2.6.2	Spatial intensity profile of the laser pulse (knife edge method)	37
2.6.3	Spatial intensity profile of the laser pulse (beam imaging)	37
2.7	Optical Emission Spectroscopy (OES)	39
2.7.1	Calculating the electron temperature (T_e)	39
2.7.2	Calculating the electron number density (N_e)	40
2.8	Optical time of flight measurements (OTOF)	41
2.9	ICCD Imaging Technique	42
2.10	Ion Time of flight studies	43
2.11	X-ray measurements	44
2.12	Experimental set up at a glance	45
2.13	Summary	47

3	LASER PRODUCED PLASMA FROM ALUMINIUM AT DIFFERENT AMBIENT PRESSURE	49
3.1	Introduction	50
3.2	Results and Discussion	51
3.2.1	Optical Emission Spectroscopy (OES)	51
3.2.2	Time of Flight Studies	59
3.3	Summary	67
4	ION DYNAMICS OF LASER PRODUCED ALUMINIUM PLASMA AT DIFFERENT AMBIENT PRESSURE	69
4.1	Introduction	70
4.2	Experimental setup	71
4.3	Results and Discussion	72
4.4	Summary	85
5	EFFECT OF LASER BEAM SIZE ON THE DYNAMICS OF ULTRA-SHORT LASER PRODUCED ALUMINIUM PLASMA IN VACUUM	87
5.1	Introduction	88
5.2	Experimental setup	89
5.3	Results and Discussion	91
5.4	Summary	99
6	MULTIDIAGNOSTIC ANALYSIS OF TUNGSTEN PLASMAS GENERATED BY ULTRASHORT AND SHORT LASER PULSES	101
6.1	Introduction	102
6.2	Results and discussion	104
6.2.1	Optical Emission Spectroscopy (OES)	104

6.2.2	Ion time of flight (TOF) measurements	112
6.2.3	Surface structure analysis	114
6.3	Summary	115
7	STUDY OF X-RAY EMISSION FROM LASER PRODUCED PLASMAS	117
7.1	Introduction	118
7.2	Experimental setup	119
7.3	Calibration of X-ray detector	121
7.4	X-ray emission from solid targets	122
7.4.1	X-ray emission from Aluminium	123
7.4.2	X-ray emission from Tungsten (W)	125
7.5	X-ray emission from liquid targets	126
7.5.1	X-ray emission from a water jet	126
7.5.2	X-ray emission from silver and gold nanoparticle colloidal jets .	127
7.5.2.1	Materials and characterization	127
7.5.2.2	Stability studies of Au and Ag under laser irradiation .	129
7.5.2.3	X-ray emission from Au and Ag nanoparticles	131
7.6	Summary	134
8	CONCLUSIONS AND FUTURE SCOPE	135
	REFERENCES	139
	CURRICULUM VITAE	153

List of Figures

1.1	A schematic illustration of Ultrashort laser ablation (ULA) and Short laser ablation (SLA) [source: https://www.assemblymag.com/articles/93059].	3
1.2	Schematic representation of the ionization regimes. (a) Multiphoton ionization or above-threshold ionization, (b) Tunnelling ionization, (c) Over-the-barrier ionization [source: Suman 2007].	6
1.3	Schematic representation of Ultrashort and Short laser produced plasma formation [source: Harilal et al. 2018].	9
1.4	Pictorial representation of LPP using short (nanosecond) and ultrashort (femtosecond) laser pulses [source: Verhoff et al. 2012].	9
1.5	Schematic diagram of resonance absorption [source: Suman 2007].	16
2.1	Schematic of cavity alignment of Tsunami oscillator with fs configuration.[source: https://www3.nd.edu/~bohnggrp/site/groupfiles/Ti-Sapphire%20Alignment.pdf].	25
2.2	Schematic representation of the CPA scheme [source: https://www.nobelprize.org/uploads/2018/10/popular-physicsprize2018.pdf].	27
2.3	(a) Schematic representation of Nd:YAG laser system, (b) the four-level energy diagram [source: http://www.aml.engineering.columbia.edu/ntm/level1/ch05/html/l1c05s07.html].	29
2.4	(a) Photograph of the iHR320 spectrometer equipped with CCD and PMT detectors. (b) The inner layout of the spectrometer [source: http://www.horiba.com/scientific/products/osd/optical-components/spectrographs-and-monochromators/ihr-series-spectrographs/].	32

2.5	Schematic diagram of an ICCD, and photograph of istar CCD 334 from Andor Technology [source: https://andor.oxinst.com/products/istar-intensified-cameras].	34
2.6	Schematic diagram of an ion probe circuit.	35
2.7	The X-ray spectrometer X-123 CdTe [source: http://amptek.com/products/x-123-cdte-complete-x-ray-gamma-ray-spectrometer-with-cdte-detector/].	35
2.8	Wavelength spectrum of the ultrafast laser pulse.	36
2.9	Actual beam size of ultrashort and short laser pulses measured using the knife-edge method.	37
2.10	Beam size at the focus (focal length of lens 40 cm) for ultrashort and short laser pulses respectively, measured by the knife-edge method. . . .	38
2.11	Horizontal cross-section of the beam at the focus obtained from the beam profiler (a) Ultrashort pulse (100 fs) (b) Short pulse (7 ns).	38
2.12	Profile of the beam obtained using a BeamLux beam profiler (a) Ultrashort pulse (100 fs) (b) Short pulse (7 ns).	39
2.13	Connection diagram of Amptek 123CdTe X-ray Detector [source: http://amptek.com/products/x-123-cdte-complete-x-ray-gamma-ray-spectrometer-with-cdte-detector/].	44
2.14	Calibration spectrum of ^{241}Am [source: http://amptek.com/products/x-123-cdte-complete-x-ray-gamma-ray-spectrometer-with-cdte-detector/].	45
2.15	Schematic of the experimental set up used for optical emission spectroscopy (OES), OTOF spectroscopy, ICCD imaging, Ion studies and X-ray measurements.	47
3.1	Spectra of optical emission from the plasma generated by (a) ultrashort and (b) short laser pulses for $z = 1$ mm. Background pressure is 10 Torr. The net emission intensity is about five times higher for SLA compared to ULA. The 358.7 nm (Al II) and 360.1 nm (Al III) emissions are resolved in the inset shown in the top panel.	52

3.2	Emission intensity of Al I, Al II, and Al III estimated for different distances in the plasma plume from the target surface, from the corresponding emission spectra. The target is ablated using (a) ultrashort and (b) short laser pulses, respectively. Background gas pressure is 10 Torr.	53
3.3	Emission intensity of Al I, Al II, and Al III measured for different background pressures, with (a) ultrashort and (b) short pulse laser ablations respectively, for $z = 1$ mm.	55
3.4	Variation of electron temperature (T_e) and number density (N_e) with axial distance for ULA and SLA measured at 10 Torr.	57
3.5	Variation of electron temperature (T_e) and Number density (N_e) with pressure, measured at a distance of 2 mm from the target surface, for a laser fluence of 70 J/cm^2	59
3.6	Time of flight spectra of Al I, Al II and Al III measured for different axial distances in the plume from the target surface, for (a) ultrashort and (b) short laser pulses. Zero time corresponds to the instant of target irradiation. Background gas pressure is 10 Torr.	61
3.7	Intensity of emission with time for Al species measured at ~ 396 nm, at 1 mm distance from the target surface. The background nitrogen pressure was 10 Torr. Solid lines represent the Shifted Maxwell Boltzmann fit. In the case of SLA the fast peaks fits better to Gaussian function as shown in the inset.	62
3.8	Velocities of atomic and ionic species in (a) ULA and (b) SLA, at different distances in the plasma plume from the target surface, estimated from the TOF data. The species attain relatively higher velocities in SLA compared to ULA. Background gas pressure is 10 Torr.	64
3.9	The peak velocity of Al, Al II and Al III in the plasma plume for (a) ultrashort and (b) short pulse laser ablation for different background pressures. The measurements are carried out at $z = 1$ mm.	65

3.10	Collisionality parameter of the plasma plume at different background pressures. Measurements are carried out at $z = 1$ mm. Mean free path of the background gas is showed in the inset for different background pressures.	66
4.1	ICCD images of the a) ULA expanding plasma plume, and b) its ionic components (Al^{2+}), for varying ambient pressures ranging from 10^5 to 760 Torr. Gate delay of the ICCD is 50 ns, and the gate width is 1000 ns. c) Variation of intensity with ambient pressure for the whole plume and its ionic component. Maximum intensity is observed for the pressure region of 1 Torr to 10 Torr. d) The aspect ratio of the plume (plume length/plume width) measured at various pressures, for 1000 ns ICCD gate width.	73
4.2	ICCD images of the a) SLA expanding plasma plume, and b) its ionic components (obtained using an interference filter), for varying ambient pressures ranging from 10^{-5} to 760 Torr. Gate delay of the ICCD is 50 ns, and the gate width is 1000 ns. c) Variation of intensity with ambient pressure for the whole plume and its ionic component. Maximum intensity is observed for the pressure region of 0.1 Torr to 10 Torr. d) The aspect ratio of the plume (plume length/plume width) measured at various pressures, for 1000 ns ICCD gate width.	74
4.3	Temporal evolution of ultrashort laser produced plasma (ULA) plume from the aluminium target for five different ambient pressures. Images are normalized to their maximum intensity along each row.	76
4.4	Temporal evolution of the ionic components (Al^{2+}) in the ultrashort laser produced plasma (ULA) plume from an aluminium target for five different background pressures. Images are normalized to their maximum intensity along each row.	77
4.5	Temporal evolution of short laser produced plasma (SLA) plume from the aluminium target for five different ambient pressures. Images are normalized to their maximum intensity along each row.	78

4.6	Temporal evolution of the ionic components (Al^{2+}) in the short laser produced plasma (SLA) plume from an aluminium target for five different background pressures. Images are normalized to their maximum intensity along each row.	80
4.7	Position-time plots for the whole ultrashort laser produced plume (ULA) estimated from the gated ICCD images, for the ambient pressure range of 10^{-5} Torr to 760 Torr. Symbols denote measured data points, and dashed curves represent different expansion models. For the shock wave model, $kt = (k/p)^{1/5}$ found to be 0.257 mm/ns ^{0.4} for 10^{-3} Torr, $kt = 0.014$ mm/ns ^{0.4} , for 1 Torr, $kt = 0.002$ mm/ns ^{0.4} for 10 Torr. Fitting parameters for the drag model at 760 Torr are $\beta = 0.078$ ns ⁻¹ and $R_0 = 1.629$ mm, respectively.	81
4.8	Position-time plots for the ultrashort laser produced ions (ULA ions) estimated from the gated ICCD images, for the ambient pressure range of 10^{-5} Torr to 760 Torr. Symbols denote measured data points, and dashed curves represent different expansion models. For the shock wave model, $kt = (k/p)^{1/5}$ found to be 0.01526 mm/ns ^{0.4} for 1 Torr, $kt = 0.008$ mm/ns ^{0.4} , for 10 Torr. Fitting parameters for the drag model at 760 Torr are $\beta = 0.056$ ns ⁻¹ and $R_0 = 1.662$ mm, respectively.	82
4.9	Position-time plots for the whole short laser produced plume (SLA) estimated from the gated ICCD images, for the ambient pressure range of 10^{-5} Torr to 760 Torr. Symbols denote measured data points, and dashed curves represent different expansion models. For the shock wave model, $kt = (k/p)^{1/5}$ and R_0 found to be 6.92×10^{-4} mm/ns ^{0.4} and 0.0054 mm respectively for 1 Torr, $kt = 6.75 \times 10^{-7}$ mm/ns ^{0.4} and 2.0 mm respectively for 10 Torr. Fitting parameters for the drag model at 760 Torr are $\beta = 0.0125$ ns ⁻¹ and $R_0 = 1.4$ mm, respectively.	83

4.10	Position-time plots for Al^{2+} estimated from the ICCD images of SLA ions, for the ambient pressure range of 10^{-5} Torr to 760 Torr. Symbols denote measured data points, and the dashed curves represent shock wave expansion model. The inset shows the shockwave and drag model fits for the 760 Torr background pressure. For the shock wave model, $kt = (k/p)^{1/5}$ and R_0 found to be 1.832 mm/ns ^{0.4} and 4.63 mm respectively for 10^{-2} Torr, $kt = 0.0144$ mm/ns ^{0.4} and 0.79 mm respectively for 1 Torr, $kt = 4.66 \times 10^{-5}$ mm/ns ^{0.4} and 0.58 mm respectively for 10 Torr, and $kt = 2.233 \times 10^{-7}$ mm/ns ^{0.4} and 0.12 mm respectively for 760 Torr.	84
5.1	Beam diameter and fluence on the target as a function of lens position (z). When $z = 0$ the target is exactly at the beam focus, where the beam diameter is 112 microns and the laser fluence is 60.9 J/cm ²	90
5.2	Optical emission spectra of the plasma plumes measured at a distance of 2 mm from the target surface, for different laser beam sizes. The spectra are recorded with 100 ns integration time. Inset shows emission intensities measured for Al I (396.15nm), Al II (358.65 nm) and Al III (414.99 nm) respectively.	92
5.3	Time integrated ICCD images of the full plume and Al^{2+} plume recorded for various beam sizes. Images are acquired for an integration time of 500 ns. Each picture is the average of 10 images taken for successive laser shots.	93
5.4	Time-resolved ICCD images of plume expansion during the period 50 ns to 550 ns after laser irradiation, for different beam sizes on the target.	94
5.5	R-t plots drawn using the ICCD images. Solid lines and curves are numerical fits to the plume expansion data using the free expansion and shock wave models respectively.	95

5.6	Ion TOF spectra of the plasma for different laser beam sizes, acquired using the Faraday cup. The fast peak is very prominent when the target is at the beam focus. The slow peak becomes prominent away from the focus.	97
5.7	Ion flux of fast and slow ions measured for different laser beam sizes using the Faraday cup.	98
5.8	Ion velocities of fast and slow ions measured for different laser beam sizes using the Faraday cup.	99
6.1	Optical emission spectra of the plasma generated by ultrashort (ULA, 100 fs) and short (SLA, 7 ns) laser pulses, measured for $z = 1$ mm, for different ambient pressures (P).	105
6.2	(a) Electron temperature and (b) Stark broadening ($\delta\lambda$) plotted against ambient pressure, measured at a distance of 1 mm from the target surface, for a laser fluence of 44 J/cm^2	106
6.3	Temporal evolution of the ULA plasma plumes from the tungsten target, for ambient pressures ranging from 10^{-5} Torr to 760 Torr, at a laser fluence of 44 J/cm^2 . Each image is normalized to its maximum intensity for better view.	108
6.4	Temporal evolution of the SLA plasma plumes from the tungsten target, for ambient pressures ranging from 10^{-5} Torr to 760 Torr, at a laser fluence of 44 J/cm^2 . Each image is normalized to its maximum intensity for better view.	109
6.5	Variation of emission intensity with ambient pressure for ULA and SLA plasmas. Maximum intensity is observed in the pressure range of 1 Torr to 10 Torr. ICCD gate width is 1000 ns.	110
6.6	R-t plots for ULA estimated from gated ICCD images, for the ambient pressure range of 10^{-5} Torr to 760 Torr. Symbols are the measured data points while lines and curves are numerical fits to the data for different plume expansion models.	111

6.7	R-t plots for SLA estimated from gated ICCD images, for the ambient pressure range of 10^{-5} Torr to 760 Torr. Symbols are the measured data points while lines and curves are numerical fits to the data for different plume expansion models.	112
6.8	Ion TOF spectra of tungsten plasma, acquired at an angle of 20° with respect to the target normal, for ULA and SLA.	113
6.9	SEM micrographs of laser irradiated tungsten targets. First row shows the ULA surface, and a surface crack developed at the edge of the beam. Second row shows the SLA surface, revealing melting and recrystallization.	114
7.1	Schematic of the experimental setup for bremsstrahlung X-ray generation. A thin ($250 \mu\text{m}$) jet of metal nanoparticles suspended in water is irradiated by 800 nm, 150 fs laser pulses. Pulse energy is 5.5 mJ and pulse repetition rate is 10 Hz. M-mirror, WP - half-wave plate, PBS - polarizing beam splitter, L - lens, B - beaker, N - thin metal nozzle, P - water pump, D - CdTe X-ray detector, FG - function generator, MCA - multi-channel analyzer.	120
7.2	Standard radiation spectrum of Am_{241}	122
7.3	X-ray emission spectra obtained from Am_{241} with the amplifier gain set to 10x.	123
7.4	Angular distribution of X-ray emission from Aluminium (Al) target irradiated by ultrashort and short laser pulses of intensity $\approx 10^{15} \text{ W/cm}^2$ and 10^9 W/cm^2 respectively. The 0-180 axis indicates the laser propagation direction.	124
7.5	Bremsstrahlung emission from an unpolished Aluminium (Al) target kept in air irradiated with ultrashort and short laser pulses respectively. .	124
7.6	Angular distribution of X-ray emission from Tungsten (W) target irradiated by ultrashort and short laser pulses of intensity $\approx 10^{15} \text{ W/cm}^2$ and 10^9 W/cm^2 respectively. The 0-180 axis indicates the laser propagation direction.	125

7.7	Bremsstrahlung emission from an unpolished Tungsten (W) target kept in air irradiated with ultrashort and short laser pulses respectively. . . .	126
7.8	X-ray emission from a planar water jet irradiated by ultrashort laser pulses at an intensity of 10^{15} W/cm ² . (a) angular distribution of emission, (b) emission spectrum obtained for the detection angle of 30°. . . .	126
7.9	(a) Absorption spectra of Ag and Au nanoparticle suspensions showing LSPR bands; (b) SEM images of as prepared Ag and Au nanoparticles; (c) and (d) size distribution histograms for Ag and Au nanoparticles calculated from SEM images.	128
7.10	(a) Linear absorption spectra of Ag nanoparticle suspension measured after successive steps of laser irradiation (each step is 9000 laser shots), (b) absorption spectra drawn with the peak absorbances normalized to unity, (c) SEM images showing morphology changes.	129
7.11	(a) Absorption spectra of Au nanoparticle suspension measured after successive steps of laser irradiation (each step is 9000 laser shots), (b) absorption spectra drawn with the absorbances normalized to unity, (c) corresponding SEM images showing morphology changes.	130
7.12	Energy spectrum of bremsstrahlung X-ray emission measured in Ag and Au nanoparticle suspensions and their precursor solutions for a laser pulse intensity of 7.4×10^{14} W/cm ² . Total counts measured for the first 9000 laser pulses (step 1) are shown. Solid curves are numerical fits obtained using Eqn. 7.2.	131
7.13	Hot electron temperature versus $I\lambda^2$ for the generated plasmas. Solid curves are numerical fits to the data using Equation 7.3	133

List of Tables

6.1 Spectroscopic data of tungsten neutral lines (W I) used for the estimation of electron temperature.	106
---	-----

NOMENCLATURE

α	Absorption coefficient
β	Slowing coefficient
χ_0	Thermal conductivity at conventional equilibrium
χ_e	Coefficient of thermal conductivity of electrons
χ_i	Coefficient of thermal conductivity of lattice
$\Delta\lambda_{1/2}$	Full width at half maximum (FWHM) of emission
Δn_e	Electron density gradient
ϵ	Plasma dielectric function
ϵ_0	Emissivity of free space
ϵ_b	Binding energy of the ions to the lattice
ϵ_{esc}	Work function
ϵ_{kin}	Kinetic energy of free electrons
ϵ_{total}	Total energy of the laser
γ	Keldish parameter
\hbar	Planks constant
λ	Wavelength of laser
$\lambda_{i,j}$	Wavelength
Ω	Latent heat of vaporization
ω	Electron impact parameter
ω_0	Laser carrier frequency

ρ	Density of the material
ρ_0	Ambient gas density
σ_{ec}	Elastic scattering cross section of the electron
τ	Characteristic exchange time of the electron subsystem
τ_e	Ion electron transfer time
τ_i	Lattice heat conduction time
τ_L	Pulse Duration of the Laser
τ_p	Laser pulse duration
φ	Work function
ζ	Collisionality parameter
A	Absorptivity of the material
$A_{i,j}$	Transition probability
c	Velocity of light
C_e	Specific heat capacity of the electron
C_i	Specific heat capacity of the lattice
c_p	Specific heat
D	Heat diffusion coefficient
d	Gas molecule diameter
e	Electron Charge
E_0	Amount of energy released
E_a	Time dependent amplitude of the linearly polarized laser light

$E_{i,j}$	Energy of the excited state
F	Fluence
F_{th}	Threshold fluence
$g_{i,j}$	Statistical weight
I	Intensity of laser
I_p	Ionization potential
$I_{i,j}$	Line intensity
k	Laser wave vector
k_c	Thermal conductivity
K_{ibeff}	Effective inverse bremsstrahlung coefficient
K_{ib}	Inverse bremsstrahlung coefficient
L	Cavity length
L_n	Plasma density scale length
$ln\Lambda$	Coulomb logarithm for electron-ion collisions
L_p	Distance of Faraday Cup from the target
m	Electron rest mass
M_B	Mass of the background gas
m_e	Electron mass
N	Number of ions observed during time t
n	Number of photon
N_A	Avogadro's number

n_B	Density of the background gas
n_c	Critical density of plasma
N_e	Number density of plasma
n_e	Number density of free electrons on the metal
n_{cr}	Number density at the critical density layer
p	Ambient gas pressure
Q	Laser energy absorbed by the electrons
q_e	electron charge
R	Universal gas constant
R_0	Stopping distance of the plume
R_f	Reflectivity coefficient of the material
s	Number of excess photons absorbed
T	Gas temperature
T_e	Electron temperature
T_i	Lattice temperature
T_{hot}	Hot electron temperature
v_q	Electron quiver velocity
Z	Atomic number of element

CHAPTER 1

LASER-PRODUCED PLASMAS: AN INTRODUCTION

This chapter gives a brief introduction to laser-produced plasmas. The physics of laser-matter and laser-plasma interactions, and the processes which follow the evolution and expansion of laser-produced plasmas, are outlined.

*Our responsibility is to do what we can,
Learn what we can,
Improve the solutions and pass them on
————— Richard P Feynman*

1.1 Laser-Produced Plasma

The invention of high power lasers was a milestone in the field of light-matter interactions. The ruby laser, discovered by Maiman (1960), is considered to be the first successful operational laser. After this invention, the phenomenon of gas breakdown and dense plasma formation upon the focusing of intense laser pulses to suitable targets was demonstrated. Investigations in the field of optical breakdown and plasma formation in solids, liquids, and gases have rapidly advanced since then. Developments in ultrashort, intense lasers using the chirped pulse amplification (CPA) technique have helped the study of matter under extreme physical conditions (Strickland and Mourou 1985). The invention of the CPA scheme led to a method of amplifying the short but weak pulses obtained by active and passive mode locking by a few orders of magnitude (Mourou and Umstadter 1992). During this period, the application of a focused laser beam as a tool for material removal also was recognized and explored. The general term used to represent the phenomenon of material removal using a focused laser beam is laser ablation (LA) (Breech and Cross 1962; Russo 1995). Here an intense laser pulse delivers energy to the target surface for a very short interval of time, which instantly excites, ionizes and vaporizes the material into an extremely hot vapour plume, also known as the ‘plasma plume’ (Dawson 1964). The interaction of the laser pulse with the target depends very much on the wavelength of irradiation, the pulse duration and energy, and the physical properties of the material (Fabbro et al. 1982; Bloembergen 1974; Pert 1974).

The processes governing laser ablation, particularly ultrashort laser ablation (ULA), are not fully understood now. The fundamental processes occurring during the irradiation

tion of solid targets with ultrashort (femtosecond) and short (nanosecond) laser pulses are of somewhat different in nature from each other. Several studies have been undertaken to understand the mechanisms of laser absorption and material excitation, as well as material removal and plume expansion, but none of them can be considered complete. Moreover, comparative studies of laser-produced plasmas by ultrashort and short laser pulses are limited in number in literature (Margetic et al. 2000; Giacomo et al. 2005; Elhassan et al. 2008; Zhang et al. 2002; Albert et al. 2003; Oraevsky et al. 1996; Zeng et al. 2005; Freeman, et al. 2013;).

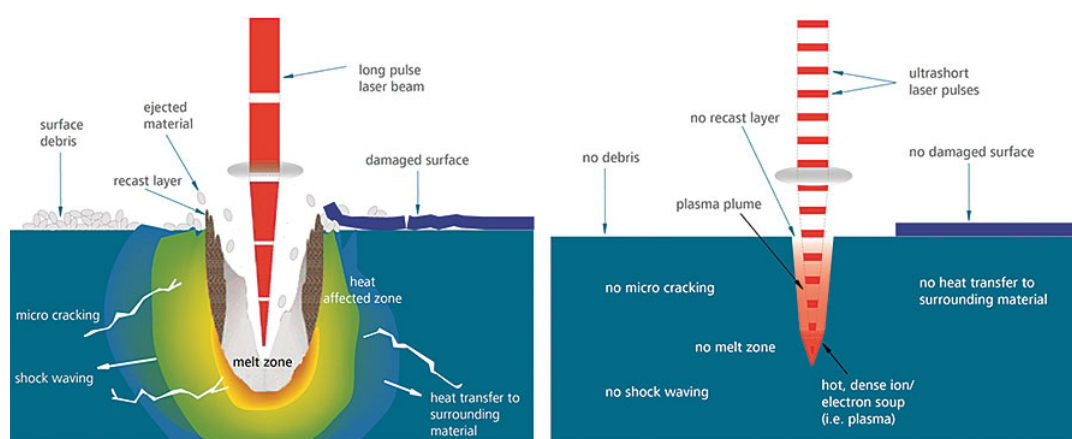


Figure 1.1: A schematic illustration of Ultrashort laser ablation (ULA) and Short laser ablation (SLA) [source: <https://www.assemblymag.com/articles/93059>].

Depending upon the duration of the laser pulse and its intensity, the ablation mechanisms can be described as either thermal or non-thermal (Leitz et al. 2011; Bulgakova and Bulgakov 2001). However, such a partition is not ideal since the simultaneous occurrence of both mechanisms cannot be ruled out (Choi and Grigoropoulos 2002; Welch et al. 1991). Many researchers have investigated the processes taking place at the target due to laser-matter interaction, both theoretically and experimentally. Non-thermal effects play an important role in ULA because the electron energy exceeds the Fermi energy of the metal (Welch et al. 1991). In such a case, the energetic electrons escape from the target and pull out the ions by the electrostatic force of charge separation. This non-equilibrium ablation occurs only when the maximum electron temperature is below the electrostatic ablation threshold. In the case of the ultrashort laser pulse, the duration of the pulse is short compared to the time required for energy to be transferred

from the electrons to the surrounding lattice, which results in a minimum heat affected zone (HAZ)(Russo et al. 2013). On the other hand, in the case of a long pulse, thermal conductivity of the target dominates the ablation process. This leads to the thermal equilibrium condition, which in turn results in thermal ablation. Thermal effects play a significant role in pulsed laser ablation, and these have been extensively studied by both the Kelly and Miotello (1997) and Miotello and Kelly (1995). Vaporization from the extreme outer surface and boiling from an extended near surface region take place at low and higher laser intensities respectively (Bulgakova and Bulgakov, 2001).

Short pulse laser ablation is well developed and has various applications such as LIBS, LA-ICP-MS, X-ray generation, Pulsed laser ablation, Micromachining, surface modification and cleaning, inertial fusion energy, etc. (Harmon and Russo 2013; Singh and Thakur 2007; Russo 1995). Current interest in ULA is mostly directed towards renewed and improved applications of short pulse laser ablation (SLA), including a number of diverse fields such as high-energy particle accelerators.

Laser produced plasmas are bright sources of electromagnetic radiation in the EUV, X-ray and γ -ray spectral regions (Ishikawa et al. 2012; Rundquist et al. 1998). Laser produced plasmas with electron densities as high as 10^{18} electrons/cm³ and temperatures as high as 10^4 K can be achieved to make laser-plasmas ideal media for efficient X-ray emission (Giulietti and Gizzi 1998). Hot electron generation is the pathway towards X-ray emission from the plasma, which can be efficiently achieved by using high Z materials (Nishimura et al. 1993).

In recent years, the development of shorter wavelength light sources has been motivated by their applications in technology and science in the extreme ultraviolet (EUV) and soft X-ray spectral regions. Synchrotrons, free electron lasers (FEL) and inertial confinement fusion (ICF) reactors are currently the practical sources for intense soft X-rays. These are huge experimental set-ups requiring large amounts of money and space. Therefore, in search of economic alternatives, vigorous research efforts are now ongoing for the optimization of X-ray emission from laser produced plasmas, using emission sources like solid targets, nanoparticles, microdroplets, and gaseous media.

1.1.1 Optical field ionization mechanism

The process by which the outermost electrons get away from the binding energy of nuclei and leave the net positively charged parent atom is known as ionization. In the linear optical regime, ionization happens only when the energy of the incident photon matches with the binding energy of the electron. Hence, electromagnetic radiation with higher photon energy ionizes matter with greater probability. When the laser irradiance is high enough (above the ablation threshold) to initiate plasma on the sample surface, some of the pulse energy will be used for heating, melting and vaporizing material into a plume which expands normal to the target surface. The photon energies of most high power lasers operating in the visible spectral region are typically too low to ionize matter directly. It should be noted that the energy of the individual photon determines the ionization of single atoms, while the intensity of the incident radiation determines the number of atoms ionized. While a fully ionized plasma state is difficult to maintain in the laboratory, partially ionized plasmas can be quite complex due to the presence of additional processes such as elastic and inelastic collisions, and excitation and de-excitation of atoms and molecules. At high laser intensities ($>10^{13}$ W/cm²) the behaviour of an atom is usually dependent on the ‘Keldysh parameter’ (Keldysh 1965) which is given as,

$$\gamma = \frac{\omega_0 \sqrt{2mI_0}}{eE_a} \quad (1.1)$$

where ω_0 is the laser carrier frequency, m the electron rest mass, I_0 the ionization potential of the atom (i.e. the binding energy of the most weakly bound electron), e the electron charge and E_a the time-dependent amplitude of the linearly polarized laser field. There are three types of optical field ionization (OFI) according to the Keldysh parameter (Keldysh 1965; Brabec and Krausz 2000; Protopapas et al. 1997). Multiphoton ionization (MPI), also known as above-threshold ionization (ATI) occurs for $\gamma > 1$. Tunneling ionization (TI), and over-the-barrier ionization (OBI) at extreme high intensities occur for $\gamma < 1$ (Keldysh 1965; Corkum 1993).

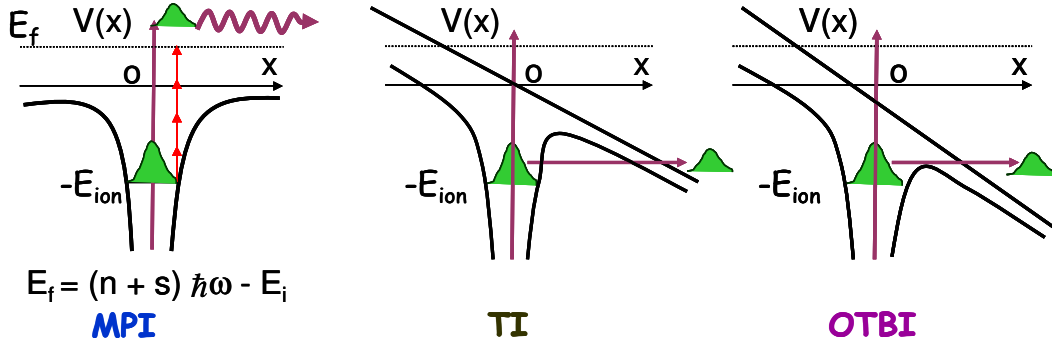


Figure 1.2: Schematic representation of the ionization regimes. (a) Multiphoton ionization or above-threshold ionization, (b) Tunnelling ionization, (c) Over-the-barrier ionization [source: Suman 2007].

Similar to the linear photoelectric effect, the nonlinear photoelectric effect - MPI takes place when a single photon by itself does not have sufficient energy to cause ionization ($I_p \geq \hbar\omega$), but the light pulse is intense enough to combine the effect of multiple (n) photons to take the electron above the ionization threshold ($n\hbar\omega \geq I_p$). In MPI of atoms in the laser field, the kinetic energy of the released electron is given by (Gontier et al. 1980),

$$E_f = (n + s)\hbar\omega - I_p \quad (1.2)$$

where n is the number of photons required for MPI and s is the number of excess photons absorbed. This excess absorption of photons through inverse bremsstrahlung (IB) is the absorption of photons from the laser field by the accelerating electrons during their scattering with neutral atoms or ions. Typically, MPI occurs in the intensity range $10^{13} - 10^{14} \text{ Wcm}^{-2}$. For wide band gap dielectrics and semiconductors, where the photon energy is less than band gap, free carriers are generated due to multiphoton ionization.

At higher intensities, the excitation laser field corresponding to a regime of $\gamma < 1$, ($> 10^{14} \text{ Wcm}^{-2}$) the distortion of the Coulomb potential can be so large that the barrier between a bound state and continuum does not remain infinite. There comes a situation when the initially bound electron can tunnel through the distorted Coulomb barrier. An

electron can successfully tunnel through if the tunnelling frequency is higher than the laser frequency. Since the laser intensity essentially controls the width of the barrier and the frequency of the laser field determines the time available for tunnelling, they both become important parameters controlling the rate of tunnel ionization (TI, Gontier et al. 1980).

At extremely high intensities, when the Coulomb barrier falls below the bound electron's energy, the electron is exposed to the continuum directly. This ionization mechanism is called over the barrier ionization (OBI, Keldysh, 1965).

The electron, once freed from the Coulomb potential by any one of the above three ionization mechanisms, is released to the strong electromagnetic field which excited the matter. Initially, the released electron sees the E and B fields of the laser pulse, and is subjected to the Lorentz force, resulting in an oscillatory motion in the laser electric field. The energy possessed by the free electron in the laser field is known as the electron quiver energy, which is given by (Popruzhenko 2014),

$$E_{osc} = \frac{e^2 E^2}{4m\omega^2} \quad (1.3)$$

where E and ω are the electric field and angular frequency of the laser field respectively. Therefore, an ultra-short laser pulse rapidly ionizes any medium via any of the three optical ionization mechanisms resulting in the formation of dense plasma.

1.1.2 Timescales in plasma formation

In short, when an intense laser is focussed to a small spot, dense matter is heavily ionized due to different ionization processes depending on the intensity as discussed above, and results in a hot soup of electrons and ions with a dominant collective behaviour, which is the plasma.

The formation of plasma on a solid surface is a dynamic process. During the interaction of a laser beam with solid targets, the laser energy is partially absorbed by free

electrons via inverse bremsstrahlung. Free electron excitation happens when the total energy of the laser exceeds the binding energy ($\varepsilon_{tot} > \varepsilon_b$) and the work function of the target (φ). The extra energy ($\varepsilon_{kin} = \varepsilon_{tot} - \varepsilon_b - \varphi > 0$) constitutes the kinetic energy of the free electrons. The electrons freed from the atoms are accelerated directly by the laser field, and these electrons pull the ions by their Coulomb field. These oscillating electrons collide with the neutral atoms and ions in their vicinity and cause further ionization. The electrons are subject to an extraordinary heating rate while the lattice remains comparably cold in the early stages. This is known as ‘nonthermal’ ablation. Some part of the absorbed energy from the laser pulse is transported to the ablation surface via the diffusive process of thermal conduction, which results in ‘thermal’ ablation. In short pulse laser ablation (SLA), typically a dense cloud of electrons is formed at the rising edge of the laser pulse itself, even before the intensity peak of the pulse is reached. This dense electron cloud and the resultant positively charged background ions will interact with the trailing part of the laser pulse. The contribution of laser-plasma interaction dominates in SLA, which is absent in ULA. Thus ultrashort pulse laser ablation (ULA) and short pulse laser ablation (SLA) have fundamentally different characteristics shown in the figure below, which will be reflected in the properties of the generated plasmas. Hence, measuring the properties of such plasmas is essential for understanding the physics of the interaction.

ULA becomes attractive for different applications since the pulse duration of the laser (τ_L) is shorter than the electron to ion energy transfer time (τ_e) and electron to lattice heat conduction time (τ_i). Lasers having pulse duration (τ_L) less than 1 ps come under this class. Theoretical concepts on ULA have been proposed by Anisimov et al. (1974), Gamaly et al. (2002), Nolte et al. (1997), and Perez and Lewis (2009), etc. Because of the fast early stage evolution of ULA, a well-defined theoretical model is required to explain the major mechanism of laser-matter interaction in ultrashort time scales.

During the interaction of an ultrashort laser pulse with a metal surface, the absorbed pulse energy will excite valence electrons through the inverse bremsstrahlung mech-

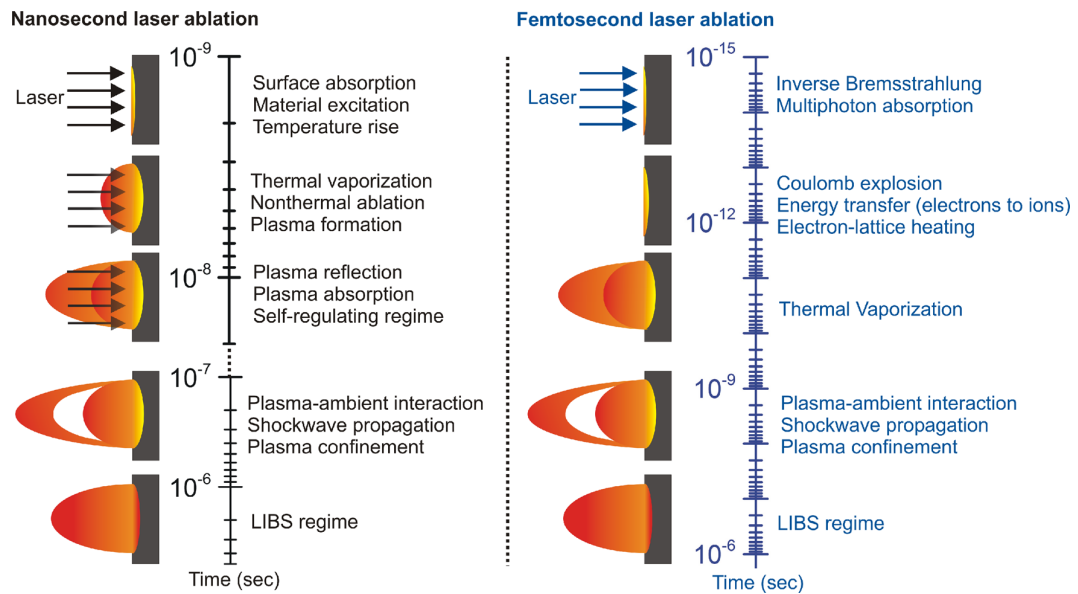


Figure 1.3: Schematic representation of Ultrashort and Short laser produced plasma formation [source: Harilal et al. 2018].

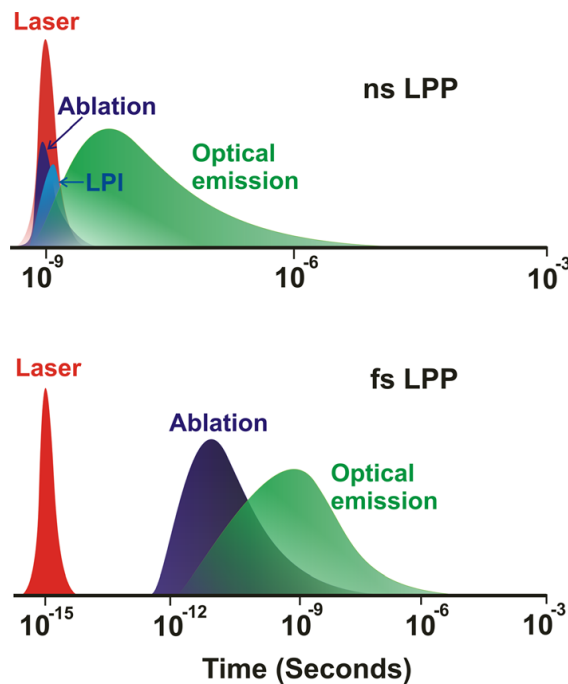


Figure 1.4: Pictorial representation of LPP using short (nanosecond) and ultrashort (femtosecond) laser pulses [source: Verhoff et al. 2012].

anism. The excited electrons are thermalized immediately due to the short electron-electron interaction time. Since this instantaneous change in temperature does not affect the ions, the lattice remains at room temperature. This difference in temperature

results in a temperature gradient between electrons and lattice, for several picoseconds. At this stage, electronic and lattice sub-systems are out of equilibrium. This transient two-temperature system will tend to reach thermal equilibrium within a few tens of ps through electron-phonon interactions, as well as through electron diffusion out of the excited region. This dynamic process is well described by Anisimov et al. (1974) through a two-temperature model (Anisimov and Luk'yanchuk 2002; Anisimov and Kapeliovich 1974; Nolte et al. 1997). This model is a widely used tool for the investigation of electron and lattice temperatures in ULA. The two-temperature model (TTM) is given by coupled nonlinear equations describing energy transport from electrons to the cold lattice:

$$C_e \frac{\partial T_e}{\partial t} = \chi_e \frac{\partial^2 T_e}{\partial z^2} - \mu(T_e - T_i) + Q \quad (1.4)$$

$$C_i \frac{\partial T_i}{\partial t} = \chi_i \frac{\partial^2 T_i}{\partial z^2} - \mu(T_e - T_i) \quad (1.5)$$

where z is the distance perpendicular to the target surface, C_e , C_i are the specific heat capacities of the electrons and lattice [$\text{J cm}^{-1}\text{K}^{-1}$], and χ_e , χ_i are the coefficients of thermal conductivity of electrons and lattice respectively $\mu = \frac{C_e}{\tau}$ is the electron-phonon coupling constant and τ is the characteristic exchange time of the electron subsystem. Q is the laser energy absorbed by the electrons, given by the equation,

$$Q = \frac{-\partial I}{\partial z} = \alpha I \quad I(0, t) = I_s \quad (1.6)$$

where α is the absorption coefficient. $I_s = I(t) \times A$, where $I(t)$ is the absorbed laser intensity at the metal surface ($z = 0$). $A = (1 - R)$ is absorptivity of the material and R is the reflectivity coefficient of the material.

As mentioned earlier, three different time scales, viz, τ_e , τ_i , τ_L are involved in the early stage evolution of ULA. Here, $\tau_e = \frac{C_e}{\mu}$ is the electron cooling time, $\tau_i = \frac{C_i}{\mu}$ is the lattice heating time, and τ_L is the laser pulse duration. Since the specific heat capacity

of electrons is less compared to that of the lattice, electrons achieve a high transient temperature. At this stage the thermal conductivity of the lattice can be neglected. When the pulse duration of the laser changes, the interaction of laser pulses with the target also changes significantly. The interaction can be divided into three different temporal regimes, namely, femtosecond, picosecond, and nanosecond interactions.

Interaction in femtosecond time scales can be considered when the laser pulse is too short compared to the characteristic electron energy relaxation time $\tau_L \ll \tau_e$, which is typically in the order of 1ps for metals (Chichkov et al. 1996; Eesley 1983, 1986). When the electron temperature remains smaller than the Fermi energy, the specific heat capacity and thermal conductivity of the electron can be written as $C_e = C'_e T_e$ and $\chi_e = \chi_0(T_e) \frac{T_e}{T_i}$ respectively, where $\chi_0(T_e)$ is thermal conductivity at conventional equilibrium. Due to this shorter timescale, the electron-phonon coupling term and the electron thermal conductivity term can be neglected from the coupled nonlinear equation model, giving

$$C'_e \frac{\partial T_e^2}{\partial t} = Q \quad (1.7)$$

where $Q = 2I_0 A \alpha \exp(-\alpha z)$, with I_0 being the incident laser intensity. Solving the above equation gives

$$T_e(t) \approx \left\{ T_0^2 + \frac{2I_0 A \alpha}{C'_e} \right\}^{\frac{1}{2}} \exp(-\alpha z) \quad (1.8)$$

where T_0 is the initial temperature. At the end of the laser pulse the electron temperature is given by (Chichkov et al. 1996),

$$T_e(\tau_L) \approx \left\{ \frac{2F\alpha}{C'_e} \right\}^{\frac{1}{2}} \exp\left(\frac{-z}{\delta}\right) \quad (1.9)$$

Here $T_e(\tau_L) \gg T$ is assumed and the absorption of laser (of fluence $F = I_0 \tau_L$) will take place only up to a skin depth $= \frac{2}{\alpha}$. The high intensity involved in ULA results in the rapid and direct creation of vapour and plasma from the solid target. The lattice gets

heated up relatively slower in picosecond timescales, and thermal ablation effects are not significant.

In the case of picosecond laser interaction with matter, the characteristic timescales relate as $\tau_e \ll \tau_L \ll \tau_i$, such that the characteristic electron energy relaxation time is much smaller compared to the pulse duration of the laser. The time scale of lattice heating is therefore smaller than the pulse duration of the laser. Hence, the contribution of electron temperature can be neglected. The temperature of the lattice is given by (Chichkov et al. 1996).

$$T_i \approx T_e \left(1 - \exp\left(\frac{-t}{\tau_i}\right) \right) \approx \left(\frac{t}{\tau_e} \right) T_e \quad (1.10)$$

which is much lower than the electron temperature in the picosecond regime. As we know, electron energy relaxation (electron cooling) happens due to energy exchange with the lattice. Hence, electron temperature and lattice temperature at the end of the laser pulse are given by,

$$T_e \approx \frac{I_0 A \alpha}{\mu} \exp(-\alpha z) \quad (1.11)$$

$$T_i \approx \frac{F \alpha}{C_i} \exp(-\alpha z) \quad (1.12)$$

Obviously, lattice temperature at the end of the laser pulse is determined by the electron cooling time. Hence, picosecond laser ablation involves electron heat conduction and the formation of the heat-affected zone (HAZ).

Finally, in the case of nanosecond laser pulses, $\tau_e \ll \tau_i \ll \tau_L$ is considered. The electrons and the lattice achieve thermal equilibrium i.e. $T_e = T_i = T$. The coupled nonlinear equations reduce to

$$C_e \frac{\partial T}{\partial t} = \chi_e \frac{\partial^2 T}{\partial z^2} + Q \quad (1.13)$$

In this regime, the energy deposited on the target over nanosecond time scales is used to heat up the target surface to the melting point and then to the vaporization temperature. Each metal has a threshold energy for evaporation (energy required to exceed the specific heat of evaporation) given by (Momma et al. 1996),

$$I_{th} \approx \frac{\rho\Omega D^{\frac{1}{2}}}{\tau_L^{\frac{1}{2}}}, \quad F_{th} \approx \rho\Omega D^{\frac{1}{2}}\tau_L^{\frac{1}{2}} \quad (1.14)$$

The threshold fluence for evaporation with nanosecond laser pulses increase by a factor $\tau_L^{\frac{1}{2}}$. In this regime, ablation is more complicated since the time available for a thermal wave to propagate into the target is large, creating a large area of the melted material surface.

1.1.3 Atomic process in a plasma

According to conservation laws, every atomic process is as frequent as its inverse process in a thermodynamic system. In principle, knowing the rates of all the atomic processes would allow the prediction of the emission spectrum. The combined effects of many processes determine the emission spectrum of plasma. The processes of collisional and radiative excitation, de-excitation, ionization, and recombination involve many energy levels and several stages of ionization. Some of the main atomic processes occurring in the plasma are briefly explained below.

1.1.3.1 Absorption mechanisms

Free-Free Absorption: Inverse bremsstrahlung (free-free absorption), where a photon is absorbed by an electron in the presence of an ion, is particularly relevant to photon energies of a couple of eV or less. In detail, the electrons, while oscillating under the influence of the laser electric field, collide with the ions to absorb radiation and results an increase of the energy and temperature of the electron particle. The fraction of absorbed laser energy after propagation over a distance L in a uniform plasma is given

by (Kruer, 1988),

$$\alpha_{abs} = 1 - \exp(-k_{ib}L) \quad (1.15)$$

where

$$k_{ib} = 3.1 \times 10^{-7} Z n_e^2 \ln \Lambda \omega_L^{-2} \left[1 - \frac{\omega_p^2}{\omega_L^2} \right]^{-\frac{1}{2}} (T_e(\text{eV}))^{-\frac{3}{2}} \text{cm}^{-1} \quad (1.16)$$

k_{ib} is the inverse bremsstrahlung coefficient, i.e. the imaginary part of the laser wave vector k , and $\ln \Lambda$ is the Coulomb logarithm for the electron-ion collisions. It is clear from the above equation that collisional absorption is higher for lower temperatures, higher densities, and higher Z plasmas.

Consequently, in the case of interaction with inhomogeneous plasma, most of the absorption takes place near the critical density n_c , provided that the density scale length is not too short. On the other hand, for sufficiently large scale lengths, strong absorption may occur by dense plasma preventing laser energy from reaching the critical density layer, thus reducing inverse bremsstrahlung absorption (Kruer and Estabrook 1976).

At high laser intensities electron-ion collision frequency is dominated by the oscillatory behaviour of the electrons in the laser electric field. In fact, the effective electron velocity is given by (Ginzburg 1961),

$$v_{eff} = \sqrt{v_{ih}^2 + \frac{eE_L^2}{m\omega_L}} \quad (1.17)$$

where E_L is the laser electric field. Due to the strong dependence of the cross-section of electron-ion collisions on the electron velocity $\sigma_{ei} \approx 4\pi Z^2 e^4 m^2 v_{th}^{-4}$, the inverse bremsstrahlung coefficient reduces to a value given by,

$$k_{ib}^{eff} = k_{ib} \left[1 + \frac{3}{2} \left(\frac{v_q}{v_{th}} \right)^2 \right]^{-1} \quad (1.18)$$

where $v_q = \frac{eE_L}{m\omega_L}$ is the electron quiver velocity.

Bound-Free Absorption: Photo-ionization processes (bound-free absorption), are the physical processes in which an ion is formed from the interaction of a photon with plasma atom. It exhibits a series absorption coefficients corresponding to different ionization stages. Photo-ionization is particularly relevant in optically thick plasma because the mean free path of the photon will be smaller than the dimensions of the plasma.

Bound-Bound Absorption: Absorption occurs when an incident photon has the same energy as the difference between two bound electron states, resulting in an electron excited from a lower energy level to a higher level. This kind of collisionless absorption plays a significant role in laser absorption. This mechanism is known as *resonance absorption*, which occurs when the incident laser is p-polarized. In this mechanism, the laser energy is transferred to the excitation of electron plasma waves near the critical density layer where the local electron plasma frequency is equal to the laser frequency. The energy of the electron plasma waves is deposited in the plasma via electron acceleration and collisional absorption.

In more detail, laser radiation incident on plasma obliquely with a component of the electric field in the plane of incidence (p-polarized) can excite resonant longitudinal plasma oscillations at the critical density (n_c) surface. Using Snell's law it can be shown that the electromagnetic wave will propagate up to the density of $n_c \cos^2$ before it undergoes specular reflection. Some amount of light energy can tunnel into the critical density layer at this interface. The crucial feature is the presence of a component of the incident electric field \vec{E} along the density gradient $\vec{\nabla} n_e$, i.e. $\vec{E} \cdot \vec{\nabla} n_e$ in the case of p-polarized light. The associated electrostatic wave with this tunnelling field can give rise to the resonant electron wave when the natural plasma frequency matches with the external driving field frequency. This field can be expressed as,

$$\frac{E_d}{\epsilon(Z)} = \frac{E_L}{\sqrt{2\pi\omega_0 \frac{L_n}{C}}} \varphi(\tau) \quad (1.19)$$

where ϵ is the plasma dielectric function, and L_n is the plasma density scale length. τ

relates the scale length to the angle of incidence as

The function φ can be expressed as (Ginzburg 1961)

$$\varphi(\tau) \approx 2.3\tau \exp\left(-\frac{2\tau^3}{3}\right) \quad (1.21)$$

By introducing a small amount of damping $\frac{\nu}{\omega_0} \ll 1$, the fraction of energy transferred from the electromagnetic wave to the electron plasma wave can be derived as,

$$f_{RA} \approx \frac{\varphi^2(\tau)}{2} \quad (1.22)$$

as a result of which, part of the incident electromagnetic wave energy is transferred from the light wave to the plasma wave, with the above equation estimating the amount of absorption.

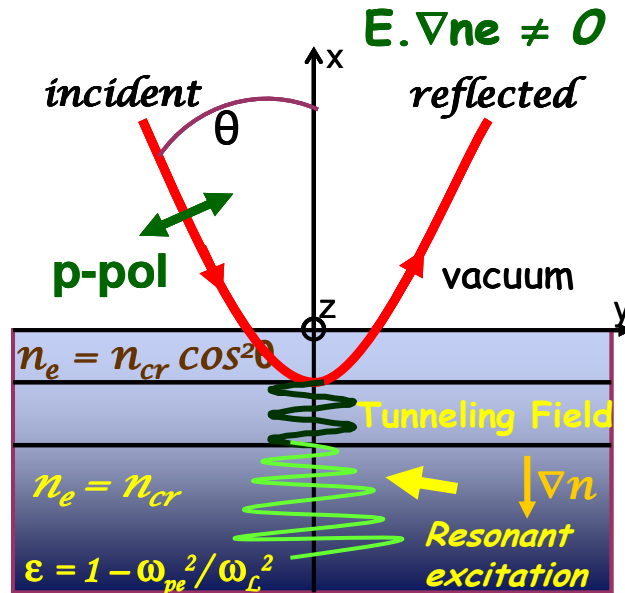


Figure 1.5: Schematic diagram of resonance absorption [source: Suman 2007].

1.1.3.2 Emission mechanisms

Free-Free Emission: In plasma, bremsstrahlung radiation generally occurs due to the deceleration of electrons by the field of ions. Radiation is emitted when a coulomb

field or another charged particle deflects a charged particle. Since the electron is free before and after the emission, the radiation is also referred to as free-free radiation. When these energetic electrons collide with surrounding ions they emit radiation due to Bremsstrahlung. Bremsstrahlung radiation can be measured experimentally, from which the temperature of the plasma can be deduced. Bremsstrahlung (free-free emission) produces a continuum of radiation where the logarithm of the X-ray energy spectrum is a straight line when the electron distribution is a Maxwellian.

Free-Bound Emission: Recombination radiation (free-bound) occurs when an electron recombines with an ion and emits a photon, contributing to the continuum emission spectrum. As the electron is free before recombination and bound afterwards, the radiation is also referred to as free-bound radiation. The energy of the emitted photon,

$$h\nu = \epsilon_0 + \chi_i \quad (1.23)$$

where $\epsilon_0 = \frac{1}{2}mv^2$, ϵ_0 is the energy of the free electron and χ_i is the ionization potential of the i^{th} level of ion. For low atomic number and high T_e , bremsstrahlung radiation is predominant over recombination radiation. For high atomic number and low T_e , recombination radiation predominates bremsstrahlung radiation.

Bound-Bound Emission: Spectral line emission (bound-bound) occurs when an electron decays from an excited state to a lower energy level, emitting a photon with energy equal to the difference between the levels. Emissions due to the transition of electrons between two bound states are referred to as line radiation. Those transitions to the ground state of the ion are the strongest, and they are referred to as resonance transitions.

In addition several other processes also occur in the plasma, such as collisional excitations, de-excitations, and ionization. Collisional excitation involves collisions between an electron and a neutral particle or an ion resulting in the conversion of kinetic energy into excitation energy in the atomic system. In the inverse process of collisional de-excitation, excitation energy is converted into kinetic energy by the collision. Colli-

sional ionization can occur when the kinetic energy of an electron is sufficient to remove another electron from an atom or molecule. Collisional recombination occurs when two electrons encounter an ion, and one electron recombines with an ion when the kinetic energy of the system is conserved.

1.1.4 Hot electrons and X-rays from laser produced plasma

When the gas temperature is very high most elements are highly ionized, and the gas becomes a hot plasma. Negatively charged electrons in this plasma experience a force when they pass close to an ion, and accelerating charges emit electromagnetic dipole radiation. Since the electron loses energy in the encounter it will slow down, which is named thermal bremsstrahlung. Moreover, as the electron slows down the plasma also loses energy, and the gas cools. The electron is not bound to any particular ion throughout the interaction. This type of radiation is also known as free-free radiation. Hot electrons may be generated as a consequence of the inhibition of electron thermal conduction (Thermal bremsstrahlung) that prevents the laser energy absorbed in the proximity of the critical density layer to propagate towards the high-density plasma regions. In these circumstances, a thin plasma layer just beyond the critical surface can reach very high temperature, and the production of hot electrons and ions becomes possible. Taking into account the inhibited electron thermal conduction, one gets, for the hot electron temperature (Forslund et al. 1977),

$$T_{hot} \propto (I\lambda^2)^{\frac{2}{3}} \quad (1.24)$$

Resonance absorption mechanism is another source of hot electrons. This absorption process produces an intense electric field parallel to the plasma density gradients, strongly localized in the proximity of the critical surface. Slow electrons that travel only a small portion of this high field region during a laser period experience an oscillating electric field, which does not produce a significant increase in their kinetic energy. However, fast electrons that move across the high field region in a small portion of the period experience a constant electric field. Due to the short time scales of the electric field, the energy gain of these electrons is small. However, electrons with an

intermediate velocity, crossing the region in a portion of the period $\Delta t \leq \frac{T}{2}$, can gain as much energy as their initial kinetic energy. In this case the hot electron temperature scales as (Forslund et al. 1977),

$$T_{hot} \propto (I\lambda^2)^{\frac{1}{3}} \quad (1.25)$$

These hot electrons are the signature of X-ray emissions, and are highly detrimental to the achievement of Inertial Confinement Fusion conditions. Measurements of the spectrum of X-ray radiation emitted in laser-plasma interaction experiments often show evidence of the generation of superthermal electrons. In fact, besides the thermal Maxwellian population of electrons characterized by a temperature T_e , there is a small population being distributed as a Maxwellian at a much higher temperature T_h . These electrons give rise, via. bremsstrahlung emission, to hard X-ray radiation, well above the typical thermal emission from LPP. Therefore, hot electrons emission can be useful in applications requiring hard X-rays.

1.2 The scope of the thesis

The interaction of short laser pulses with matter have opened the broad field of laser-produced plasmas in optics. The implementation of the Chirped Pulse Amplification (CPA) technique for lasers has provided new opportunities in the domain of ultra-intense and ultrashort laser produced plasmas (Strickland and Mourou 1985). The pulse duration of the ultrashort laser pulse is shorter than the electron-to-ion energy transfer time and heat conduction time in the sample lattice, making it distinct from other long pulse duration lasers (Gamaly et al. 2002). This results in different laser-matter interactions and heat dissipation mechanisms as compared to short pulse laser ablation (SLA). Through ultrashort laser produced plasmas, important applications like material processing, thin film growth using ultra fast pulsed-laser deposition, and ultrashort pulse X-ray sources, particle acceleration, and ion sources have been explored. Even though many studies have been carried out in spectroscopy and hydrodynamic expansion of laser produced plasma using different lasers, comparative studies of the effect of

different pulse durations on the generated plasmas is limited. Since the ablation process is significantly affected by the pulse duration of the laser, the study of the formation and the evolution of the plasma using different pulse durations is instrumental in understanding the fundamental physics. During the literature survey we observed that the comparison of ultrashort and short pulse laser produced plasmas is very limited, and that the fundamentals of ultrashort pulse laser ablation are still not fully understood. In addition, the studied material tungsten (W) is currently a leading choice for the diverter material in ITER, and plasma facing material in nuclear fusion reactors. The aforesaid discussion undoubtedly proves the potential candidature of ultrashort laser produced plasmas in state-of-the-art application domains.

Previous researchers have mostly focused on aluminium target for enhancing X-ray emission from laser produced plasmas (Giulietti and Gizzi 1998; Nagel et al. 1974). However, experimental conditions also can be optimized for enhancing the X-rays, which is an area that needs more attention. In addition, these experiments are expected to provide new insights into the science of short wavelength generation from laser produced plasmas. Laser-plasma X-ray sources are extensively used in a wide range of advanced scientific and technological applications including X-ray microscopy, nanolithography, dynamics studies of the mechanical properties of materials, and X-ray time-resolved radiography.

1.3 Objectives of the thesis

Properties of the plasma can be deduced from multitude of diagnostic measurements and spectroscopic investigations. Optical emission spectroscopy and ion parameters such as ion energy distributions, the total number of ions, their average and maximum charge states, the abundance of ion and neutral species and energy carried by them give information about the mechanisms of laser-plasma interaction, the absorbed energy, and the electron temperature of the plasma. After a detailed literature survey, the following objectives were finalized for the research work reported in this thesis:

- Spectroscopic investigation and characterization of laser produced plasma from

Aluminium target.

- Ion dynamics of laser produced aluminium plasma at different ambient pressures.
- Effect of laser spot size on the dynamics of ultrashort laser produced Aluminium plasma in vacuum.
- Multidiagnostic analysis of laser produced tungsten plasma at different ambient pressures.
- Optimization of X-ray emission from laser produced plasma.

1.4 Outline of the thesis

The present thesis comprises of eight chapters, and each chapter is summarized concisely below.

Chapter 1: This Chapter gives an introduction to laser produced plasmas and their applications. The underlying phenomenon of ultrashort and short pulse laser ablation (ULA and SLA) are discussed. Timescales of different plasma formations are explained.

Chapter 2: Chapter 2 provides a detailed description of the lasers and spectrometers used in the experimental setup. It also includes a detailed explanation of different experimental techniques.

Chapter 3: This chapter gives a comparative study of ultrashort and short pulse produced plasmas generated from a solid aluminium target in a nitrogen ambient. Optical emission spectroscopy, Optical time of flight studies and ICCD imaging are carried out as a function of ambient pressure. The evolution and expansion dynamics of neutral and ionic species in the plasma are presented for a background pressure range of 10^{-2} to 760 Torr of nitrogen.

Chapter 4: This chapter discusses ion dynamics measured at different ambient pressures. We have measured the spatial and temporal evolution of the whole plasma plume, as well as that of the ionic (Al^{2+}) component present in the plume, using spectrally resolved time-gated imaging. Comparative studies of ion dynamics from ultrashort and

short pulse laser produced plasmas is included.

Chapter 5: This chapter gives details of the expansion dynamics of a laser produced Aluminium plasma, measured as a function of the laser spot diameter on the target, investigated using optical emission spectroscopy, 2-D imaging, and Faraday cup probing.

Chapter 6: This chapter discusses the multi-diagnostic measurement of laser produced tungsten plasma, facilitating a complete study of plume formation and expansion at different ambient pressures. The study is carried out for different laser pulse durations (ULA and SLA) and the results are compared. Ion TOF and structural analysis of irradiated tungsten surface are done for both cases.

Chapter 7: In this chapter, optimization of X-ray emission from laser produced plasma generated on different targets is discussed. A comparison of X-ray emission from ultrashort and short pulse laser ablation of aluminium and tungsten samples is carried out. We have also used liquid jets of *Ag* and *Au* nanoparticles (200 microns size) irradiated by high intensity ultrashort laser pulses to produce bremsstrahlung X-rays.

Chapter 8: This is the concluding chapter, in which a few proposals for future work are given.

CHAPTER 2

EXPERIMENTAL TECHNIQUES AND INSTRUMENTATION

This chapter discusses the experimental techniques used for the investigation of laser-produced plasmas (LPP) and the instruments used for characterizing LPPs. Instrumentation required to perform optical emission spectroscopy, optical time of flight measurements, ICCD imaging, ion emission studies and X-ray emission studies of the plasma plume generated by nanosecond/femtosecond laser pulses is explained in detail.

*“The formulation of a problem is often more essential than its solution,
Which may be merely a matter of mathematical or experimental skills.”*

————— *Albert Einstein*

2.1 Introduction

In this work, different diagnostic techniques have been used to characterize the plasma formed at the target surface. Plasmas are efficient broadband emitters, and this chapter outlines the experimental techniques employed in the characterization of laser-produced plasmas (LPPs) in both the visible and X-ray regimes. The experimental setup involves three main parts, which are (a) the laser source, (b) experimental environment and (c) detection systems. Another important part is the target. We have used aluminium (Al) as low Z element and tungsten (W) as high Z element to compare low Z and high Z elemental plasmas. In addition, X-ray emission studies have been performed using silver (Ag) and gold (Au) nanoparticles used in the form of a thin liquid jet.

In the following sections we describe five different experimental techniques which were used to characterize the LPP. These are optical emission spectroscopy, optical time of flight, time-resolved ICCD imaging, ion measurements using Faraday cup, and X-ray emission spectroscopy. These techniques were used to unveil the fundamental physics underlying ultrashort and short pulse laser produced plasmas.

2.2 Ultrashort pulse laser source

The ultrashort pulse laser system has three components: The Ti:Sapphire ultrafast oscillator, Ti:Sapphire regenerative chirped pulse amplifier (CPA), and the Nd:YAG pump laser for the CPA.

2.2.1 The ultrafast oscillator

The Ti:Sapphire ultrafast oscillator (*Tsunami*, Spectra-Physics) consists of a folded optical cavity is shown in Figure 2.1. An acoustic-optic modulator (AOM) with active feedback is used for the generation of ultrashort pulses by the regenerative mode-locking technique. Dispersion compensation of the laser cavity is achieved with a pair of prisms, and the wavelength can be tuned with an adjustable slit. The lasing material is a 1 cm long Ti: sapphire crystal rod which is pumped using a solid-state Nd:Vanadate (Nd:YVO4) continuous wave laser (*Millennia Pro-S*, Spectra-Physics). A cw diode laser (809 nm, 40 W) pumps the vanadate crystal via an optical fiber module. The fundamental emission from the vanadate crystal (1064 nm) is frequency-doubled using a Lithium Triborate (LBO) crystal to produce 532 nm at an output power of 5.2 W. The output beam has a TEM₀₀ spatial intensity distribution with a nominal beam width of 2.3 mm. The ultrafast oscillator produces Gaussian pulses of approximately 100 fs duration at a repetition rate of 82 MHz, and the output wavelength can be tuned from 700 nm to 1000 nm. Maximum average power output of 550 mW can be obtained at the peak of the tuning curve, which is 809 nm.

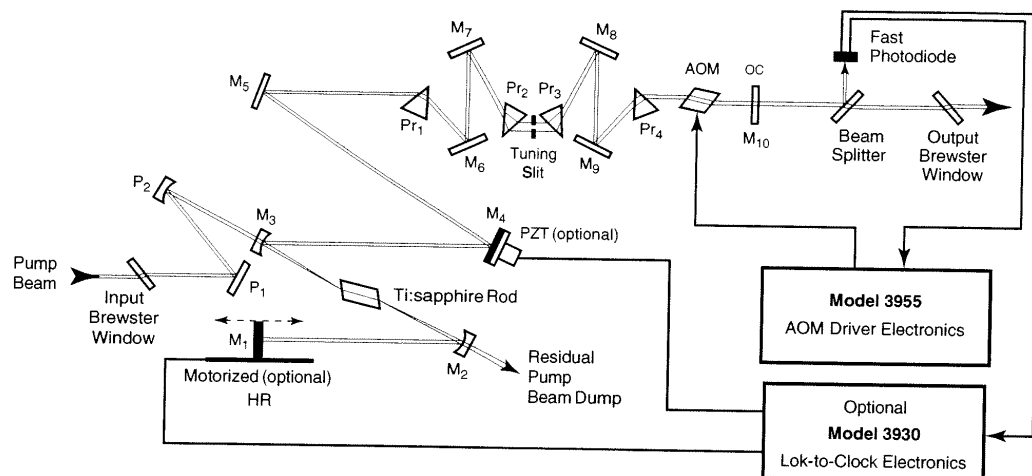


Figure 2.1: Schematic of cavity alignment of Tsunami oscillator with fs configuration.[source: [https://www3.nd.edu/~bohnggrp/site/groupfiles/Ti-Sapphire %20Alignment.pdf](https://www3.nd.edu/~bohnggrp/site/groupfiles/Ti-Sapphire%20Alignment.pdf)].

Synthetically grown Sapphire (Al_2O_3) is doped with titanium to give the Ti:Sapphire crystal, in which the titanium ion (Ti^{3+}) is responsible for laser action. The crystal

field of the sapphire lattice splits the electronic ground state of the Ti^{3+} ion into a pair of vibronically broadened levels. Absorption transitions occur over a broad range of wavelengths from 400 nm to 600 nm, and fluorescence transitions occur from the lower vibrational levels of the excited state to the upper vibrational levels of the ground state. Although the fluorescence band starts from 600 nm, the lasing action is only possible at wavelengths longer than 670 nm because the long wavelength side of the absorption band overlaps the short wavelength end of the fluorescence spectrum. Additionally, the tuning range is affected by mirror losses, tuning element losses, pump power and atmospheric absorption.

The pulse width tuning characteristics of Ti:Sapphire is influenced by factors inherent in the Ti:Sapphire material as well as the cavity parameters. The optical components in the laser cavity introduce positive group velocity dispersion (GVD) and cause pulse spreading in addition to that caused by self-phase modulation in the Ti:Sapphire rod, while negative GVD, which is intentionally introduced in the cavity using four prisms, compensates these effects. Mode-locking in the Tsunami oscillator is achieved by using an AOM module in a regenerative mode-locking configuration. Unlike conventional active mode-locking, the RF signal used to drive the AOM is derived directly from the cavity in the regenerative mode-locking configuration. An advantage of this configuration is that it removes one of the greatest drawbacks of active mode-locking, i.e., the requirement that the cavity length matches the external drive frequency. In regenerative mode-locking, depending on the cavity length, the drive signal to the modulator automatically changes.

Initially, when the laser is switched on, it operates in the continuous wave (CW) mode with oscillations from several longitudinal modes. While these are partially phase-locked, mode beating generates a laser output at a frequency of $c/2L$. A photodiode detects this mode beating and is then amplified. Since this signal is twice the required AOM modulation frequency (ω_{ML}), it is divided by two followed by a phase adjustment such that the modulator is always at the maximum transmission when the pulse is present. Finally, the signal is re-amplified and given to the AOM.

2.2.2 The ultrafast amplifier

Even though the usual pulse energy levels (generally in nanoJoules) from ultrafast oscillators are sufficient for many applications like multi-photon fluorescence microscopy, femtosecond writing, fluorescence lifetime measurements, etc., much higher pulse energies (in the order of milliJoules) are required for performing intense laser field experiments. Therefore, a regenerative pulse amplifier is added to the system to obtain high energy ultrafast pulses. It is not possible to amplify ultrashort pulses directly to high energy levels, as the high intensities will damage the amplifying medium. Therefore, a technique called chirped pulse amplification (CPA) is employed to overcome this difficulty. In the CPA technique the pulse to be amplified is stretched in time by a large factor (typically 10,000) to reduce the peak power, so that the resultant pulse can be amplified without causing damage to the optical components. After amplification the pulse is compressed back to the original (or even a shorter) pulse width.

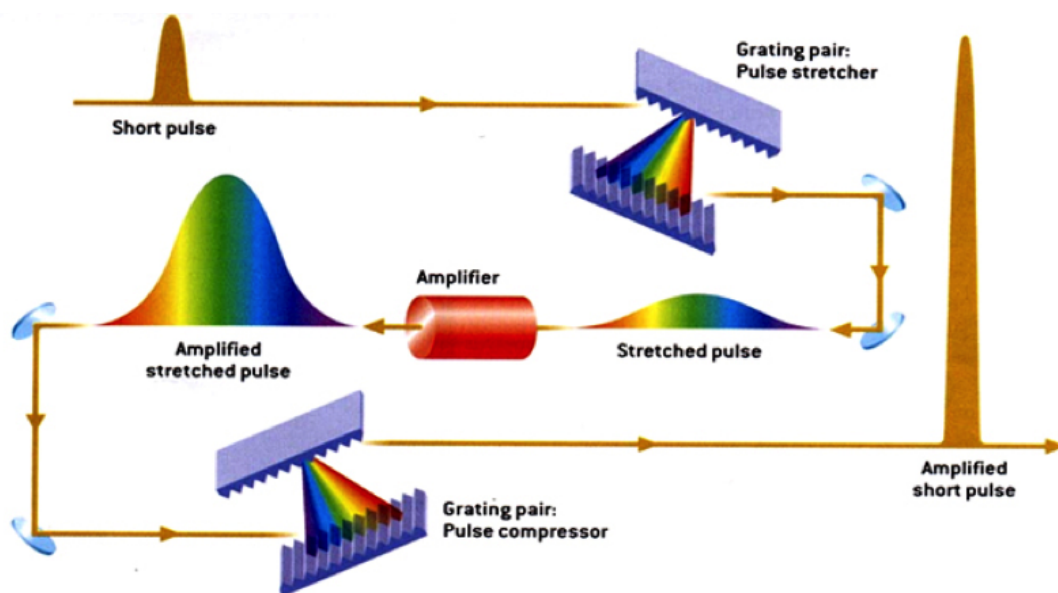


Figure 2.2: Schematic representation of the CPA scheme [source: <https://www.nobelprize.org/uploads/2018/10/popular-physicsprize2018.pdf>].

The schematic of the CPA is shown in Figure 2.2. In this Ti:Sapphire based system (TSA-10, Positive Light), mode-locked 100 fs pulses from the ultrafast oscillator at the repetition rate of 82 MHz are initially sent to a grating stretcher, where the pulses are broadened to 300 ps temporal width. Then an individual pulse is picked from the pulse

train using an electro-optic modulator and seeded into a regenerative cavity, which contains an optically pumped Ti:Sapphire crystal as the amplifying medium. The principle of regenerative amplification is to confine a single pulse (selected from a mode-locked pulse train) by polarization, amplify it to an appropriate energy level, and then "cavity dump" the output. The pulse which oscillates in the regenerative cavity gains energy in each trip as it passes through the crystal. After several round trips, when the pulse gains sufficient energy, it is reflected out of the cavity using an electro-optic switch. Typically, an input pulse of energy of a few nJ can be amplified to over 5 mJ by this method. The cavity-dumped pulse is then fed to another Ti:Sapphire crystal (in the linear double-pass mode) for further amplification. The pulse is then sent to a grating compressor, which compresses the pulse back to the original 100 fs width. TSA-10 can generate 100 fs pulses of 10 mJ energy at a repetition rate of 10 Hz.

As mentioned, diffraction gratings are used for stretching and compressing the ultrafast pulses in the TSA-10. Ultrafast pulses have a large spectral bandwidth: a 100 fs pulse at 800 nm typically has a FWHM width of 12 nm. When this pulse is incident on a diffraction grating at an angle, different frequencies in the ultrafast laser pulse will get dispersed. In the TSA-10 the stretcher grating is configured in such a way that the bluer frequency components have to travel farther than the redder components, so that the pulse is stretched temporally to 300 ps. Pulse compression is essentially the reverse of pulse stretching. For compression the grating is arranged such that the bluer frequencies travel a shorter path compared to the redder frequencies, so that the pulse gets compressed back to 100 fs.

The ultrafast amplifier is a passive system, and needs to be pumped by an external source. For this we use the short pulse laser which is described below.

2.3 Short pulse laser source

We have used a frequency-doubled, Q-switched Nd:YAG laser (*Quanta-Ray*, Spectra-Physics) operating at 10 Hz with a pulse width of 7 ns as the short pulse laser source. The schematic representation of Nd:YAG laser and the four level energy diagram is

shown in Figure 2.3. This flash lamp pumped laser is capable of producing pulses of 275 mJ energy at 532 nm using a KDP crystal for frequency doubling. In fact this laser is a part of the ultrafast laser system, and is used for pumping the ultrafast amplifier. However, since our ultrafast system has a modular design, we can use this laser separately for generating short pulse LPPs as well.

Neodymium-doped yttrium aluminium garnet (Nd:YAG) is a popular four-level solid-state laser with broad applications. Triply ionized neodymium ions serve as the active medium. Optical pumping excites electrons to a higher energy state, which has a lifetime of 230 s. Thereafter they drop to the upper lasing level of ${}^4F_{3/2}$, from which the electrons relax to the lower lasing level ${}^4I_{11/2}$. The radiative transition from ${}^4F_{3/2}$ to ${}^4I_{11/2}$ gives photons at 1064 nm.

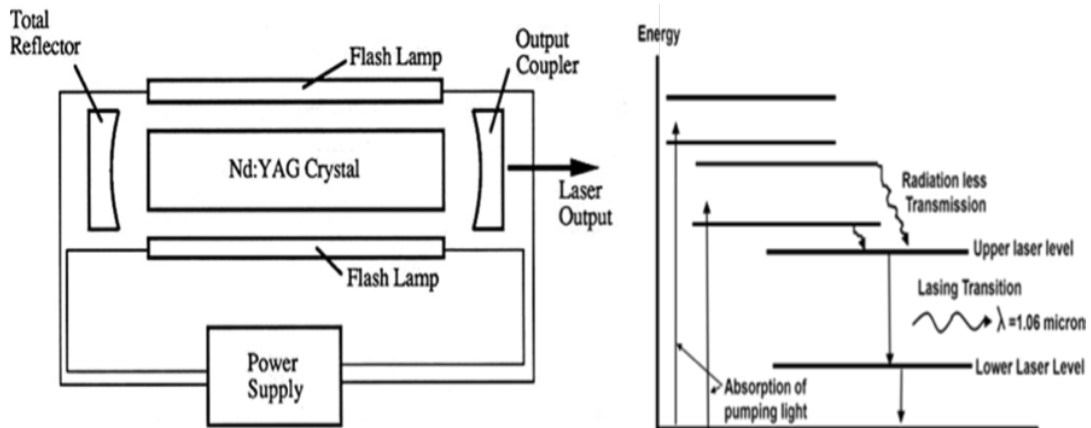


Figure 2.3: (a) Schematic representation of Nd:YAG laser system, (b) the four-level energy diagram [source: <http://www.aml.engineering.columbia.edu/ntm/level1/ch05/html/11c05s07.html>].

In a Q-switched Nd:YAG laser the laser cavity includes of a polarizer, a Pockels cell and a quarter-wave plate, in that order. The Pockels cell is an electro-optic crystal which becomes birefringent when a high voltage is applied to it. The flash lamp excites the gain medium for about $200 \mu\text{s}$, resulting in substantial population inversion. The polarizer horizontally polarizes the light, which passes through the Pockels cell to the quarter wave plate. When Q-switch is not activated (i.e., when no voltage is applied) the Pockels cell is passive in the cavity. The quarter-wave plate converts horizontal polarization into circular polarization. As the circularly polarized light comes back

after reflection from the end reflector, the quarter wave plate converts it into vertically polarized light. Since the polarizer transmits only horizontally polarized light, it will reflect the vertically polarized light out of the resonator, so that there is no laser output.

However, during Q-switch operation, a fast high voltage will be applied to the Pockels cell at the time of maximum population inversion. The Pockels cell becomes birefringent, and will convert the vertically polarized light coming from the quarter-wave plate into horizontal polarization. This horizontally polarized light will be passed by the polarizer, which gets amplified in the gain medium. As a result, the laser pulse width will be shortened to 7 ns, and the output peak power will be raised to Megawatt levels.

2.4 Experimental environment

The ambient pressure is very important in the formation, evolution, and dynamics of laser produced plasmas. The essential components of the experimental environment are the vacuum chamber, dry pump, turbomolecular pump, solid target manipulator and target motion controller. Low pressure background minimizes energy transfer from the plasma to the ambient. We have generated laser plasmas at ambient pressures ranging from 10^{-5} to 760 Torr. For efficient detection of ions generated in the plasma, high vacuum of the order of 10^{-6} Torr is desirable.

2.4.1 Vacuum chamber

The vacuum chamber used for the experiments comprises of two chambers which are linked. The main chamber is 1 meter in diameter, 40 cm in height and has a volume of approximately 300 liters. There are 16 ports in this chamber. The smaller chamber is 75 cm in length and 30 cm in width with four ports. The targets were kept in the smaller chamber during the experiments.

2.4.2 Dry pump and Turbo Molecular Pump (TMP)

The use of rotary pumps will leave a layer of oil on the target surface affecting the surface quality, especially on polished and coated surfaces. Our chamber is pumped

using a turbo molecular pump (Pfeiffer, model TPU 2101 PC, 2000 rev/s) backed by a dry pump (Pfeiffer, model Unidry DBP 050-4, 180 rpm) to obtain oil-free vacuum. A TMP is made of a stack of rotors with blades, or slots, depending on the specific pump. In between the rotor disks are the stators, which are fixed discs that contain the same blades as the rotors, but oriented in the opposite direction. The TMP works by transferring kinetic energy to the gas molecules by using these angled blades that propel the gas out as they rotate at high speeds.

The dry pump used as the primary pump can evacuate the chamber down to 5×10^{-2} Torr in about five to eight minutes. A Pirani gauge is used to measure the rough vacuum ranging from 750 Torr to 10^{-3} Torr. Lower pressures in the pressure range of 10^{-3} - 10^{-5} Torr are measured using a cold cathode gauge. The turbo molecular pump in conjunction with the dry pump can pump the chamber down to 1×10^{-6} Torr in about twenty-five minutes.

2.4.3 Solid target manipulator and Target motion controller

The solid target needs to be moved after every laser shot to produce plasma from a fresh sample surface. For this we use a stepper-motor controlled XY translation stage fixed outside the vacuum chamber, which is attached via a Wilson seal to the vacuum compatible target holder fixed inside the chamber. This solid target manipulator is attached to a 100 CF port located on the top of the chamber. It can be moved in both horizontal and vertical directions (50 mm in both directions) with an accuracy of 12.5 micrometers.

The stepper motor of the target manipulator can be controlled and synchronized with the laser pulses for accurate measurements. Precise motion in the X and Y directions is achieved by a custom-made electronic circuit controlled by a LabVIEW program. Control signals from the PC to the target manipulator are transferred via the LPT port (parallel port). Since the stepper motor requires relatively high currents to run, a buffer amplifier is included in the circuit.

2.5 Detectors

2.5.1 Spectrometer

Emission from the plasma is collected using the imaging system and focused onto the entrance slit of a Czerny-Turner spectrometer (iHR320, Horiba Jobin Yvon), which has provision for fixing a CCD detector as well as a PMT (photomultiplier tube) detector at the exit is shown in Figure 2.4a. The compact CCD detector is from Horiba Jobin Yvon (*Synapse*) and the PMT is from Hamamatsu (*R943-02*, rise time 3 ns). The CCD can record the emission spectrum while the PMT can record the optical time of flight (OTOF) of the plasma constituents. The iHR320 is an automated grating spectrometer with a focal length of 320 mm ($f/4.1$ aperture). The on-axis grating turret, mounted on a drive, supports three gratings with different resolutions. These can be individually selected via an *Origin* program written in the Visual BASIC platform. The maximum resolution achievable is 0.06 nm, and the spectral range is 200 nm to 1500 nm. The inner layout is shown in Figure 2.4b.

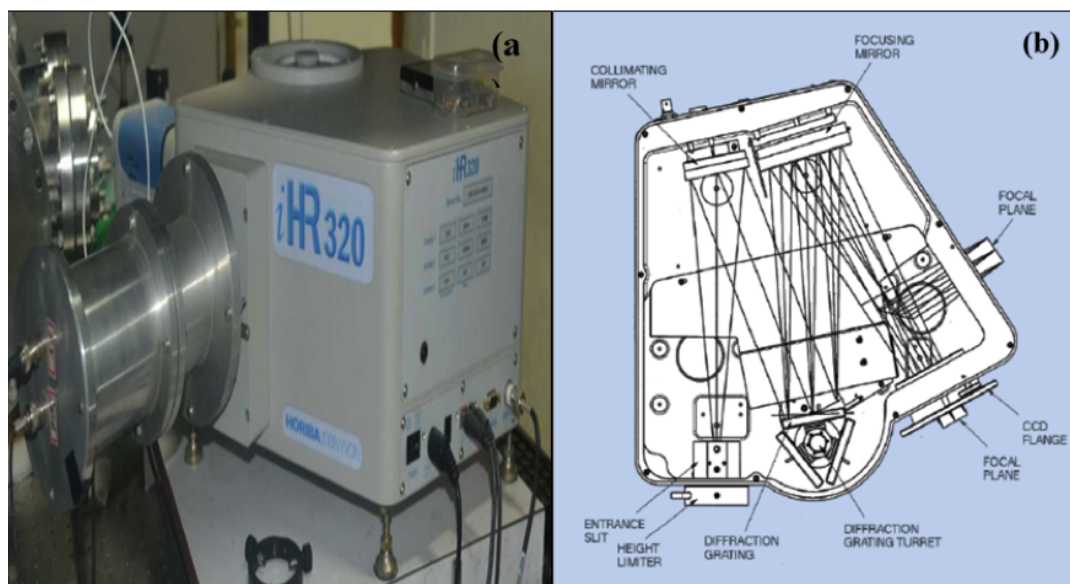


Figure 2.4: (a) Photograph of the iHR320 spectrometer equipped with CCD and PMT detectors. (b) The inner layout of the spectrometer [source: <http://www.horiba.com/scientific/products/osd/optical-components/spectrographs-and-monochromators/ihr-series-spectrographs/>].

2.5.2 Digital Phosphor Oscilloscope

A digital phosphor oscilloscope (DPO7354, Tektronix) is used for displaying and measuring the optical time of flight (OTOF) signals acquired by the PMT. This fast DPO has an analog bandwidth of 3.5 GHz, and a real-time sampling rate of 40 GS/s when only a single input channel is in operation. The real-time sampling rate reduces to 10 GS/s when all four input channels are taking data simultaneously. Since the rise time of this DPO (110 picoseconds) is an order of magnitude shorter than that of the PMT, it can display the OTOF signals accurately.

2.5.3 Intensified charge coupled device (ICCD) detector

The intensified charge coupled device (ICCD) is an excellent imaging device capable of fast time-gated data acquisition. From ICCD images taken at regular time intervals, features of plume expansion can be directly investigated. An ICCD is a CCD that is optically connected to an image intensifier that is mounted in front of the CCD. The image intensifier includes three functional elements: a photocathode, a micro-channel plate (MCP) and a phosphor screen. Photons coming from the light source generate photoelectrons from the photocathode, which are accelerated towards the MCP by an electrical control voltage. Electrons are multiplied inside the MCP channels and then accelerated by a constant high voltage (5-8 kV) towards the phosphor screen. The phosphor screen finally converts the multiplied electrons back to photons, which are then guided to the CCD either by a fiber optic bundle or by a lens. The high gain in the optical domain is the important feature that distinguishes an ICCD from the regular CCD.

We used one of the best commercial ICCDs available (istar CCD 334, Andor Technology Ltd.) for imaging the plasma. The ICCD is equipped with a 1024×1024 array, and can be triggered by a 1.5 V pulse. Images can be acquired after a delay of 50 ns with respect to the trigger pulse. Minimum gate width is 200 picoseconds and minimum gate delay is 2 nanoseconds. The application software is Andor SOLIS, and the communication is performed via an RS232 serial interface.

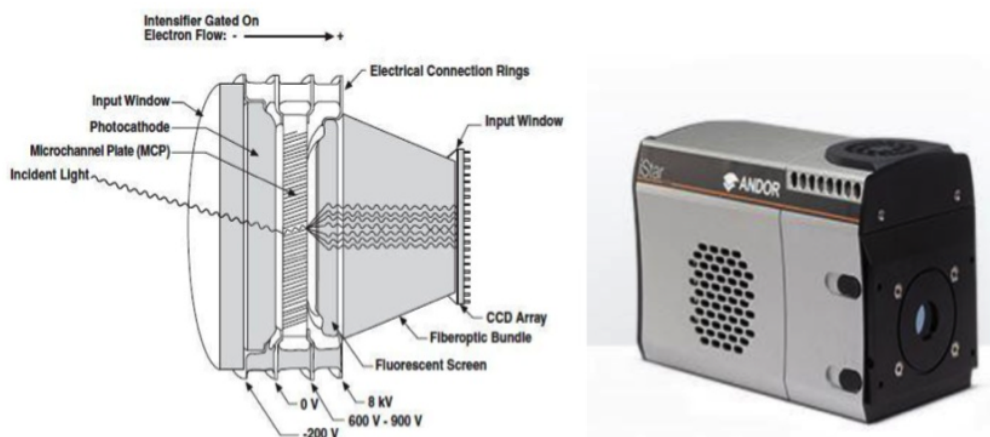


Figure 2.5: Schematic diagram of an ICCD, and photograph of Istar CCD 334 from Andor Technology [source: <https://andor.oxinst.com/products/istar-inten-sified-cameras>].

When the ICCD is operated in the time-gated mode, time-resolved snapshots of expanding plasma plumes can be recorded by acquiring single-shot photographs of the plume in the x - z plane. From 2D imaging of a three-dimensionally expanding plasma, processes happening at different time scales (plume splitting, instabilities etc.) can be recorded. All images recorded are found to be fairly symmetric about the surface normal. From plume imaging done at various ambient pressures for ultrashort and short pulse laser irradiation, the corresponding angular distributions of the expanding plumes also can be determined.

2.5.4 Faraday Cup

The Faraday cup is an electrically biased metal cup which can be used to collect charged particles from a plasma plume (Figure 2.6). The collected ions or electrons will form a current which can be measured. We used a Faraday cup from Kimball Physics Inc. (model FC-71A) which consists of a hollow copper cylinder with a mesh in front of it. The charge collection area is 5 mm^2 , and an outer cylinder which is grounded provides shielding. The base of the Faraday cup is attached to a BNC connector from which the signal can be taken out through a vacuum feed through, to be measured on an oscilloscope. The voltage bias on the Faraday cup reduces scattering of electrons or ions collected in the cup, as well as secondary electron emission. Typically, -30 V is applied

for positive ions, while for electrons and negative ions it is +30 V.

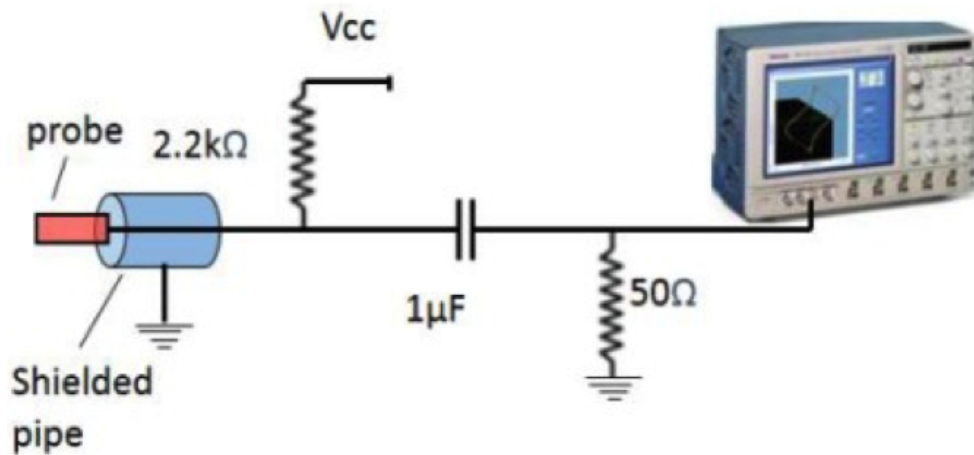


Figure 2.6: Schematic diagram of an ion probe circuit.

2.5.5 X-ray detector



Figure 2.7: The X-ray spectrometer X-123 CdTe [source: <http://amptek.com/products/x-123-cdte-complete-x-ray-gamma-ray-spectrometer-with-cdte-detector/>].

X-ray emission from the plume was measured using a CdTe X-ray detector (model X-123CdTe from Amptek) as shown in Figure 2.7. It combines in a single package the XR100T-CdTe detector and pre-amplifier, DP5 digital pulse processor and MCA, and PC5 power supply. It has 4 mill Be window and 9 mm² detector area. The detector has

an optimum energy range from 5 keV to 150 keV. It also has a two-stage thermoelectric cooler similar to Si: PIN X-ray detector. The thermoelectric cooler reduces the electronic noise in the detector and pre-amplifier. The semiconductor-based detector works by photoelectric effect when the X-rays interacts with the CdTe crystal. The electrons are collected and the current generated can be used to measure the X-Ray emissions.

2.6 Laser pulse characterization

2.6.1 Spectral characteristics

Since the ultrafast pulse is generated by mode-locking a large number of laser cavity modes, it is broad in the spectral domain. For a Gaussian pulse, the relationship between the spectral and temporal width is given by $\Delta\nu\Delta t \geq 0.441$, which corresponds to a bandwidth ($\Delta\lambda$) of about 12 nm for a chirp-free pulse width and (Δt) of about 100 fs, at 800 nm wavelength, as shown in Figure 2.8.

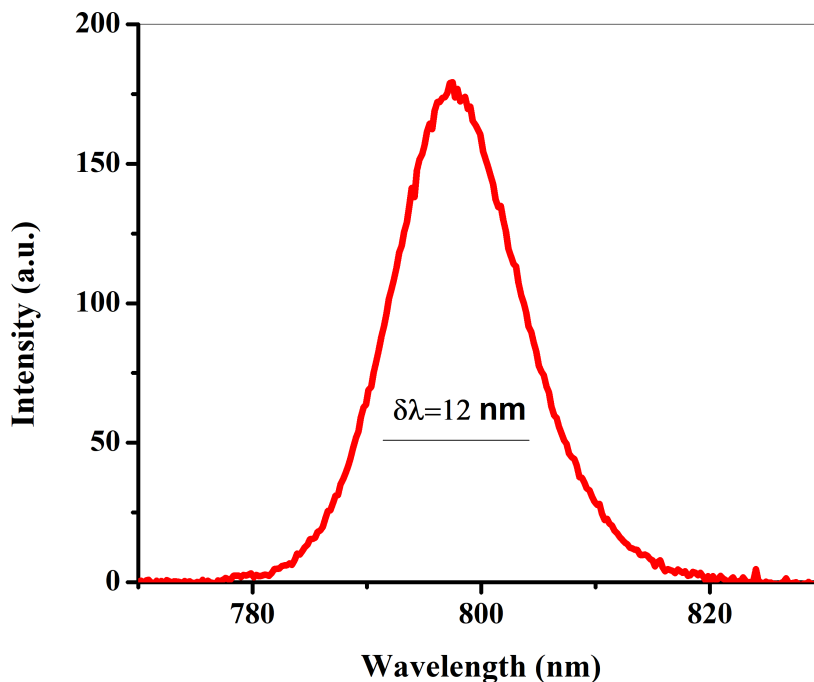


Figure 2.8: Wavelength spectrum of the ultrafast laser pulse.

2.6.2 Spatial intensity profile of the laser pulse (knife edge method)

The cross-sectional intensity profile of the laser beam is an important parameter, which is crucial in determining the focused spot size as well as the irradiance of the beam. The conventional knife-edge method can be used to determine the spatial intensity profile of the laser pulse. In the knife-edge method, a knife-edge is scanned across the transverse profile of the beam and the energy passing the knife-edge is recorded using an energy detector. The detector output corresponds to the integrated intensity, which when differentiated gives the input laser spatial profile. Assuming the laser spatial profile to be a Gaussian, the beam diameter can be calculated by fitting a Gaussian to the derivative of the energy meter output. The actual beam diameter of ultrashort and short laser pulses calculated using the knife-edge method are 9.4 mm and 8.5 mm respectively.

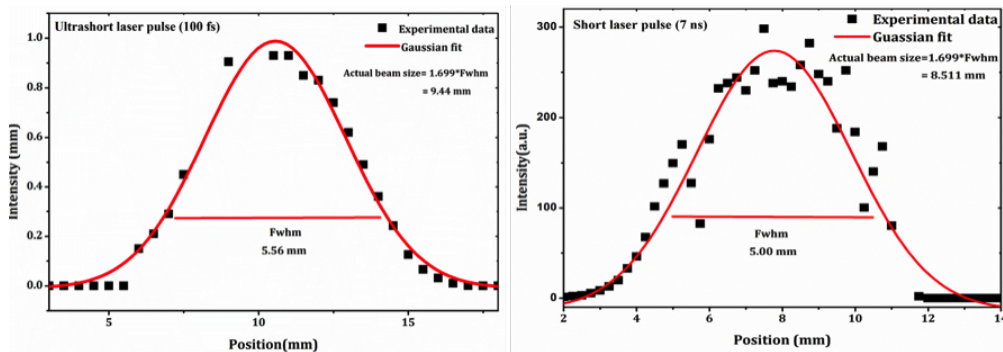


Figure 2.9: Actual beam size of ultrashort and short laser pulses measured using the knife-edge method.

For measuring the spot size (radius of the beam at the focus) of the beam at the focal point of a focusing lens, knife-edge measurement is done at the minimum spot size position. The spot size of the ultra short and short pulse is nearly $90 \mu m$, and $209 \mu m$ at the focus.

2.6.3 Spatial intensity profile of the laser pulse (beam imaging)

A spatial beam profiler (BeamLux II, Metrolux, USA) also was used to measure the spatial profile of the laser beam. The beam diameter can be measured using the beam profiler, by calibrating the pixel size. BeamLux II is well suited for all pulsed and continuous wave light sources, and image sizes ranging from a few μm to a few mm can

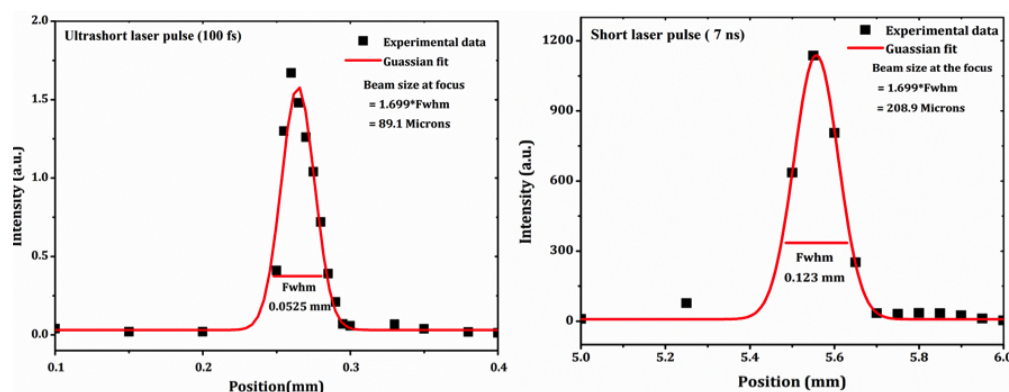


Figure 2.10: Beam size at the focus (focal length of lens 40 cm) for ultrashort and short laser pulses respectively, measured by the knife-edge method.

be investigated within an optimum resolution of 6.5 microns. It operates over a broad wavelength range $\sim 320 - 1100$ nm. The beam diameter at the focus of ultrashort and short laser pulse (7 ns) measured using BeamLux were $86.7\mu\text{m}$ and $221.8\mu\text{m}$ respectively when a 40 cm lens was used, which matches well with the value obtained from the knife-edge measurements. The horizontal cross section and profile of the ultra short and short laser pulse beam is shown in Figures 2.11 and 2.12.

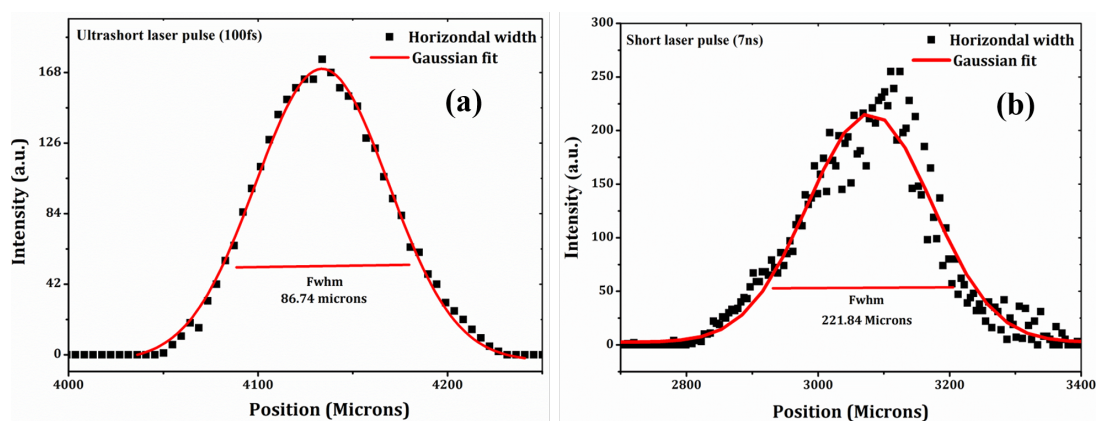


Figure 2.11: Horizontal cross-section of the beam at the focus obtained from the beam profiler (a) Ultrashort pulse (100 fs) (b) Short pulse (7 ns).

From the results it is clear that the focal spot sizes obtained from the beam profiling and knife-edge methods are almost similar.

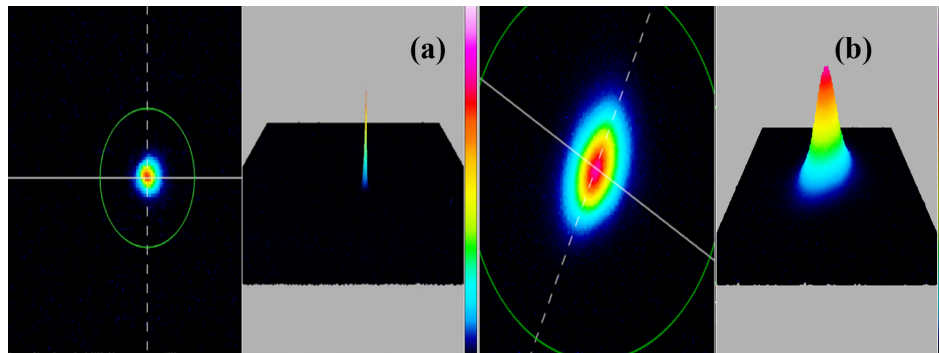


Figure 2.12: Profile of the beam obtained using a BeamLux beam profiler (a) Ultrashort pulse (100 fs) (b) Short pulse (7 ns).

2.7 Optical Emission Spectroscopy (OES)

Optical Emission Spectroscopy (OES) is a useful non-destructive spectroscopic technique, which can be used for the characterization of laser produced plasmas. The energy of the laser pulse, the sensitivity, the wavelength range of the spectrograph and the detector are important in OES. Because of its remarkable features, OES is used to study a wide range of materials like metals, alloys, biological samples, pollutants, explosives, etc. It is an important technique used in Laser-Induced Breakdown Spectroscopy (LIBS) for detecting unknown samples. From the optical emission spectra, key parameters such as electron temperature and number density of the plasma can be calculated.

2.7.1 Calculating the electron temperature (T_e)

The temperature of the plasma can be calculated either by the ratio of the line intensity method or via the Boltzmann plot method. Temperature calculations are performed by assuming the plasma to be in Local Thermodynamic Equilibrium (LTE). Under a valid LTE, different temperatures of the plasma such as ion temperature, electron temperature, and neutral temperature are considered to be approximately equal. We evaluated electron temperatures (T_e) using intensity ratios of line emissions from similar species emitting two different wavelengths, which are relaxing to the same lower energy state. Assuming local thermodynamic equilibrium (LTE) in the system, the temperature is

estimated using the equation (Rumsby and Paul, 1974; Griem 1964),

$$\frac{I_i}{I_j} = \frac{g_i A_i \lambda_j}{g_j A_j \lambda_i} \exp\left(-\frac{E_i - E_j}{K_b T_e}\right) \quad (2.1)$$

where $\lambda_{i,j}$, $A_{i,j}$, $g_{i,j}$, $I_{i,j}$ and $E_{i,j}$ are the wavelength, transition probability, statistical weight, line intensity and energy of the excited state respectively.

2.7.2 Calculating the electron number density (N_e)

The electron number density (n_e) is evaluated from Stark broadening of line emission at a particular wavelength using the equation (Rumsby and Paul 1974; Harilal 1997; Griem 1974),

$$\Delta\lambda_{1/2} = 2w\left(\frac{n_e}{10^{16}}\right) + 3.5A\left(\frac{n_e}{10^{16}}\right)^{\frac{1}{4}} \times \left(1 - \frac{3}{4}N_D^{-\frac{1}{3}}\right)w\left(\frac{n_e}{10^{16}}\right)A^0 \quad (2.2)$$

where $\Delta\lambda_{1/2}$ is the full width at half maximum (FWHM) of emission, w is the electron impact parameter, N_D is the number of particles in the Debye Sphere, and A is the ion broadening parameter.

In addition to Stark broadening, broadening mechanisms such as Doppler broadening and pressure broadening also will contribute to line broadening in LPPs. Instrumental broadening is another factor which can increase measured line widths. Doppler broadening arises due to different velocity components in different regions of the plume. Typical FWHM of Doppler width in LPP is always one or two orders of magnitude less than that of Stark broadening. Pressure broadening depends on the ground state number density and oscillator strength of the transition, and normally it is neglected since it is very small. Instrumental broadening can be minimized by reducing slit widths in the spectrometer. For non-hydrogenic ions, Stark broadening is dominated by electron impact, and therefore the ion correction factor is negligible. Therefore the Stark broadening equation reduces to (Griem 1974; Harilal et al. 1997),

$$\Delta\lambda_{1/2} = 2w\left(\frac{n_e}{10^{16}}\right)A^0 \quad (2.3)$$

The theoretical value of ω is obtained from the literature. A Lorentzian curve fits the emission profile for a given wavelength. Knowing ω corresponding to the estimated number density n_e can be calculated.

The validity of LTE can be checked using the McWhirter criterion for each case independently, which in the case of electrons is given as (Griem 1963; Cristoforetti et al. 2010)

$$n_e \geq 1.6 \times 10^{14} T_e^{\frac{1}{2}} \Delta E^3 \text{ cm}^{-3} \quad (2.4)$$

where ΔE is the energy difference between upper and lower energy levels in electron volts, and T_e is the electron temperature in eV.

If the value of N_e calculated using the above equation satisfies this inequality then LTE approximation is valid. In a transient system like the plasma, LTE is valid only when the collision time between particles is low compared to the time duration where significant changes occur in the plasma.

2.8 Optical time of flight measurements (OTOF)

Different methods are available to measure the time taken by an object or particle to travel a distance through a medium, which is called a time of flight measurement (Marine et al, 1992; Campbell et al. 1978). In the present study, the time taken by different species of the plasma (electrons, ions or neutrals) to travel a certain distance is measured using spectrometer, PMT and a digital oscilloscope. Time and space resolved line emission spectroscopic information is an effective tool to estimate the velocities of ions and neutrals moving in an expanding LPP. Recombination and ionization mechanisms

present in expanding LPPs are studied by OTOF in the present work. OTOF studies of ions and neutrals along the expansion direction (i.e., normal to the target surface) for a large range of ambient pressures are also done. As different species give distinct lines in the spectrum, the species to be monitored is set by configuring the spectrometer to the corresponding wavelength.

2.9 ICCD Imaging Technique

ICCD imaging is a robust method to investigate the spatial and temporal evolution of plasma plumes (Whitty and Mosnier 1998;Geohegan and Puretzky 1996). Plume morphology details such as plume sharpening, plume splitting and instability also can be studied from the plume images. Expansion dynamics of LPP can be investigated by acquiring single-shot photographs of plume emission in the x-z plane using an intensified charge coupled device (ICCD) operating in the time-gated mode. The position-time plot for the leading edge of the plume emission is evaluated from the ICCD images. At each delay, the plume front position is identified from the 80% of the decay position of vertical cross-section profile of the plume. In vacuum the plasma exhibits free expansion, fitting to a linear model. The absence of deceleration indicates free expansion of the plume. When the background pressure is increased the plume velocity gets reduced. Depending on the pressure range the plasma expansion dynamics can be analysed using different models, of which the two major ones are the shock wave and the drag force models.

According to the shock wave model, the expansion length of the plume is controlled by the background pressure (Gonzalo et al. 1995;Sharma and Thareja 2005). This model is valid only when the mass of the gas surrounding the shock wave is higher than the mass of the ablated material. Under the shock wave model, the distance R from the target surface at which maximum transient emission is observed is given as a function of time as,

$$R = \frac{k^{\frac{1}{5}}}{p} t^{\frac{2}{5}} \quad (2.5)$$

where k is a constant proportional to the laser energy density, and p is the ambient gas pressure.

The plasma plume experiences rapid expansion at the initial timescales, followed by deceleration, before finally coming to rest. Ambient gas pressure influences plasma dynamics and stopping distance significantly. At higher background pressures plasma expansion gets more affected. When the plasma moves at a speed that is close to the speed of sound, the plume experiences an opposing drag force that makes it stop after travelling a certain distance known as stopping distance. Therefore, at higher pressures, the plume expansion is better described by the drag model, which is given as (Gonzalo et al. 1995;Geohegan and Puretzky, 1996)

$$R = R_0(1 - \exp(-\beta t)) \quad (2.6)$$

where R_0 is the stopping distance of the plume and β is the slowing coefficient ($R_0\beta = v_0$).

2.10 Ion Time of flight studies

During laser ablation, ionization of the target occurs at the beginning of the laser pulse, generating electrons and ions according to the intensity. These charged particles are an essential part of the LPP. Langmuir probe and Faraday cup detectors have been widely used to diagnose low-temperature plasmas produced by pulsed laser ablation of solid targets (Pearlman 1977;Hopkins and Graham 1986). In the present study, we have used Faraday cup for diagnosing the ions present in the plume in vacuum. This diagnostic technique finds the plasma flow velocity, electron and ion fluxes and their velocities. The number of electrons flowing through the Faraday cup circuit per second is directly proportional to the number of charges being carried by the ions. The continuous beam of ions (each with a single charge) is given by (Hopkins and Graham, 1986;Verhoff et al. 2012)

$$N \times e = I \times t \quad (2.7)$$

where N is the number of ions observed during time t (in seconds), I is the measured current (in amperes), and e is the elementary charge ($1.60 \times 10^{-19}\text{C}$). The Digital phosphor oscilloscope is used to measure the ion current from the Faraday cup by triggering with a laser pulse from the photodiode.

2.11 X-ray measurements

Plasmas emit broadband radiation, including soft X-rays and hard X-rays. Measurement of X-ray emission is carried out using a calibrated CdTe detector. The detector is set to ‘gate in time’ with respect to the incident laser pulse to ensure background free data acquisition. The CdTe detector for X-rays and γ -rays (*Amptek* make) is placed normal to the target to collect the photons optimally. It requires only two connections to run: $+5\text{ V}_{DC}$ power and a standard RS-232 or USB bus. The X-ray yield is measured over 500 successive laser shots. The electron temperature of the plasma is calculated from the X-ray emission spectrum.

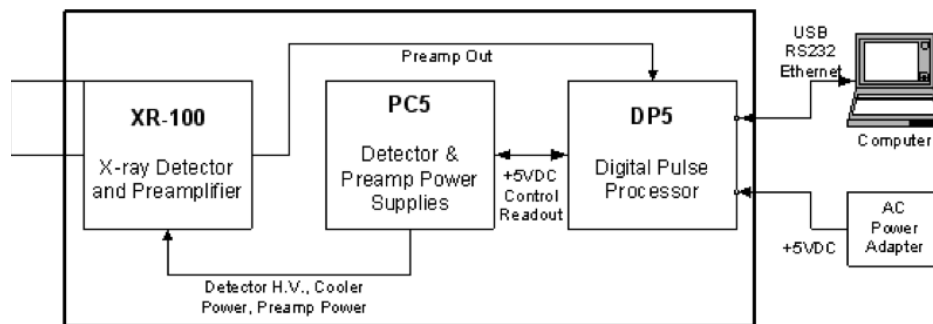


Figure 2.13: Connection diagram of Amptek 123CdTe X-ray Detector [source: <http://amptek.com/products/x-123-cdte-complete-x-ray-gamma-ray-spectrometer-with-cdte-detector/>].

The DP5 digitizes the pre-amplifier output, applies real-time digital processing to the signal, detects the peak amplitude (digitally), and bins this value in its memory, gen-

erating an energy spectrum. The spectrum is then transmitted over the DP5's interface to the user's computer. PC5 is a single board power supply for the X-ray detector. The input is approximately +5 VDC with a current of about 250 mA. PC5 uses switching supplies to produce all the low and high voltages required for the digital processor, the pre-amplifier and the detector.

In order to get the absolute photon energy corresponding to each pulse height, calibration of the detector is essential. Well-defined emission lines from standard radiation sources like ^{241}Am are used for calibration (Figure 2.14).

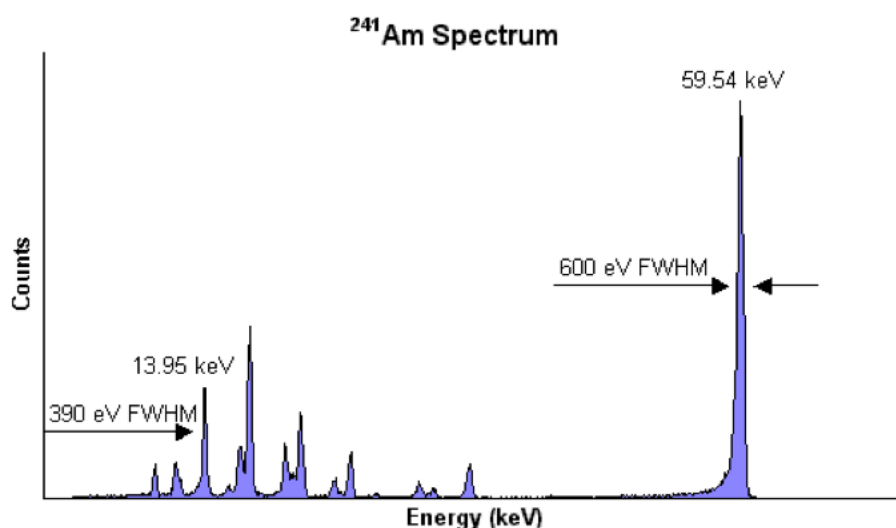


Figure 2.14: Calibration spectrum of ^{241}Am [source: <http://amptek.com/products/x-123-cdte-complete-x-ray-gamma-ray-spectrometer-with-cdte-detector/>].

2.12 Experimental set up at a glance

A chirped pulse amplifier (CPA) Ti:Sapphire laser (TSA-10, Spectra-Physics) delivering pulses of 120 fs width (FWHM) at 796 nm, and a Q-switched Nd: YAG laser producing 7 ns pulses at 1064 nm, are used in the current studies for the generation of plasma plumes. While both lasers were running at 10 Hz repetition rate, the experiment is carried out as a single-shot measurement by employing a fast mechanical shutter positioned in the beam path to select single pulses from the pulse train. A plano-convex lens of 40 cm focal length focuses the laser pulses. An unpolished Aluminum (99.95%

purity, ACI Alloys) of 5 cm x 5 cm size and Tungsten (Kurt J. lesker, 99.95% purity) of 1.00” Dia. × 0.125” Thick targets are kept in nitrogen background for the whole studies. The targets are translated by about 200 microns after each laser shot in order to avoid repeated ablation of the same spot. Emission from any axial position of the plasma plume could be collected using a lens combination that produces a 1:1 image on the entrance of the spectrometer. A grating spectrometer (iHR 320, Horiba Jobin Yvon) equipped with a CCD detector (Synapse, Horiba Jobin Yvon) and a fast Photomultiplier Tube (PMT) (R943-02, Hamamatsu) is used for the OES measurements. The integration time of the CCD is fixed at 100 ms. Time of flight data of the neutral and ionic species is measured by the PMT (with 3 ns rise time) and recorded on a digital phosphor oscilloscope (DPO 7354, Tektronix, 3.5 GHz bandwidth, 10 GS/s sampling rate) for further analysis. Moreover, to understand the plume dynamics, images were recorded at different time delays using an f/2.8 aperture lens (Nikon, Micro-NIKKOR-5mm) attached to the Intensified Charge Coupled Device (ICCD, Andor istar CCD 334).

The ion dynamics is measured using a negatively biased Faraday cup (Kimball Physics, Inc., model FC-71A). This device is kept at an angle of 20° with respect to the normal to the target surface, and the Faraday cup collector is located 11 cm away from its front aperture, so for FC measurements, an effective target-collector distance of 6.0 cm was considered. The output signal from FC is acquired across a 50Ω load resistor using a 3.5 GHz storage oscilloscope with a sampling rate 40 GS/s (DPO7354, Tektronix). A fast photodiode positioned near the window of the vacuum chamber triggered the oscilloscope to record the ion current signal from FC.

Measurements of hard x-ray emission in the 10keV-150 keV range performed with a calibrated CdTe X-ray detector (Amptek inc.). The CdTe detector has its gating to reduce the pileup data external gating was not required. The detector kept at a distance of about 25 cm from the target and at an angle is varied to optimize the X-ray emission. The cosmic ray background noise is reduced by using appropriate time gating. An unpolished Aluminium (99.95% purity, ACI Alloys) of 5 cm × 5 cm size and Tungsten (Kurt J. lesker, 99.95% purity) of 1.00” Dia. × 0.125” Thick targets are used for the

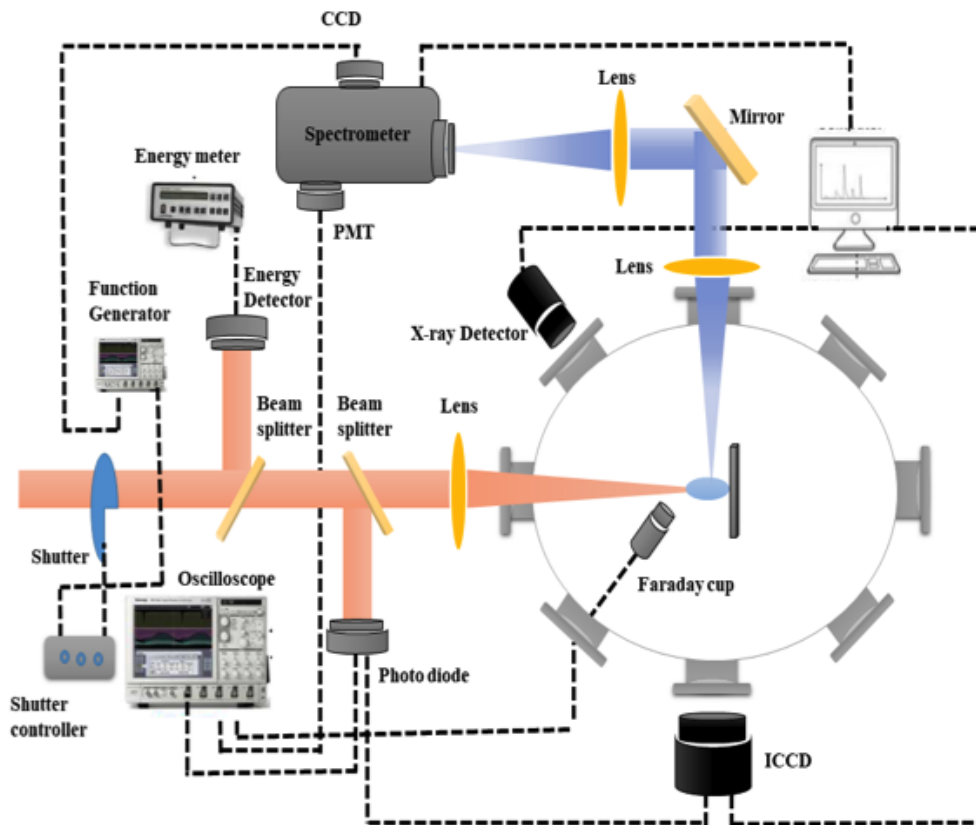


Figure 2.15: Schematic of the experimental set up used for optical emission spectroscopy (OES), OTOF spectroscopy, ICCD imaging, Ion studies and X-ray measurements.

measurements. The laser is p polarized and was incident on the sample at an angle of 90 degrees. The spectrum is collected over 5000 laser shots.

2.13 Summary

This chapter gives a description of the different instruments used for the experiments reported in this thesis. Experimental techniques used for the diagnostics of laser produced plasma are explained. Details of the experimental setups for the Optical emission studies (OES), Optical time of flight (OTOF), ICCD imaging, Ion emission studies and the X-ray emission studies are given in detail.

CHAPTER 3

LASER PRODUCED PLASMA FROM ALUMINIUM AT DIFFERENT AMBIENT PRESSURE

A detailed comparison study of ultrashort and short pulse laser produced aluminium plasma from a solid aluminium target in a nitrogen ambient is discussed in this chapter. Optical emission spectroscopy (OES) and Optical time of flight studies (OTOF) are carried out as a function of ambient pressure. We have explored the evolution and expansion dynamics of neutral and ion species in the plasma for a background pressure range of 10^{-2} to 760 Torr of nitrogen.

*“If you can’t explain it simply,
You don’t understand it well enough.”*

————— *Albert Einstein*

3.1 Introduction

Laser ablation has developed into an important area of research in recent years owing to various applications such as high harmonic generation (HHG, Ganeev 2009), pulsed laser deposition (PLD, Amoruso 2005), laser treatment of surfaces, nanoparticle generation (Amoruso et al. 2005), acceleration of neutrals and ions, and laser induced breakdown spectroscopy (LIBS, Cremers and Radziemski 2006). Future development of these applications requires a better understanding of the mechanisms of laser-solid interaction, formation of the plasma plume, and its expansion under vacuum or in an ambient gas. Even though much theoretical and experimental work has been done in laser produced plasmas (LPP) in the past, the processes involved in the plume expansion process are not yet understood completely. Plasma parameters not only depend critically on the nature and pressure of the ambient gas but also on laser parameters such as the pulse duration, wavelength, and fluence.

Laser ablation occurs a few picoseconds (ps) after irradiation whenever the fluence exceeds the ablation threshold of the material (Rethfeld et al. 2004). Since the electron collision time and heat conduction time are in the order of several picoseconds, the laser pulse does not interact with the plasma in ultrafast laser ablation (ULA, Gamaly et al. 2002). However, for short-pulse laser ablation (SLA), the ablated species interact with the relatively longer laser pulse, creating different plume characteristics. While Coulomb explosion is the prominent cause for plasma formation in ULA, thermal ablation and laser-plasma interaction are dominant in SLA. The nature of plume expansion and the propagation of its components will depend on the background gas pressure in both cases. In general, at low ambient pressures the plasma expands freely, while at higher pressures physical processes such as enhanced collisions, plume focusing, and

plume confinement will constrain expansion. Similarly, while Monte-Carlo simulations satisfactorily explain plume dynamics at low pressures, the shock wave model is appropriate at moderate pressures, and the drag model is suitable at higher pressures.

Even though a few studies have been reported for Aluminium LPPs in the past, a comprehensive comparison of the time of flight dynamics of Al plasma species (neutrals and ions) generated by ultrashort and short laser pulses has not yet appeared anywhere. Therefore, in the present work, we have employed ultrashort (100 fs) and short (7 ns) laser pulses for generating plasmas from a pure Al target for a background pressure range of 10^{-2} to 760 Torr of nitrogen. Plumes have been investigated using OES and OTOF. The relative abundances of neutral (Al I) and ionic (Al II, Al III) species present in the plumes, their spatial distribution along the plume axis, and their velocities have been determined. The role of background gas pressure on plume expansion is explored.

3.2 Results and Discussion

3.2.1 Optical Emission Spectroscopy (OES)

Material ablation will happen for any laser fluence that exceeds the threshold fluence of the material. The threshold fluence for ULA can be calculated using the equation (Gamaly et al. 2002)

$$F_{th} = \frac{3}{8}(\epsilon_b + \epsilon_{esc}) \frac{\lambda n_e}{2\pi} \quad (3.1)$$

where ϵ_b is the binding energy of the ions to the lattice, ϵ_{esc} is the work function, and n_e is the number density of free electrons. The corresponding values are 0.80 eV/atom, 4.28 eV, and 1.81×10^{23} electrons/cm³, respectively, for Al, λ (= 796 nm) is the wavelength of the laser. For SLA the threshold fluence is given by (Cremers and Radziemski 2006),

$$F_{th} \approx \rho \Omega D^{\frac{1}{2}} \tau_p^{\frac{1}{2}} \quad (3.2)$$

where ρ is the density of the material (2.7 g/cm^3), Ω is the latent heat of vaporization ($1.085 \times 10^4 \text{ J/g}$), D is the heat diffusion coefficient ($0.9628 \text{ cm}^2/\text{s}$), and τ_p is the laser pulse duration ($7 \times 10^{-9} \text{ s}$). D is given by $k/\rho C_p$ where k is the thermal conductivity and C_p is the specific heat. From the above, the ablation thresholds are calculated to be 1.01 J/cm^2 for ultrashort pulses, and 2.40 J/cm^2 for short pulses, respectively. The irradiation fluence used in the present experiments is $\sim 70 \text{ J/cm}^2$, which exceeds the above thresholds by a large margin. The intensities at this fluence are $7 \times 10^{14} \text{ W/cm}^2$ for ULA, and $1 \times 10^{10} \text{ W/cm}^2$ for SLA, respectively.

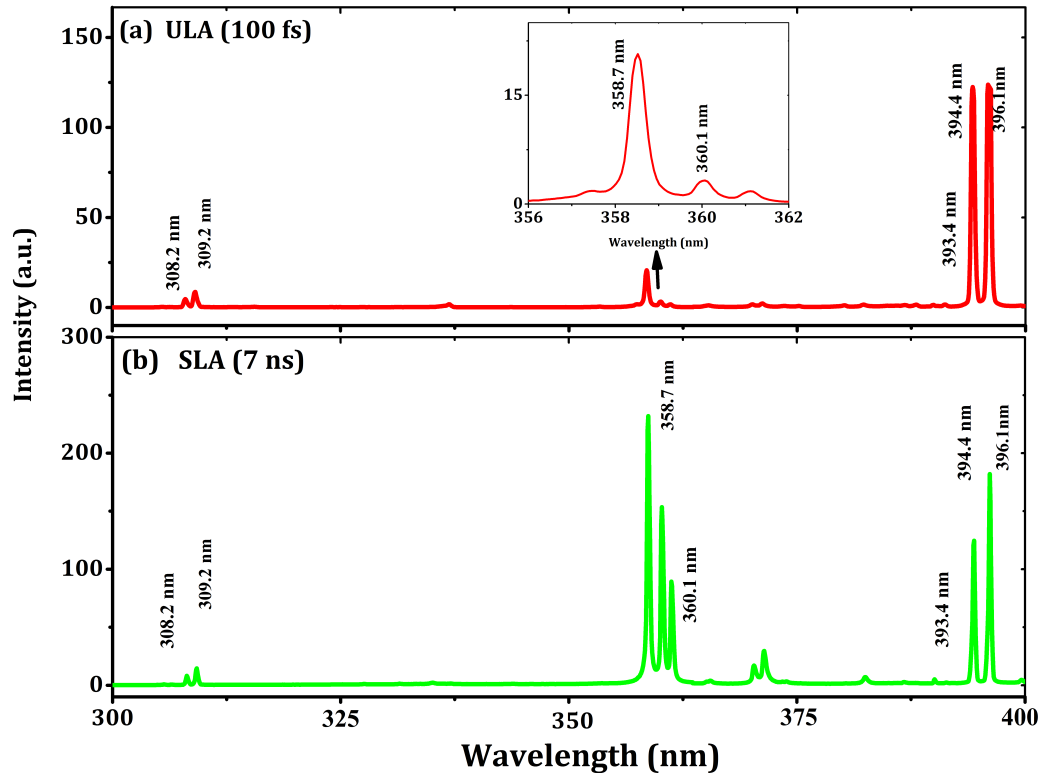


Figure 3.1: Spectra of optical emission from the plasma generated by (a) ultrashort and (b) short laser pulses for $z = 1 \text{ mm}$. Background pressure is 10 Torr. The net emission intensity is about five times higher for SLA compared to ULA. The 358.7 nm (Al II) and 360.1 nm (Al III) emissions are resolved in the inset shown in the top panel.

For SLA, irradiation of the target results mostly in thermal ablation, and subsequent laser-plasma interaction will result in enhanced ionization leading to a higher density of highly charged species. On the other hand, for ULA, the physical mechanisms responsible for plasma generation are Coulomb explosion, phase explosion, fragmentation,

and thermal ablation. Typical emission spectra measured for ultrashort and short pulse ablation are given in Figure 3.1. Emissions have been observed at 308.2 nm, 309.2 nm, 393.4 nm, 394.4 nm and 396.1 nm from Al I, at 358.7 nm from Al II, and at 360.1 nm from Al III (emission lines are verified with the NIST data base). From the various Al I emission lines the 396.1 nm line was chosen for OES and TOF studies. Several emission spectra were measured for various axial positions of the plume for a range of background pressures for characterizing ULA and SLA plasmas generated at the same laser fluence.

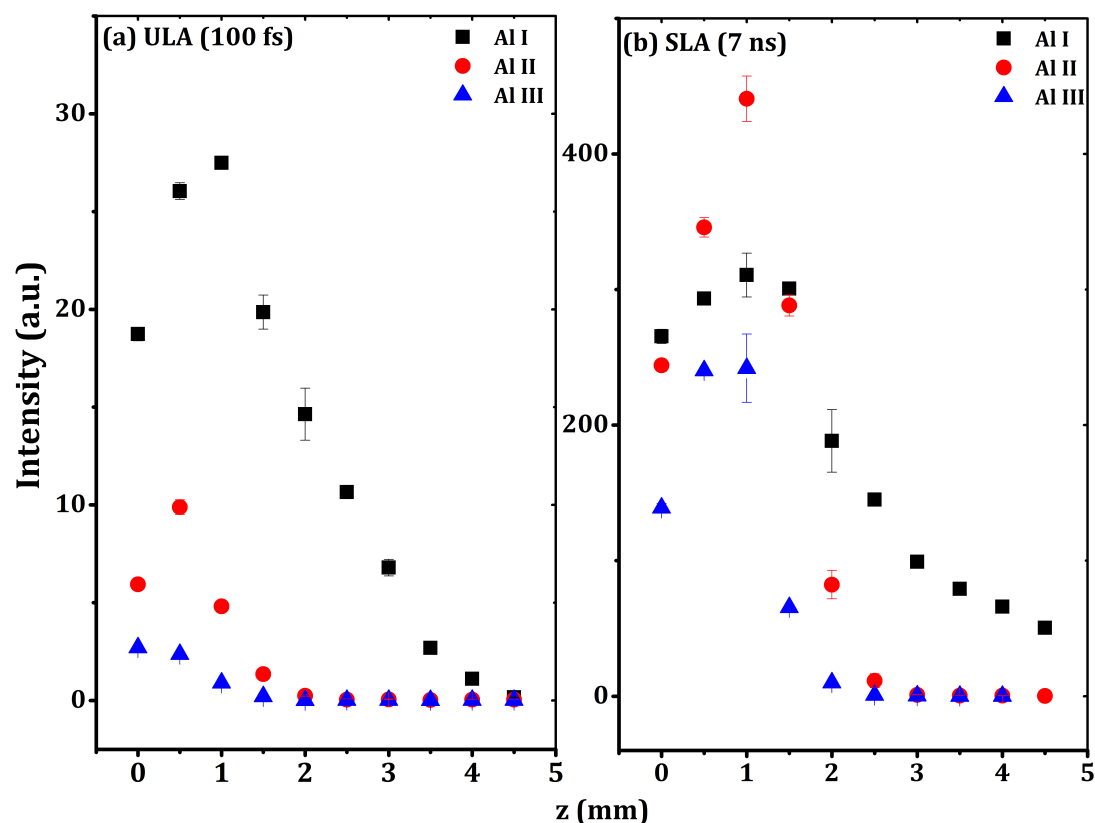


Figure 3.2: Emission intensity of Al I, Al II, and Al III estimated for different distances in the plasma plume from the target surface, from the corresponding emission spectra. The target is ablated using (a) ultrashort and (b) short laser pulses, respectively. Background gas pressure is 10 Torr.

Emission intensities from neutrals and ions measured along the plume axis, shown in Figures 3.2(a) and 3.2(b), show that the intensity is about an order of magnitude higher for SLA, compared to ULA. Emission from both neutrals and ions were mea-

sured up to $z = 5$ mm. For ULA neutral emission is found to be much stronger compared to ion emission. Intensity of Al II peaks at a distance of 0.5 mm from the target but that of Al I peaks at 1 mm, which indicates recombination during plume expansion. Al III intensity is a maximum close to the target, and decreases thereafter. Ion emission was substantial for SLA in comparison, and peak intensities were observed for neutrals, Al II and Al III at the same distance of $z = 1$ mm from the target surface. These observations corroborate the fact that laser-plasma interaction occurring in SLA is the cause for larger ion densities in the plasma. Essentially, the plasma created by the leading part of the laser pulse interacts with the remaining part, resulting in enhanced ionization of the plume. Though ion emission is strong near the target, it decays along the plume axis due to recombination during expansion, so that neutral emission is intensified.

The background gas pressure is one of the key factors that determine plume dynamics, and it plays an important role in plume splitting, sharpening, and confinement (Harilal et al. 2003). As seen from Figure 3.3, both ionic and neutral emissions increase and reach a maximum at 10 Torr in ULA, beyond which the intensity decreases. On the other hand, in SLA the neutral intensity keeps increasing beyond 20 Torr, while ion emission decreases. Since the plasma expands freely at low pressures, collisions will be negligible, but as the pressure increases from about 0.05 Torr onwards the plasma gets more confined and collisional processes will prevail. Electrons will lose energy to the background gas by elastic collisions, and the energy thus lost will be proportional to the elastic scattering cross section of the electron (σ_{ea}) and density of the background gas (n_B) through the equation (Rumsby and Paul 1974),

$$Q_{\Delta t} = \frac{2m_e}{M_B} \sigma_{ea} n_B \left[\frac{5KT_e}{\pi m_e} \right]^{\frac{1}{2}} \quad (3.3)$$

where M_B is the mass of the background gas and m_e is the electron mass. This energy loss will reduce the lifetime and emission intensity of the plasma. While electron-ion collisions will result in enhanced ionization, a higher rate of ion recombination also will occur at higher pressures. Ionization and recombination processes will balance each other at a certain intermediate pressure range where the emission intensity will

turn out to be a maximum. The intensity measured as a function of ambient pressure shows that this happens approximately in the range from 10 Torr to 20 Torr (Figure 3.3).

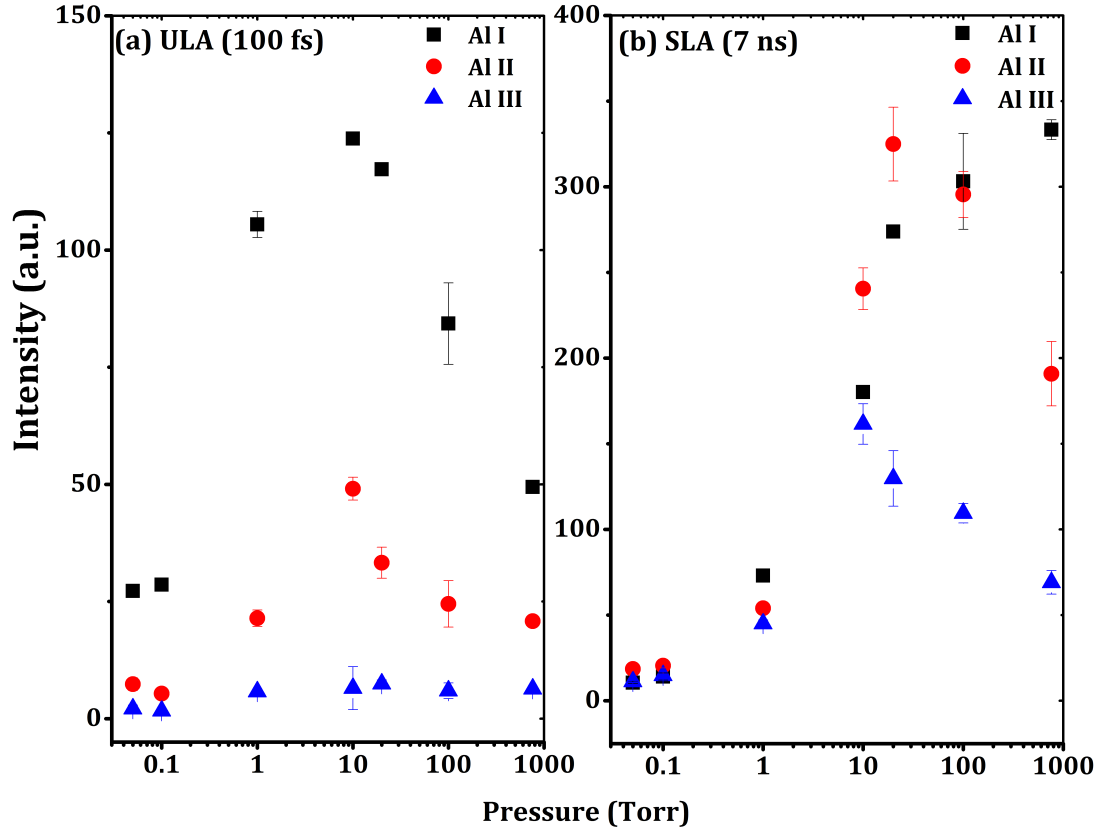


Figure 3.3: Emission intensity of Al I, Al II, and Al III measured for different background pressures, with (a) ultrashort and (b) short pulse laser ablations respectively, for $z = 1$ mm.

It may be noted that breakdown of the ambient gas into ions and electrons can occur when the pressure and laser energy are sufficiently high. The intensity threshold for air breakdown is approximately 3×10^{13} W/cm², and in the present ULA the intensity is an order of magnitude higher at 7×10^{14} W/cm². Therefore, part of the laser energy will be lost for directly ionizing the ambient gas near the target. Ambient gas ionization will happen due to hot electron emission from the target surface as well. These effects will result in a reduction of energy reaching the target. Similarly, in the case of SLA, the early plasma formed by the leading part of the laser pulse will absorb the remaining part of the incident laser pulse, decreasing the energy deposited on the target. These may be contrasted with ablation in vacuum where the ejected electrons will be propagated freely

into the surrounding space with negligible gas ionization and breakdown. Therefore, for a given intensity, the energy loss of the incident laser pulse will be lower in vacuum compared to that in air.

The temperature and number density will govern the kinetic and radiative properties of the plasma (Harilal et al. 1997; Rumsby and Paul 1974). Here, electron temperature T_e is evaluated using the Boltzmann line intensity ratio method, where we have considered emission from neutrals at 309.28 nm [$3s^23d^2D_{3/2} \rightarrow 3s^23p^2P_{3/2}$] and 396.15 nm [$3s^24s^2S_{1/2} \rightarrow 3s^23p^2P_{3/2}$], assuming local thermodynamic equilibrium (LTE). The line intensity ratio is given by (Cremers and Radziemski 2006),

$$\frac{I_1}{I_2} = \frac{g_1 A_1 \lambda_2}{g_2 A_2 \lambda_1} \exp\left[\frac{-(E_1 - E_2)}{K_B T_e}\right] \quad (3.4)$$

where λ_i , A_i , g_i , I_i and E_i ($i = 1, 2$) are the wavelength, transition probability, statistical weight, line intensity, and energy of the excited state respectively. K_B is the Boltzmann's constant. The spectroscopic constants (A_i and g_i) are taken from the NIST database. T_e estimated for different axial distances for both ultrashort and short pulse LPPs are shown in Figures 3.4.

Laser produced plasma is a powerful technique for generating ions, atoms, and molecules from a solid material. The species are formed in a high-temperature and high-electron density surroundings. These conditions lead to significant spectral line broadening. In addition, laser pulse duration, ambient pressure and laser fluence hardly affect the broadening of spectral lines in both ultrashort and short pulse LPPs, since the electric fields generated inside the plasma will perturb the energy levels of atoms and ions, shifting their energy levels. This resultant Stark broadening is the most common line broadening mechanism observed in LPPs. The spectral full width at half maximum (FWHM) of the emission line is directly proportional to the number density N_e , and is given by (Cremers and Radziemski 2006),

$$\Delta_{1/2} = 2\omega \left(\frac{N_e}{10^{16}} \right) \quad (3.5)$$

where $\Delta\lambda(1/2)$ is the FWHM of emission (in Å) and ω is the electron impact parameter. N_e can be determined from the above expression.

Near the target surface, electron temperature, T_e of short pulse LPP is almost double that of ultrashort LPP, but the temperatures are nearly equal at larger distances. The larger T_e observed for short pulse LPP can be attributed to plasma heating via laser absorption through the inverse Bremsstrahlung (IB) process. The IB absorption coefficient can be calculated from (Cauble and Rozmus, 1985),

$$\alpha_{ib} = 1.37 \times 10^{-35} \lambda^3 N_e^2 T_e^{-1/2} \quad (3.6)$$

where λ (μm) is the wavelength of the laser, T_e (K) is the electron temperature, and N_e (cm^{-3}) is the electron density.

From the figure 3.4, it is clear that electron temperature T_e decreases with axial distance, and the variation is similar for both excitations (Figure 3.4), even though T_e drops faster for short pulse LPP at larger distances. The outer region of the plasma interacts with the background transfers heat to the surroundings by adiabatic expansion. In the inner region of plume, thermalization of the ablated species by collisional excitation results higher temperature.

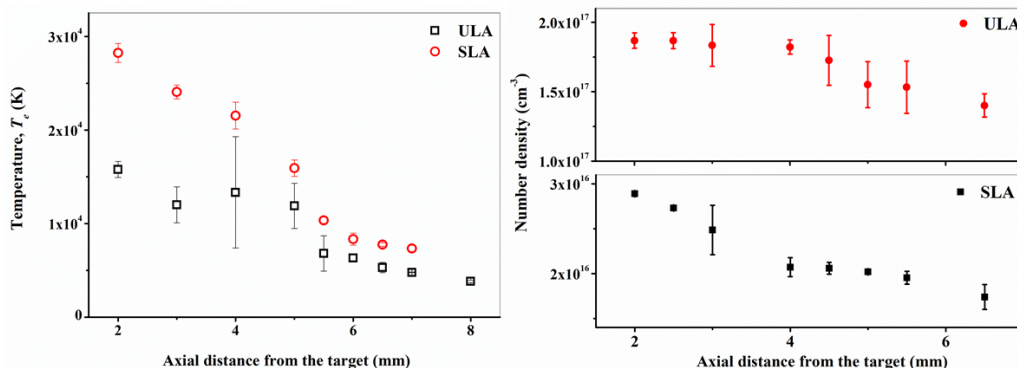


Figure 3.4: Variation of electron temperature (T_e) and number density (N_e) with axial distance for ULA and SLA measured at 10 Torr.

Figure 3.4 shows the number densities for ultrashort and short LPPs measured at 10 Torr nitrogen background. N_e is found to be higher for fs LPP compared to ns

LPP because of the three-body recombination of electrons with their parent ions. The efficient ablation in ultrashort LPP results in higher number densities, making three-body recombination significant (Harilal et al. 2014;Freeman et al. 2013a). Moreover, the plasma plume is confined along the horizontal axial expansion direction due to the self-generated magnetic field associated with intense irradiation. For ultrashort LPP, N_e remains nearly the same up to a distance of 4 mm and decreases linearly thereafter, which can be attributed to reduced collisional excitation and increased recombination on expansion. Laser-target coupling efficiency is high for ultrashort pulse LPP compared to short pulse LPP, and therefore the number density turns out to be higher.

The ambient gas also plays an important role in the plume confinement as well as excitation and re-excitation of species inside the plume (Freeman et al. 2013;Harilal et al. 2014). As mentioned above, the interaction of the expanding plume with the ambient gas leads to processes such as plume splitting, plume sharpening, collisional ionization, recombination, and plume cooling. To understand the effect of ambient gas pressure on T_e and N_e , we measured these parameters in the broad pressure range of 10^{-2} Torr to 10^2 Torr (below 10^{-2} Torr the plasma spectrum is nearly independent of the ambient pressure). Figure 3.5 shows the variation of plasma temperature with pressure. There is an increase in temperature when pressure increases from 10^{-2} to about 5 Torr, which can be correlated to plasma confinement and heating. Beyond 5 Torr T_e is found to be reduced, which should be due to collisions between plasma species and background gas, resulting in collisional recombination and thermal leak. The trend is found to be similar for both ultrashort and short pulse excitations.

On the other hand, variation of number density with pressure (Figure 3.5) shows different trends for short and ultrashort pulse excitations. Firstly, N_e is higher by almost an order of magnitude for ultrashort excitation. Secondly, while N_e remains nearly a constant in the pressure range of 0.05 Torr to 2 Torr, it decreases with further increase of pressure for short pulse excitation, and increases with further increase of pressure for ultrashort excitation. This can be explained as follows: when short pulse interacts with the target, plasma ejected by the leading part of the pulse will shield the target

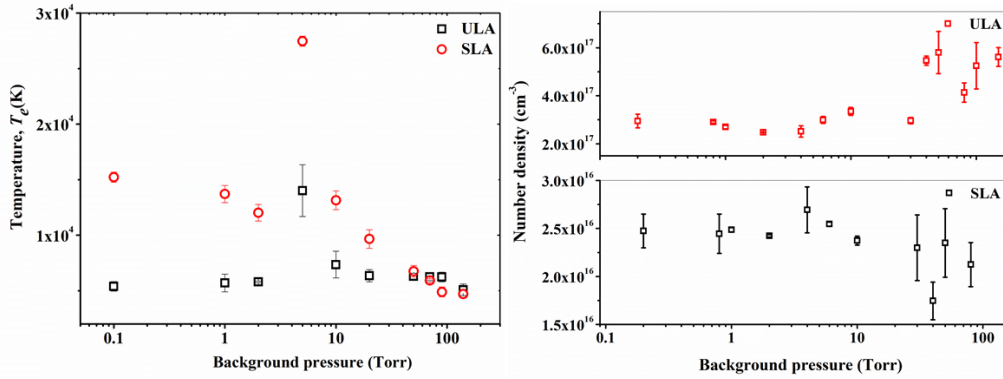


Figure 3.5: Variation of electron temperature (T_e) and Number density (N_e) with pressure, measured at a distance of 2 mm from the target surface, for a laser fluence of 70 J/cm^2 .

from further exposure, and the species will undergo multi-photon ionization and inverse bremsstrahlung by the trailing part of the pulse. Moreover, at higher ambient pressures plasma may be formed in the air volume close to the target surface also, augmenting the shielding effect. These will result in ineffective laser-target coupling so that the number density of species gets reduced at higher pressures. However, in ultrashort LPP, plasma shielding is absent and more plume confinement is observed. The resulting enhanced collisions among ablated species and with the ambient gas, will lead to an increase in the ionization of plasma species, causing the observed increase in N_e .

3.2.2 Time of Flight Studies

Time of flight (TOF) study is a useful tool for measuring the spatio-temporal propagation of different species present in expanding plasma plumes (Campbell et al. 1978; Marine et al. 1992). We have carried out optical TOF measurements of neutrals and ions at the wavelengths of 396.15 nm (Al I), 358.7 nm (Al II), and 360.1 nm (Al III). Figures 3.6 (a) and 3.6 (b) show TOF spectra measured for various axial distances (z) from the target surface, for ULA and SLA, respectively. It is found that neutrals as well as ions exhibit only a single band in ULA, for any given axial distance. However, in SLA two distinct bands can be seen, of which the first is relatively weaker and narrower, while the second is stronger and broader. The first band corresponds to faster plume components while the second band corresponds to slower components. For ions, the

fast component is produced by Coulomb explosion, while the slow component is produced by thermal ablation (Smijesh et al. 2016). On the other hand, for neutrals the fast component is produced by the recombination of fast ions with free electrons, while the slow component corresponds to un-ionized species resulting from thermal ablation (Smijesh et al. 2016). Distinct bands as seen in SLA are not seen in the TOF spectra of ULA, indicating that the velocities of the fast and slow components are quite close. The presence of distinct fast and slow species in SLA, as opposed to the apparent lack of such distinction in ULA, seems to be one of the major differences between ultrashort and short pulse LPPs.

The presence of a given species in the plume at any time, for a given position, can be identified from the corresponding TOF band. Figure 3.6 (a) reveals that Al I and Al II are seen up to $z = 3$ mm for ULA, while Al III is seen only up to 1.5 mm. Thus neutrals (Al I) last longer than Al II, which in turn last longer than Al III. Similarly, ion population is highest close to the target ($z = 0.5$ mm) and it decreases monotonically along the plume axis, whereas neutral population grows along the axis, and reaches a maximum at $z = 2$ mm. The fact that the decrease in ion density is associated with an increase in neutral density is a clear indication that strong ion-electron recombination is taking place during plume expansion.

The SLA plume shows a different dynamics because of the presence of fast and slow components. The fast component is clearly visible for neutrals, and is relatively weaker for ions. Even then, fast neutrals are only about one-third as intense compared to slow neutrals. It should be noted that the SLA fast components and ULA plume components appear almost at the same time after target irradiation. Similar to the case of ULA, here also the ion population is higher close to the target surface. However, while neutrals could be found up to a distance of 6 mm from the target surface, ions also could be seen up to a nearby distance of 5 mm (Figure 3.6(b)). This long persistence of the ions in SLA results from the fact that short pulses are relatively more efficient for the generation of higher charged states, which has implications in high harmonic generation (Gamaly 2011). Since coherent EUV and X-ray radiation can be generated using laser

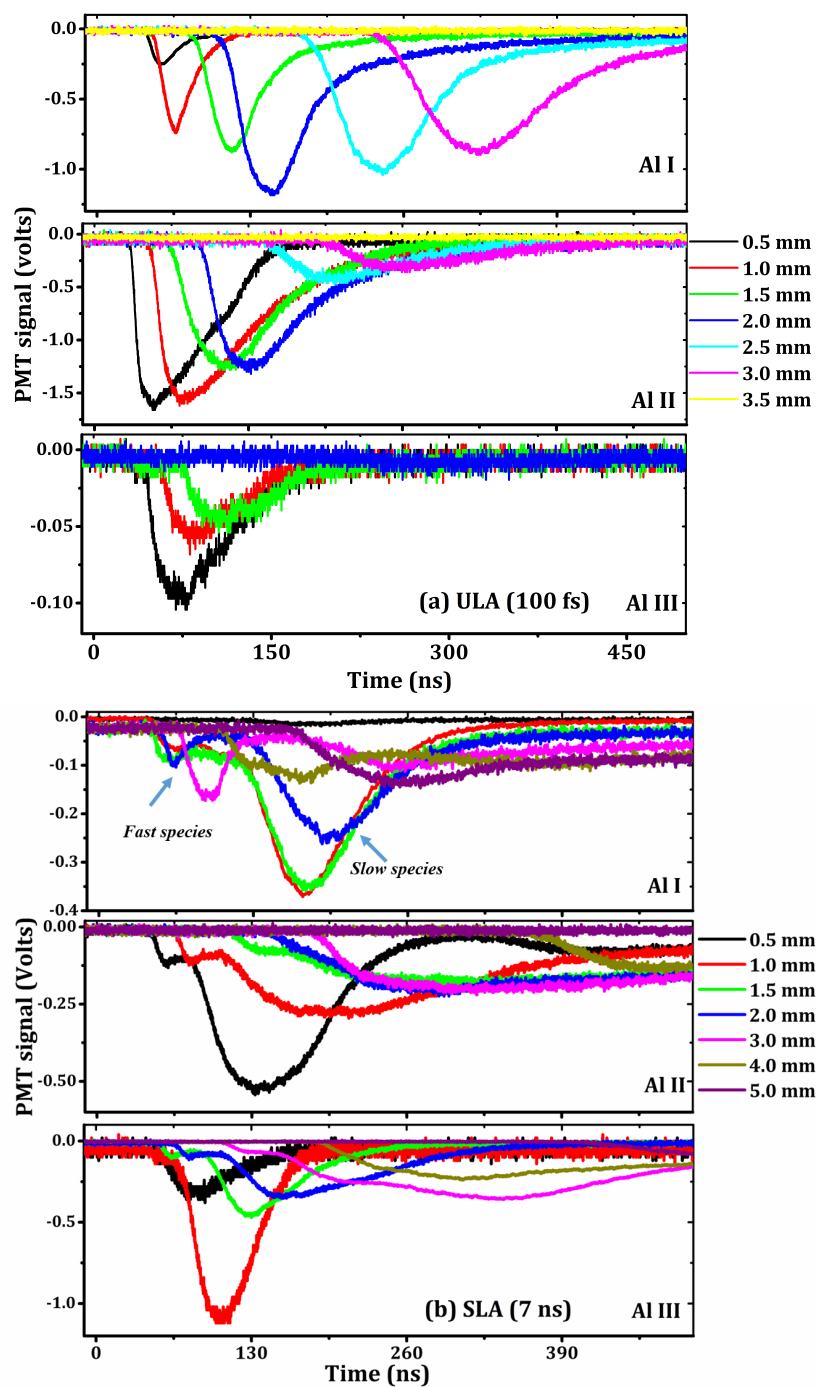


Figure 3.6: Time of flight spectra of Al I, Al II and Al III measured for different axial distances in the plume from the target surface, for (a) ultrashort and (b) short laser pulses. Zero time corresponds to the instant of target irradiation. Background gas pressure is 10 Torr.

produced plasmas as interaction media, production and characterization of plasmas is an essential first step for realizing the phenomena. For LPPs to be used as EUV and

X-ray sources, it is advantageous if highly ionized species are generated (Bagchi et al. 2011). Free electron will absorb laser light by specific collision-less processes like resonance absorption, and emits high energy radiation as they accelerate. High energy emissions are caused by accelerating free electrons, which absorb laser light by specific collision-less processes such as resonance absorption. As the evolution of hot electrons in the plasma eventually decides the ion emission characteristics, we can improve ion emission characteristics by controlling the plasma evolution.

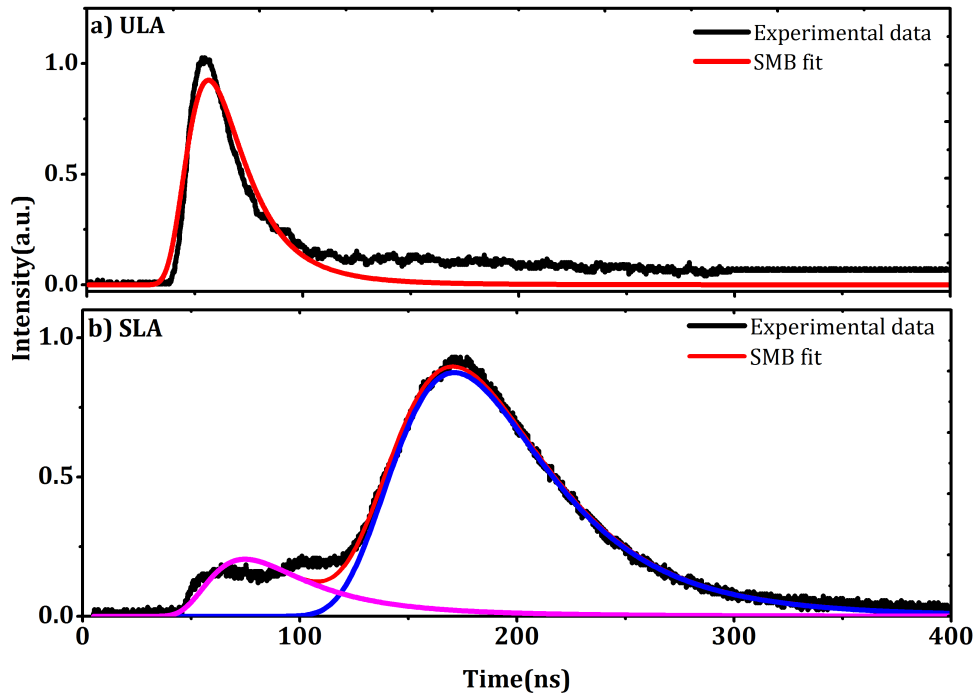


Figure 3.7: Intensity of emission with time for Al species measured at ~ 396 nm, at 1 mm distance from the target surface. The background nitrogen pressure was 10 Torr. Solid lines represent the Shifted Maxwell Boltzmann fit. In the case of SLA the fast peaks fits better to Gaussian function as shown in the inset.

In order to gain more insights into the kinetic properties of the plume species, shifted Maxwell-Boltzmann (SMB) distribution were fitted to the measured TOF profiles. The SMB fitting function is given by (Harilal et al. 2003)

$$f(v) = A \frac{m^{3/2}}{2\pi k} v^3 e^{-\frac{m(v-v_0)^2}{2kT}} dv \quad (3.7)$$

where A is a normalization constant, v and v_0 are the individual particle velocity and the center-of-mass velocity of the species, T is the translational temperature, k is the Boltzmann constant, and m is the mass of the species. The SMB distribution assumes that the speed distribution has equilibrated after propagating a short distance from the target surface and that the signal is a direct measure of the concentration of the indicated species. Figure 3.6 shows the TOF data fitted for ULA and SLA of Aluminium neutrals (396.1 nm) respectively. Excellent fit is observed for a center of mass velocity of 14.42 km/s and a translational temperature of 21.96 eV for ULA at a distance of 1 mm from the target. In the case of SLA the profile is fitted with two SMB distributions, of which one is for slow components and the other is for fast components. The fitting parameters are 5.0 km/s and 1.739 eV for the slow species, and 10.0 km/s and 21.81 eV for the fast species, respectively. However the fast peak does not fit properly to an SMB distribution: it fits best to a Gaussian distribution of the form

$$f(v) = Ae^{-\left(\frac{v-v_0}{\sqrt{2}\sigma}\right)^2} \quad (3.8)$$

This indicates that the fast peak is non thermal in nature, while the slow peak is a thermal component. Thus, the most likely explanation for the appearance of the fast peak is acceleration due to a space charge effect in the plasma (Elsied 2016).

Figure 3.8 shows velocities of species calculated from TOF data for a background pressure of 10 Torr. It can be seen that ULA components and fast SLA components are quicker to speed up and slow down, compared to the slow SLA components. Close to the target ($z = 0.5$ mm) Al III shows the highest velocity. Both Al III and neutrals attain maximum velocity (~ 15 kms $^{-1}$) at $z = 1$ mm in ULA. On the other hand, in SLA fast neutrals reach velocities up to ~ 30 kms $^{-1}$ at about $z = 3$ mm, while Al III and Al II reach velocities of ~ 20 kms $^{-1}$ and ~ 15 kms $^{-1}$ respectively, at 2 mm and 1.5 mm distances. The velocity of neutrals in ULA is only about half that of the fast neutrals in SLA. Fast neutrals have velocities comparable to or higher than fast ions, clearly indicating that they are formed by the recombination of the fastest ions in the plume. A similar acceleration of fast neutrals was observed in our recent studies of ultrafast

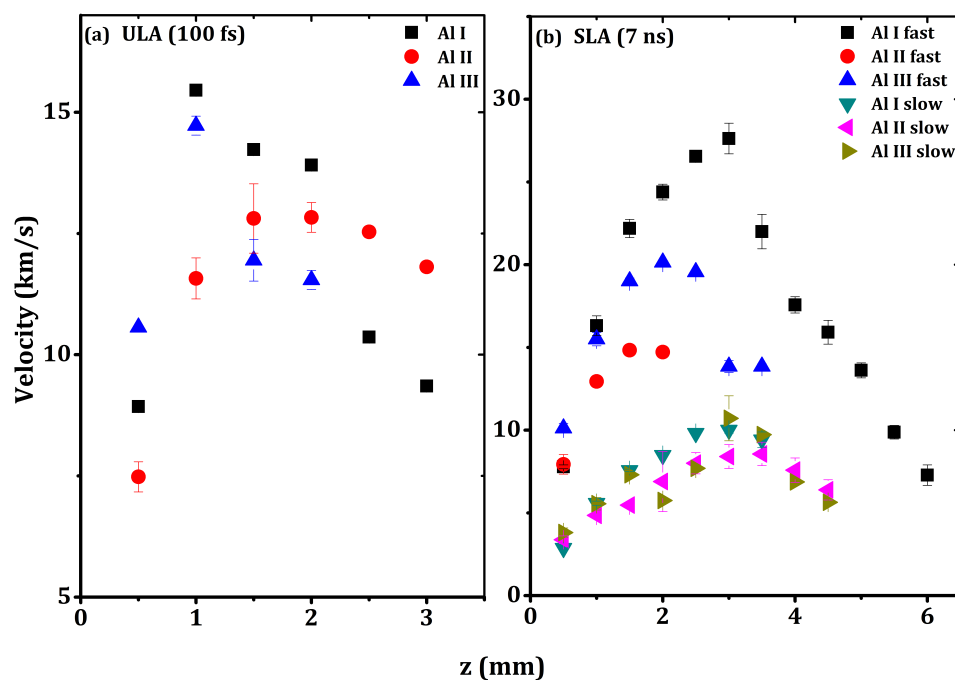


Figure 3.8: Velocities of atomic and ionic species in (a) ULA and (b) SLA, at different distances in the plasma plume from the target surface, estimated from the TOF data. The species attain relatively higher velocities in SLA compared to ULA. Background gas pressure is 10 Torr.

laser produced zinc and nickel plasmas as well (Smijesh and Philip 2013; Smijesh et al. 2014). Neutralization of fast ions occurs through collisional processes such as two body electron recombination or charge exchange (Kumar et al. 2008; Singh et al. 2008). Moreover, fast neutrals in SLA are the most persistent species as they can be seen up to a distance of 6 mm from the target surface.

The above TOF results can be explained by considering Coulomb explosion and thermal ablation as the predominant mechanisms responsible for plasma formation in ULA and SLA respectively, for metallic targets. In the case of ULA the entire laser pulse energy is transferred to the target in a very short timescale, before the formation of the plasma. The optical intensity is high at $7 \times 10^{14} \text{ W/cm}^2$ and the lattice will get disordered by direct excitation of the electronic system, while the lattice modes remain vibrationally cold (Siegal et al. 1994; Siegal et al. 1995). Plasma will be formed due to Coulomb explosion, resulting in an acceleration of charged species. Free electrons will

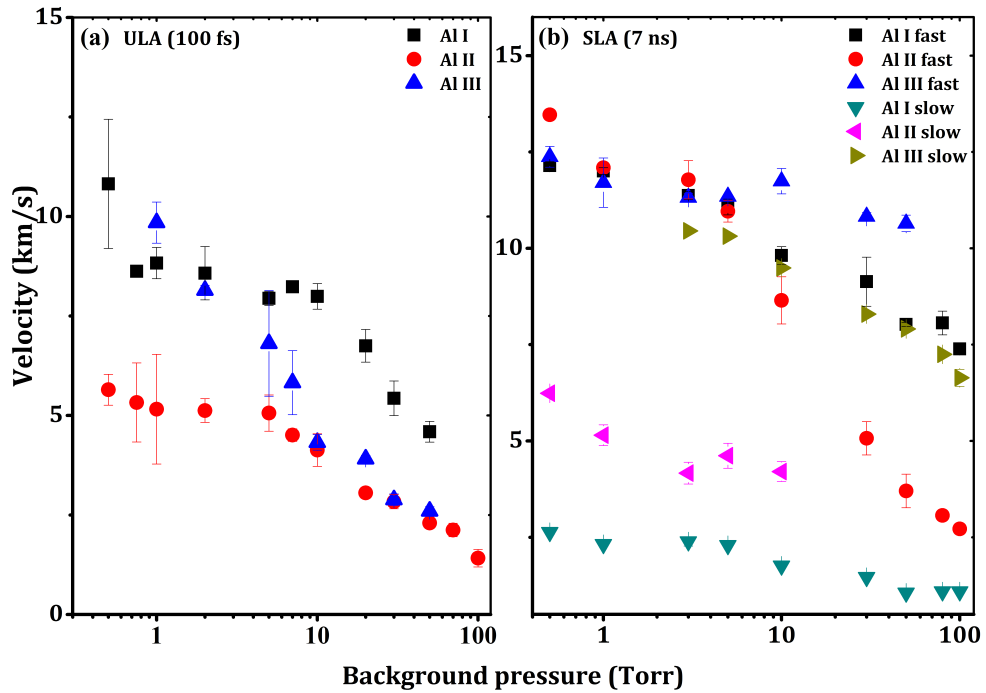


Figure 3.9: The peak velocity of Al, Al II and Al III in the plasma plume for (a) ultra-short and (b) short pulse laser ablation for different background pressures. The measurements are carried out at $z = 1$ mm.

travel faster than ions in the non-collisional regime, resulting in charge separation. This generates an electric field and therefore the space charge effect (Whealton and Whitson 1980; Rai et al. 2000). Ions of higher charge state will travel relatively faster compared to the other ions and neutrals. As the ions travel forward they will recombine with the electrons and form either neutrals, or ions of lower charge. This is evident from Figure 3.6a, where a decrease in the ion intensity along the plume axis is concomitant with an increase in the neutral intensity. The neutrals thus formed will initially have a velocity close to that of the fast ions. Since the ultrashort pulse is too short to interact with the generated plasma, further ionization due to laser-plasma interaction will be absent.

On the other hand, the laser intensity is orders of magnitude lower at 10^{10} W/cm² in SLA, reducing the chances of Coulomb explosion. Nevertheless, the weak Coulomb explosion will still generate a swarm of accelerating electrons which will exert their pull on the ions, some of which will recombine with the electrons at short distances from the

target surface. This will result in the formation of fast neutrals with velocities as high as those of the ions. However, most of the laser energy will be used for generating highly excited hot electrons, the energy of which will get transferred to the phonon modes in picosecond timescales (Singh et al. 2008), leading to thermal ablation. The plasma thus formed will be heated by the trailing part of the nanosecond laser pulse through inverse bremsstrahlung, resulting in further ionization. This results in a comparable population of ionic and neutral species.

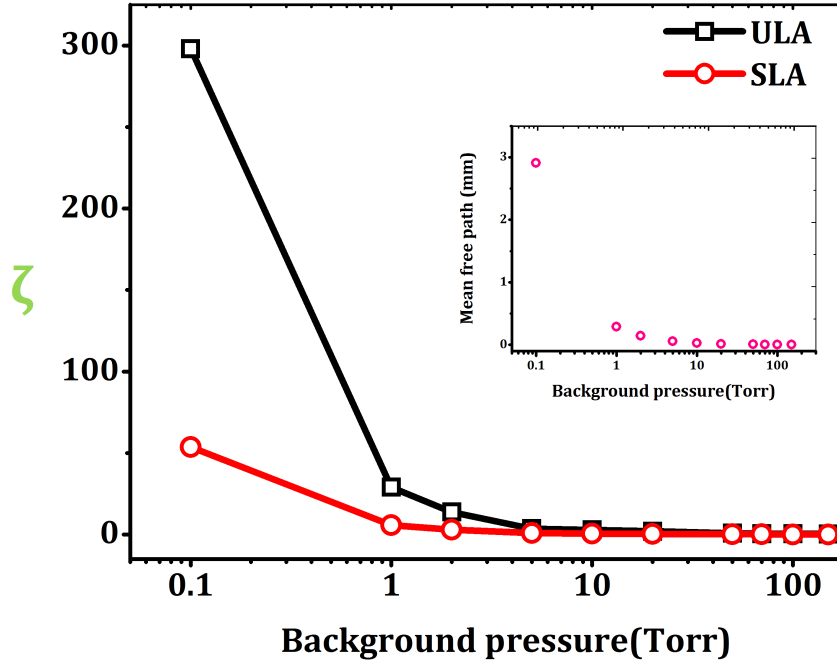


Figure 3.10: Collisionality parameter of the plasma plume at different background pressures. Measurements are carried out at $z = 1$ mm. Mean free path of the background gas is showed in the inset for different background pressures.

To get more insights into the effect of the ambient gas on the plasma, we calculate the collisionality parameter η (ratio of the mean free path (mfp) in nitrogen ambient to characteristic Debye length of aluminium plasma) as (Diwakar et al. 2015),

$$\zeta = \frac{mfp}{debye\ length} = \frac{RT}{\sqrt{2\pi}d^2N_A P} \frac{1}{\sqrt{\frac{\epsilon_0 k T_e}{n_e q_e^2}}} \quad (3.9)$$

where R is the gas constant, T is gas temperature, d is gas molecule diameter, N_A is Avogadro's number, P is gas pressure, ϵ_0 is the emissivity of free space, q_e is electron charge, and T_e and n_e are the plasma temperature and electron density respectively. Plume-ambient interaction becomes collisional when $\zeta > 1$ and free expansion when $\zeta < 1$. We estimated ζ using the measured T_e and n_e values. In vacuum, background gas pressure is so low that the mean free path of the ambient molecules is larger than the characteristic Debye length of the plume, and the plume expands adiabatically. At this stage almost all of the initial thermal energy deposited in the plasma will be converted into directed plume kinetic energy, giving high velocities to the plume species. At intermediate pressures, when the mean free path of the ambient molecules becomes comparable to the Debye length, collisions with background gas molecules begin to play a role. Here the collisions will mainly involve ablated species at the plume edge only, so that the overall plume propagation dynamics will be slightly affected. At higher pressures, when the plume becomes strongly confined and the ablated species tend to diffuse out of the plume core into the ambient gas, interaction between the plume and ambient gas will be stronger. Species velocities will get decreased in this case. Peak velocities of neutrals and ions estimated for background pressures in the range of 0.01 to 100 Torr is shown in Figure 3.9. In general, all velocities decrease when the pressure is increased, due to plume confinement.

3.3 Summary

Plasmas have been generated by irradiating a solid aluminium target by ultrashort (100 fs) and short (7 ns) laser pulses, and the dynamics of expansion of the resulting plasma plumes into the surrounding gas has been investigated for various ambient pressures. Maximum optical emission from the plasma is found to occur in the pressure range of 10 to 20 Torr, around a distance of 1 mm from the target surface. Emission intensity is one order higher for SLA because of laser-plasma interaction. While ions are relatively scarce in ULA, both neutrals and ions are equally abundant in SLA. Time of flight measurements show distinct fast and slow species of neutrals and ions in SLA, while the distinction is not obvious in ULA. Coulomb explosion is prominent in ULA because

of the high optical intensity of the laser pulse while thermal ablation and laser-plasma interaction are prevalent in SLA. The fast neutrals observed in SLA are formed by the recombination of fast ions with electrons. At low pressures, the plume expands freely but at higher pressures, the expanding plume decelerates soon due to plume confinement.

CHAPTER 4

ION DYNAMICS OF LASER PRODUCED ALUMINIUM PLASMA AT DIFFERENT AMBIENT PRESSURE

The spatial and temporal evolution of the whole plasma plume, as well as the ionic (Al^{2+}) component present in the plume, are investigated using spectrally resolved time-gated imaging. The influence of ambient gas pressure on the expansion dynamics of Al^{2+} is studied in particular. The shock wave and drag wave models are used to study the dynamics of the plume and the ionic components for different pressure.

“Creativity is contagious, pass it on.”

————— *Albert Einstein*

4.1 Introduction

On account of the numerous applications including laser treatment of surfaces, mass spectrometry, and nanotechnology, laser produced plasmas (LPP) have gained substantial attention in different areas of scientific and technological research (Eliezer and Mima 2009; Cremers and Radziemski 2006). For all these applications, ultrafast laser ablation (ULA) have several advantages over short pulse laser ablation (SLA). The ultrashort (fs) laser pulse duration is much shorter than the electron-to-ion energy transfer time, so due to which laser-plasma interaction does not occur (Gamaly 2011). Consequently, the entire laser pulse energy is transferred to the target material, which leads to more efficient ablation and lower fluence thresholds, when compared to short pulses. Future development of these and other applications requires a better understanding of the mechanisms of laser-solid interaction, formation of the plasma plume, and its expansion under vacuum or in ambient gas. Since the ambient gas effectively controls the plasma parameters, detailed knowledge of the dynamics of plasma expansion into the surroundings is indispensable from an application point of view.

The pulsed laser ablation technique can be used to generate ions with different charge states from a variety of target materials. Laser-ablated plasma can be considered as an instantaneous ion point source, with the characteristic ion emission time being smaller than the ion drift time, and the plasma plume dimension much smaller than the source-to-ion collector distance (Shaim et al. 2017). Ion generation at lower laser intensities (10^9 - 10^{15} W/cm²) is less studied and measured features of the generated ions lack a comprehensive interpretation. So far, only the cases of either vacuum or atmospheric pressure ambient have been considered in most reported studies of atomic and ionic plume expansion. Hence, a complete picture of the hydrodynamics of plasma propagation in different ambient gases and pressures is still elusive.

Ablation of a solid target by a short laser pulse can be broadly divided into three main stages: i) evaporation of the target material, ii) interaction between the evaporated material and the laser pulse resulting in material heating and plasma formation, and iii) plasma plume expansion and rapid cooling (Aguilera and Aragn, 1999). In the case of ultrashort laser ablation (ULA), the second stage is absent. This difference makes the comparison of ULA and SLA more noteworthy. The time-resolved evolution of the plume is driven by collisional processes between electrons, ions, and neutrals. In the case of SLA, electrons in the plume gain energy from the laser pulse mainly by inverse bremsstrahlung, and this energy is transferred to the ions and neutrals through collisional processes. The electron-ion energy transfer time is much shorter than the short laser pulse duration, resulting in the thermalization of the electrons and ions within the pulse (Shaim et al. 2017). Since the electrons are much lighter than the ions, some of the thermalized electrons electrostatic field (double-layer potential) at the expanding plasma-vacuum boundary (Bulgakova et al. 2000). However, the dynamics of the development and splitting of the plasma is still not fully understood and calls for further investigation. Moreover, the ion dynamics of an Al plasma has not yet been studied as a function of background pressure using fast photography.

4.2 Experimental setup

We have used an ultrashort and short laser pulse for creating a plasma of aluminium from high purity (99.99%) target obtained from ACI Alloys, Inc., San Jose, in the pressure range 10^{-5} to 760 Torr. The laser fluence is kept 50 J/cm^2 in both cases. Images of the expanding plumes are recorded for time delays up to 1000 ns using an Intensified Charge Coupled Device (ICCD, Andor istar CCD 334) fitted with an f/2.8 aperture lens (Nikon, Micro-NIKKOR-5 mm). We have used an optical interference filter (Andover corp. 50 mm in diameter) centered at 415 nm to obtain 2D images of LPP ion emission. The FWHM of the bandpass filters is $\approx 10 \text{ nm}$. From the spectrum, it is ensured that aluminium plasma has only ionic emission in this region. The 2-D images of the plume and ionic components have been used for further analysis. Detailed experimental setup is available in chapter 2.

4.3 Results and Discussion

In this work, we investigated the spatial and temporal evolution of the ionic component (Al^{2+}) of laser ablation plasma from an aluminium target. Ultrashort and short laser pulses used for ablation and the resulting plume is analyzed by the spectrally resolved time-gated imaging technique. 2D images of ion population are obtained by using appropriate bandpass interference filters in the imaging setup. It may be noticed here that while charge collection devices such as the Faraday cup and Langmuir probe can be employed for identifying ions in laser plasmas, these are effective only at very low ambient pressures. Moreover, these techniques lack species-sensitivity and cannot distinctly identify the charge state of the observed ions. Secondly, in most of the studies reported to date, characterization of the ion flux is carried out only along the normal to the target surface. In comparison, we investigate the spatially resolved, two-dimensional (2D) intensity maps of the plume emission and its ionic component. The expansion dynamics of the whole plume and the ionic component are discussed in terms of the shock wave and drag force models for increasing ambient pressures.

Among the various plasma diagnostic tools, Time-gated imaging using an ICCD is particularly effective and useful for the investigation of the hydrodynamics of laser ablation plasma. It provides two-dimensional snapshots of the plume propagation with detailed information about its structure and expansion dynamics. Time-resolved imaging of the plume provides corroborative information to TOF on the hydrodynamics of the plasma. As the ambient pressure is increased from 10^{-5} Torr to 760 Torr, the plasma evolution exhibited free expansion, splitting, sharpening, and some instability, due to the increasing plasmas ambient interactions(Diwakar et al. 2015).

In the case of ULA, when the pressure is increased to ~ 1 Torr, the spherical plasmas front turned into a cone-shape, called as plasmas sharpening. Harilal et al. (2002) have reported that the higher kinetic particles are emitted closer to the target surface normal (Harilal et al. 2002), while Pakhal et al. (2008) have mentioned that ions with higher ionization are dominant along the target surface normal, and their concentration reduces

away from the normal (Pakhal et al. 2008). With further increase in ambient pressure, instability at the plasmas-ambient interface also becomes significant. This instability becomes even higher at 760 Torr, and as a consequence, the plasma exhibited a rather irregular shape as shown in Figure 4.1. Furthermore, at atmospheric pressure levels, the pressure exerted by the ambient medium is significantly higher than the plume pressure. Hence, the effective length of the plume is confined to ~ 1 mm. In addition, the emission intensity decreases from vacuum to around 1 Torr then starts to increase.

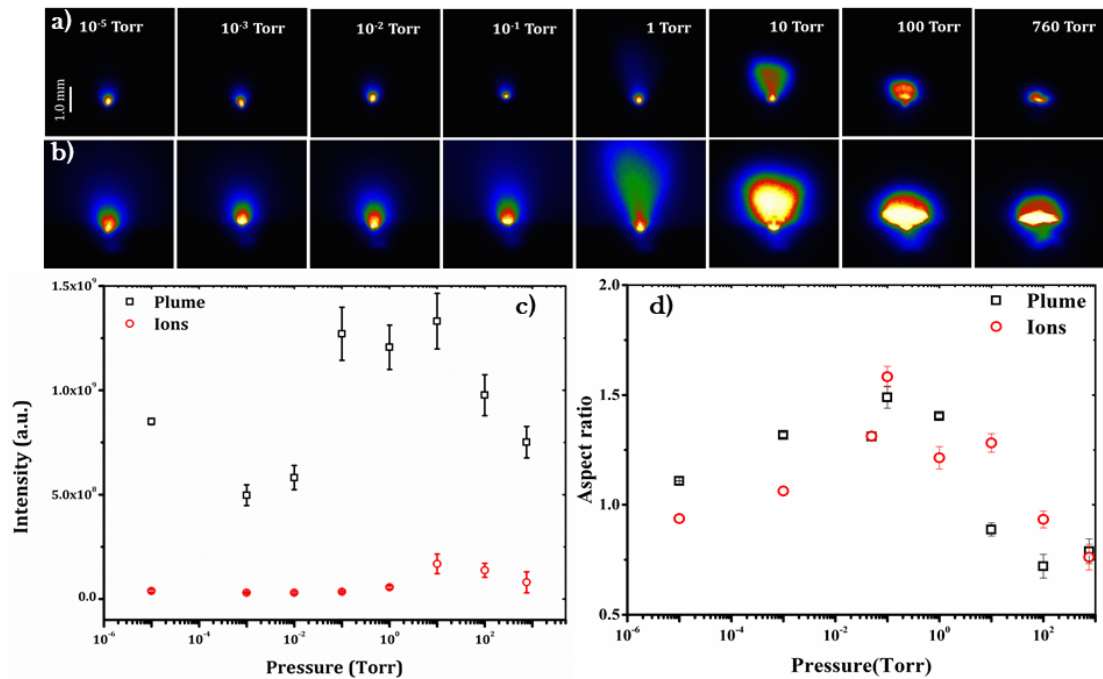


Figure 4.1: ICCD images of the a) ULA expanding plasma plume, and b) its ionic components (Al^{2+}), for varying ambient pressures ranging from 10^5 to 760 Torr. Gate delay of the ICCD is 50 ns, and the gate width is 1000 ns. c) Variation of intensity with ambient pressure for the whole plume and its ionic component. Maximum intensity is observed for the pressure region of 1 Torr to 10 Torr. d) The aspect ratio of the plume (plume length/plume width) measured at various pressures, for 1000 ns ICCD gate width.

However in the case of SLA, when the ambient pressure is increased from vacuum to around 10^{-2} Torr, the emission intensity decreases. Above these pressure levels, the plume emission is significantly enhanced. The plume starts to change because of the increase in plume ambient species collisions. The plume initiates with a forward bias in the beginning, and later on, tends to attain spherical shape because of collision of the

plume front with the ambient air. If the ambient pressure is further increased the plasma is confined to a smaller region close to the target surface, and the integrated emission volume becomes smaller (Yaln et al. 2004) due to which the integrated intensity also decreases in both ULA and SLA cases, as shown in Figure's 4.1 and 4.2.

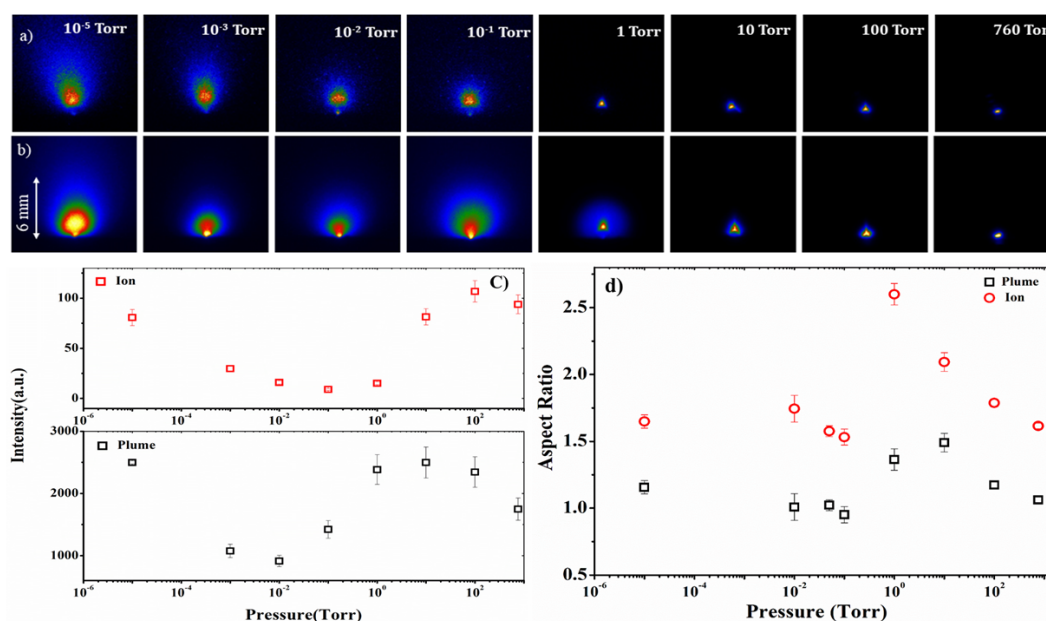


Figure 4.2: ICCD images of the a) SLA expanding plasma plume, and b) its ionic components (obtained using an interference filter), for varying ambient pressures ranging from 10^{-5} to 760 Torr. Gate delay of the ICCD is 50 ns, and the gate width is 1000 ns. c) Variation of intensity with ambient pressure for the whole plume and its ionic component. Maximum intensity is observed for the pressure region of 0.1 Torr to 10 Torr. d) The aspect ratio of the plume (plume length/plume width) measured at various pressures, for 1000 ns ICCD gate width.

Figures 4.3 - 4.6 depicts the 2-D images of ULA and SLA plasma plume and the ionic components in the plumes recorded for a range of atmospheric pressures (10^{-5} - 760 Torr). The ICCD images recorded with 1000 ns gate width at a delay of 50 ns from the laser pulse. The images (normalized to the maximum intensity in each row) show the spectrally integrated (350 - 900 nm) emission of the plasma excited species. The ambient gas pressure strongly influences the hydrodynamic expansion of the plasma. For pressure values ranging from 10^{-5} Torr - 10^{-1} Torr, the plasma has nearly the same spatial profile in both cases. The plume expands in the forward direction under the influence of pressure gradient. In vacuum, the plume expands adiabatically and has an ellipsoidal shape for ULA and SLA plumes. It shows a non-uniform intensity pattern

parallel to the direction of plume expansion and is more intense at points closer to the target. On increasing the ambient pressure, the plume becomes narrower in SLA but sharper for ULA. At even higher ambient pressures, the higher intensity region moves further towards the target (Harilal et al. 2014). Thus, the shape, size, and intensity of the plume are highly dependent on the nature of the ambient gas. The ionic components also exhibit the same behaviour as the plume. At vacuum (10^{-5} - 10^{-1} Torr) collisions are negligible between the expanding plasma species and the ambient medium. For higher pressures range, 1-10 Torr collisional excitation is enhanced, so the plasma emits more light. However, if the ambient pressure is increased beyond 10 Torr, the plasma is confined to a smaller region close to the target surface, and the integrated emission volume becomes smaller. Moreover, since the ambient gas cools the expanding plasma quickly by collisions, in this case, emission from the confined plasma will have a lower intensity (George et al. 2009;Sankar et al. 2018).

Similarly seen some common observations in the case of ions as follows, at low pressures collisions are minimal, and the plume expands more, reducing the number density and hence the ionization rate. In both ULA and SLA, the intensity of ions decreases from vacuum to around 1 Torr as similar to the plume. As the pressure increases the collision rate increases, leading to enhanced ionization of the ablated species. It is because of enhanced ionization, in turn provides the necessary free electrons to promote the excitation phenomenon further (Diwakar et al. 2015;Smijesh and Philip 2013). Thus, the intensity of ion emission also increases with pressure. If the pressure is increased beyond certain limits, the ions will undergo collisional recombination leading to a decrease in the intensity of ions. The ionic species also follows the sharpening effect after 1 Torr ambient pressures in case of ULA. The sharpening effect is more and more pronounced as the ambient pressure increases.

In ULA, ablation typically starts in the 1 - 10 ps time and is shortly followed by optical emission created from the plasma. Therefore, the emission and formation of plasma will happen in very fast time scales. The ULA plasma is transient in nature but, the self-emission in plasma can last up to a few hundreds of nanoseconds (Gamaly,

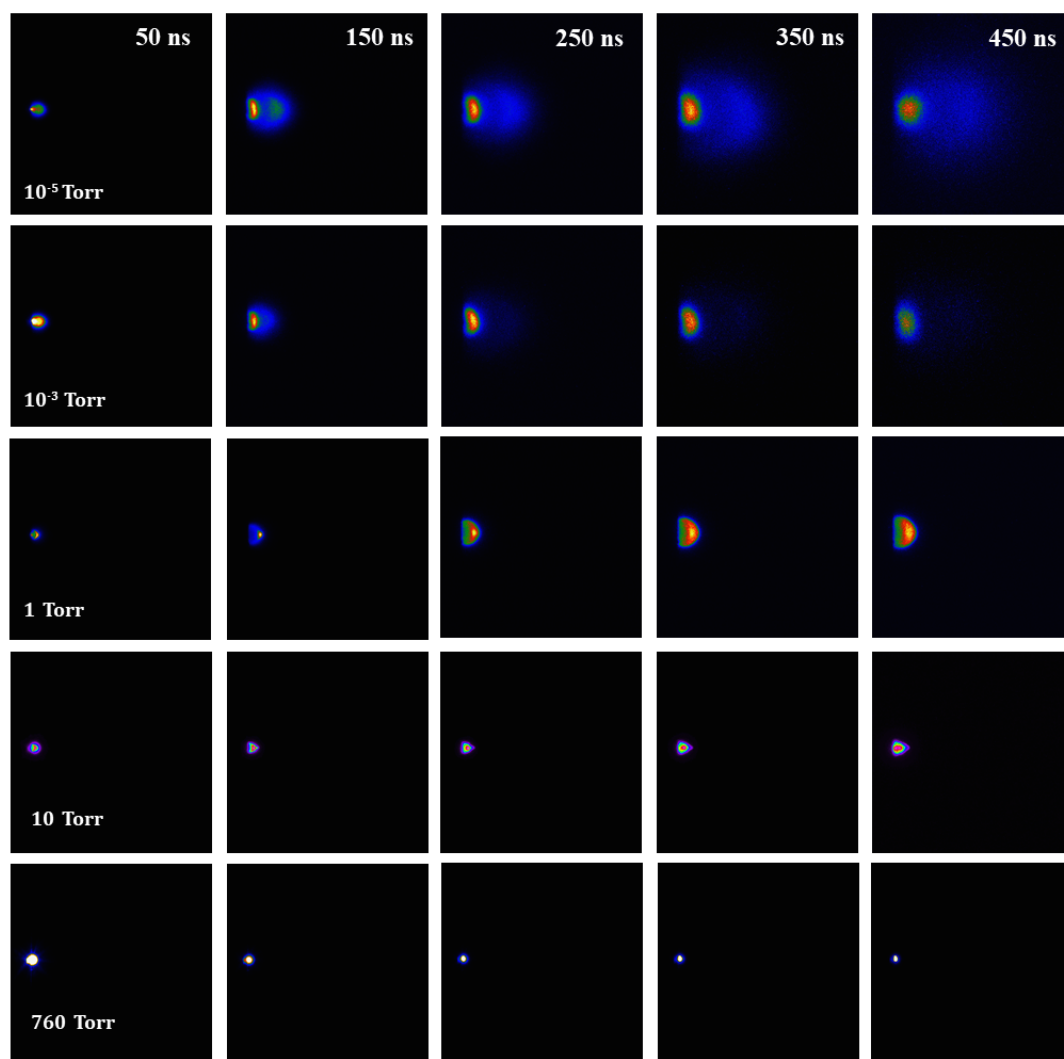


Figure 4.3: Temporal evolution of ultrashort laser produced plasma (ULA) plume from the aluminium target for five different ambient pressures. Images are normalized to their maximum intensity along each row.

2011;Chichkov et al. 1996;Rethfeld et al. 2004). ULA plumes are found to expand with a much stronger forward bias in directions normal to the target surface. Forward-directed expansion of this laser plumes can be understood by considering pressure confinement due to strong overheating in the laser impact zone and narrower angular distribution. However, the plume sharpening behaviour suggests that higher kinetic energy particles are emitted closer to the target surface normal. By increasing the background pressure, the expansion dynamics of the plume is strongly affected by the interaction with the background gas. As shown in Figure 4.3, the plume propagation is progressively slowed down and spatial confinement of the species with the formation of a con-

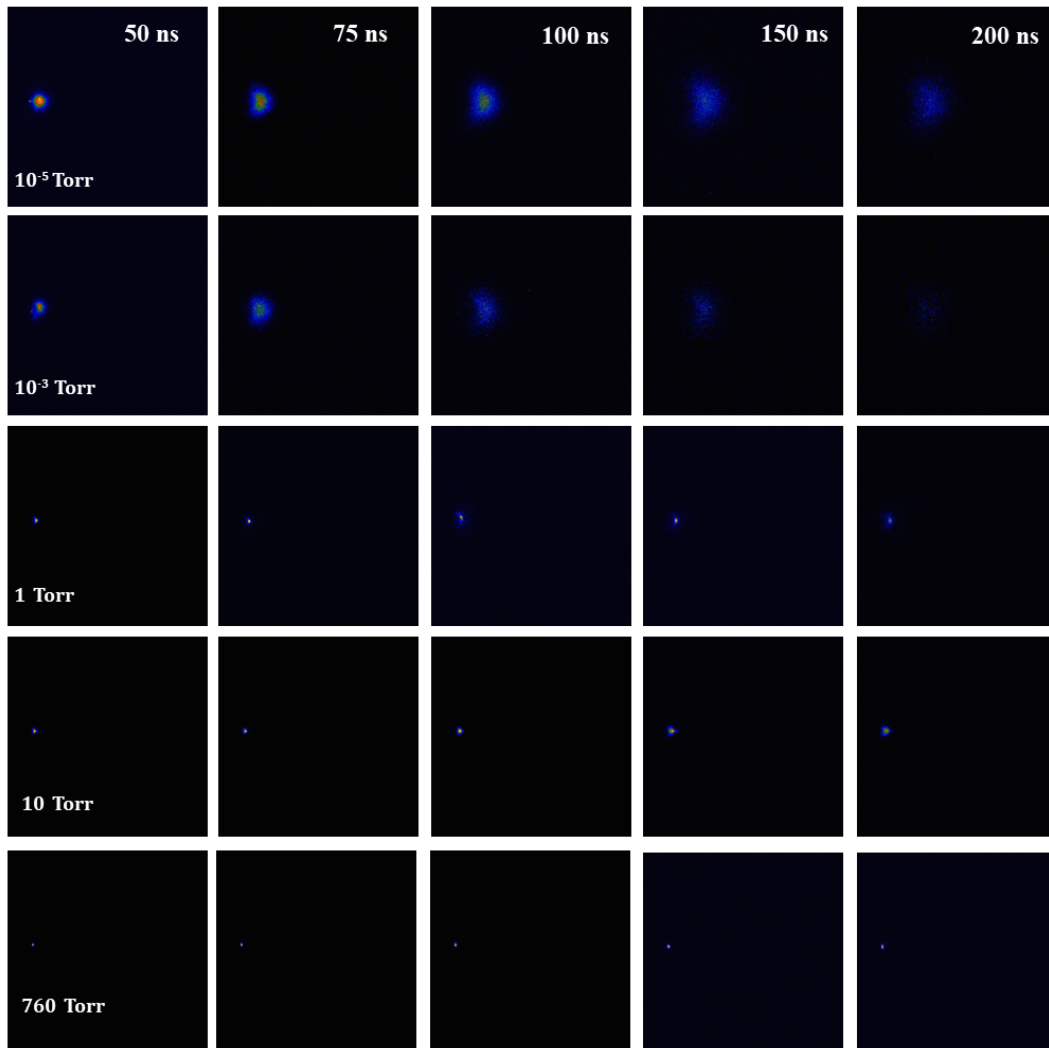


Figure 4.4: Temporal evolution of the ionic components (Al^{2+}) in the ultrashort laser produced plasma (ULA) plume from an aluminium target for five different background pressures. Images are normalized to their maximum intensity along each row.

tact front, and a consequent increase of the emission at the front. At longer time delays, plume stopping and transition to a diffusive-like propagation regime are also observed at high and low pressures respectively. In vacuum, the ULA produced Al^{2+} species is transient compared to ULA plasma. It will die out very fast even at 200 ns, which is because of faster recombination in ULA.

Considering SLA, in vacuum pressure within the plasma is higher than the ambient gas pressure so that a supersonic free expansion of the plume occurs. The plume propagates freely in a forward direction, with species of higher kinetic energy and higher

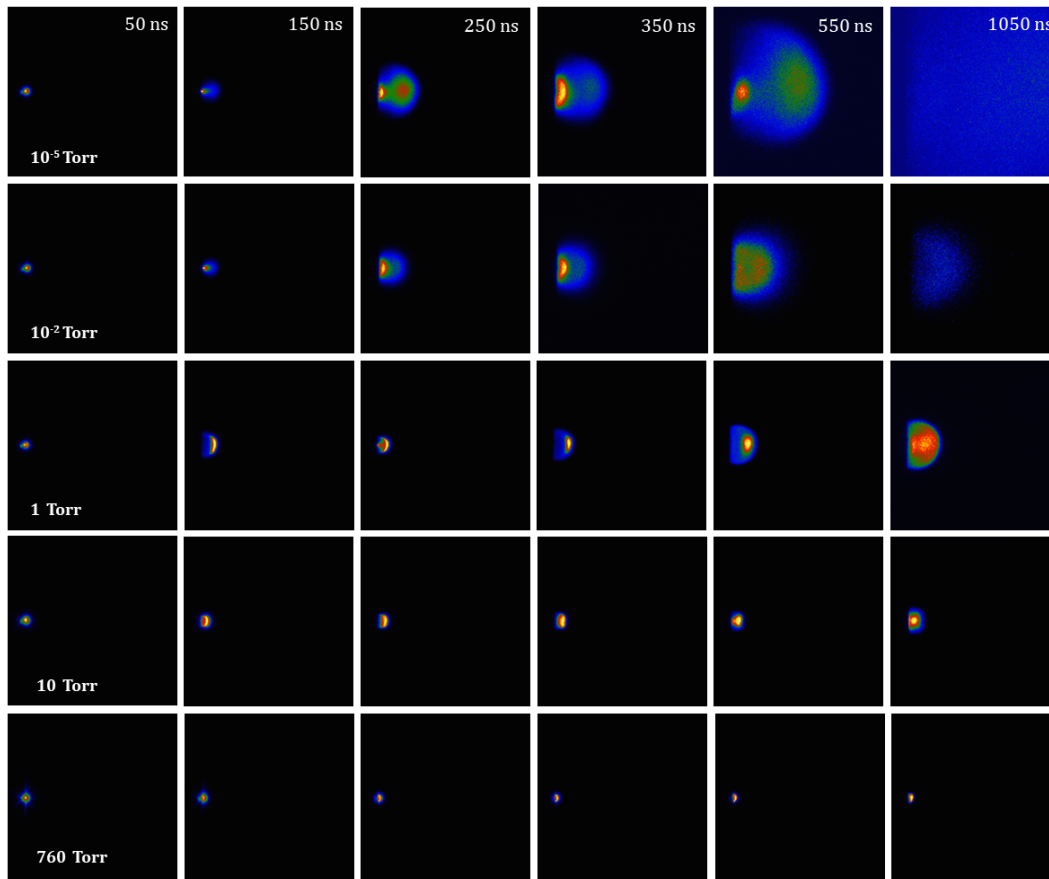


Figure 4.5: Temporal evolution of short laser produced plasma (SLA) plume from the aluminium target for five different ambient pressures. Images are normalized to their maximum intensity along each row.

charge states moving faster in the direction normal to the target. Their density is relatively low away from the target normal, and the nearly sphere-shaped plume diffuses into the surroundings. As the pressure increases (10^{-3} Torr, 1 Torr) the plume is more confined and assumes a hemispherical shape, particularly after 350 ns. It may be noted that while at low pressures both the plume and its ionic components are weakly compressed, and the process is mainly diffusive in nature, at higher pressures the interaction is dominated by the plume-gas pressure interplay. As pressure increases, the ambient gas begins to limit the expansion of the plume, while the ionic components in the plume front, acting as a piston, snowploughs the background gas. In this hydrodynamic regime, the plume expansion is concurrent with the generation of a shock wave. The plume front gets strongly compressed and its center exhibits oscillations, leading

to the formation of a compressed gas layer in front of the plume (Pain 1963;Fabbro et al. 1990). The plume and gas density profiles obtained at various pressures will indicate the background pressure needed for the beginning of the snowplough effect (Itina et al. 2002). At the highest pressures (760 Torr) the plume is very confined and the emission intensity is less, because enhanced collisions with the background gas result in a higher rate of ion-electron recombination. Plume intensity is highest for the intermediate pressures where the processes of plume confinement, collisional ionization and recombination are optimally balanced. The intensity of the ionic components in the plume also varies in a similar fashion (Figure 4.6).

Position-time plots of the leading edge of the ultrashort laser produced plasma (ULA) emission were extracted from the ICCD images, as shown in Figure 4.7. The plume exhibits fast expansion in the initial timescales, and then it becomes slow. At vacuum, both plume and ionic components follow free expansion indicated by linear fits. The estimated velocities are 34 km/s and 45 km/s for plume and ionic components respectively. The absence of deceleration indicates free expansion of the plume. When the background pressure is increased, the plume velocity is reduced. Depending on the pressure range, the plasma expansion dynamics can be analyzed in terms of different models, of which the two major ones are the shock wave and the drag force models (Dyer et al. 1990;Kumuduni et al. 1993;Kielkopf 1995).

At moderate pressures (1 Torr - 100 Torr) the experimental data is found to fit well with the shock wave model. According to the shock wave model, the expansion length of the plume controlled by the background pressure. This model justifies only after the mass of the gas surrounding the shock wave is higher than the mass of the ablated material. Under the shock wave model, the distance R from the target surface at which maximum transient emission is observed is given as a function of time as (Kumuduni et al. 1993),

$$R = \frac{k^{\frac{1}{5}}}{p} t^{\frac{2}{5}} \quad (4.1)$$

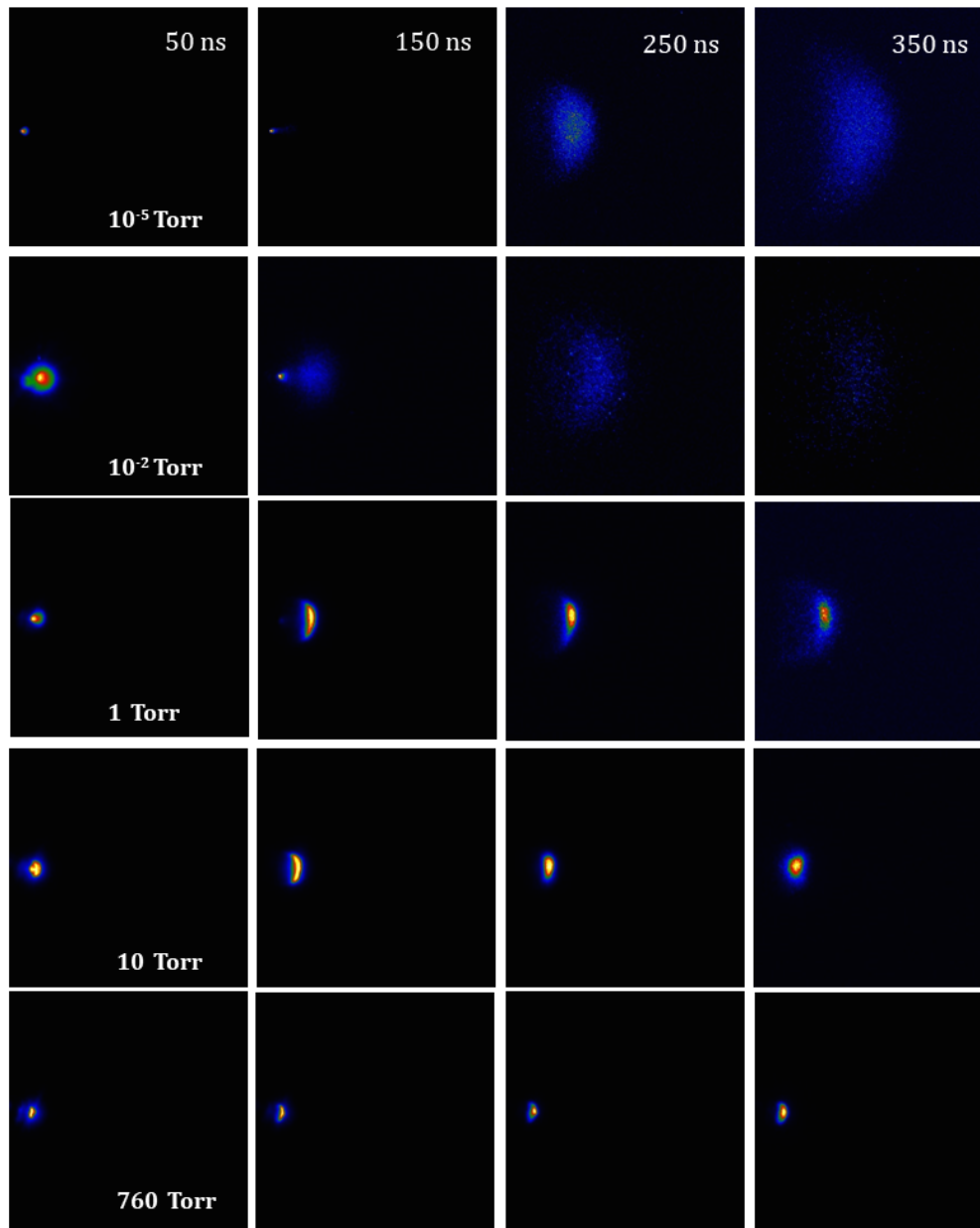


Figure 4.6: Temporal evolution of the ionic components (Al^{2+}) in the short laser produced plasma (SLA) plume from an aluminium target for five different background pressures. Images are normalized to their maximum intensity along each row.

where k is a constant proportional to the laser energy density, and p is the ambient gas pressure. The Plume and ions have a similar trend at moderate pressure. It indicates that the plume and ions are mostly in the same shock wave regime shown in Figure 4.8.

The increase in background pressure affects the expansion of plasma. When the

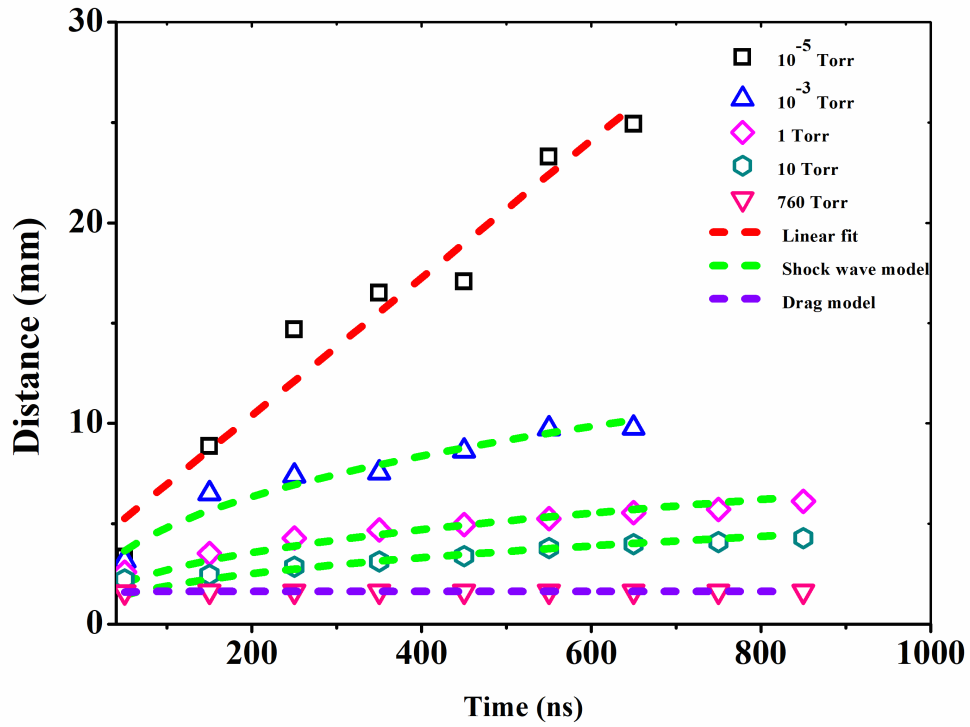


Figure 4.7: Position-time plots for the whole ultrashort laser produced plume (ULA) estimated from the gated ICCD images, for the ambient pressure range of 10^{-5} Torr to 760 Torr. Symbols denote measured data points, and dashed curves represent different expansion models. For the shock wave model, $kt = (k/p)^{1/5}$ found to be $0.257 \text{ mm/ns}^{0.4}$ for 10^{-3} Torr, $kt = 0.014 \text{ mm/ns}^{0.4}$, for 1 Torr, $kt = 0.002 \text{ mm/ns}^{0.4}$ for 10 Torr. Fitting parameters for the drag model at 760 Torr are $\beta = 0.078 \text{ ns}^{-1}$ and $R_0 = 1.629 \text{ mm}$, respectively.

plasma moves at speed close to the speed of sound, the plume experience an opposing drag force that makes it stop after traveling a certain distance known as stopping distance. Considering that the ambient air strongly influences the plasmas dynamics, the plasma front could be interpreted with the classic drag force model. In this model, the ejected ablation products experience a viscous force proportional to its velocity through the background. So, at higher pressures, the plume expansion is better described by the drag model, which is given by (Kumuduni et al., 1993)

$$R = R_0(1 - \exp(-\beta t)) \quad (4.2)$$

where R_0 is the stopping distance of the plume and β is the slowing coefficient ($R_0\beta =$

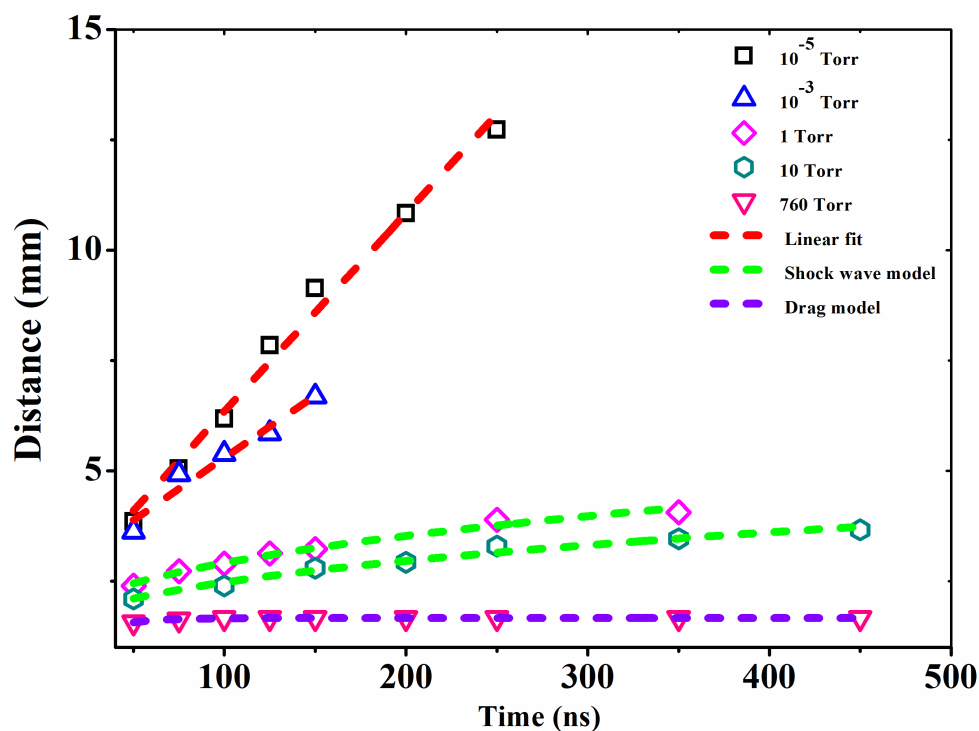


Figure 4.8: Position-time plots for the ultrashort laser produced ions (ULA ions) estimated from the gated ICCD images, for the ambient pressure range of 10^{-5} Torr to 760 Torr. Symbols denote measured data points, and dashed curves represent different expansion models. For the shock wave model, $kt = (k/p)^{1/5}$ found to be $0.01526 \text{ mm/ns}^{0.4}$ for 1 Torr, $kt = 0.008 \text{ mm/ns}^{0.4}$, for 10 Torr. Fitting parameters for the drag model at 760 Torr are $\beta = 0.056 \text{ ns}^{-1}$ and $R_0 = 1.662 \text{ mm}$, respectively.

v_0). Both plume and ions follow the drag model at extremely higher pressure.

The position-time plot for the leading edge of the short laser produced plume (SLA) calculated from the ICCD images is shown in Fig 4.9. While the leading edge of the plasma plume has a constant velocity of 27 km/s in a vacuum (10^{-5} Torr), the constant velocity is reduced to almost half (14 km/s) at 10^{-3} Torr. The absence of deceleration indicates free expansion of the plume. When the background pressure is increased, the plume velocity gets reduced.

At moderate pressure regime, the delayed Shockwave model fit well with the data. Under this model, the distance R from the target surface at which maximum transient

emission is observed is given as a function of time by (Kielkopf, 1995),

$$R = \frac{k^{\frac{1}{5}}}{p} t^{\frac{2}{5}} - R_0 \quad (4.3)$$

where k is a constant proportional to the laser energy density, and p is the ambient gas pressure. R_0 is the boundary condition in the fact that it is necessary to wait a certain time before the emission occurs ($R=0$).

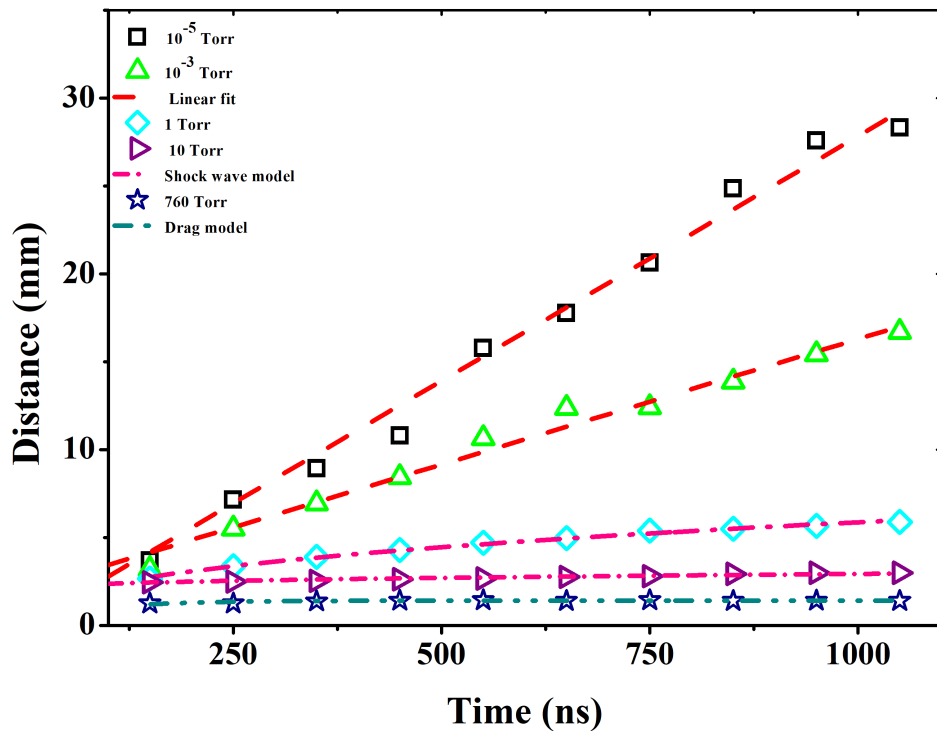


Figure 4.9: Position-time plots for the whole short laser produced plume (SLA) estimated from the gated ICCD images, for the ambient pressure range of 10^{-5} Torr to 760 Torr. Symbols denote measured data points, and dashed curves represent different expansion models. For the shock wave model, $kt = (k/p)^{1/5}$ and R_0 found to be 6.92×10^{-4} mm/ns $^{0.4}$ and 0.0054 mm respectively for 1 Torr, $kt = 6.75 \times 10^{-7}$ mm/ns $^{0.4}$ and 2.0 mm respectively for 10 Torr. Fitting parameters for the drag model at 760 Torr are $\beta = 0.0125$ ns $^{-1}$ and $R_0 = 1.4$ mm, respectively.

All the plasmas go through the process of rapid expansion at the initial timescales, followed by deceleration before finally coming to rest. The ambient gas pressures in-

fluence the plasmas dynamics and the stopping distance significantly. At higher background pressure, the expansion of plasma more gets affected. Therefore, the drag model mentioned above better describes the plume expansion at higher pressures.

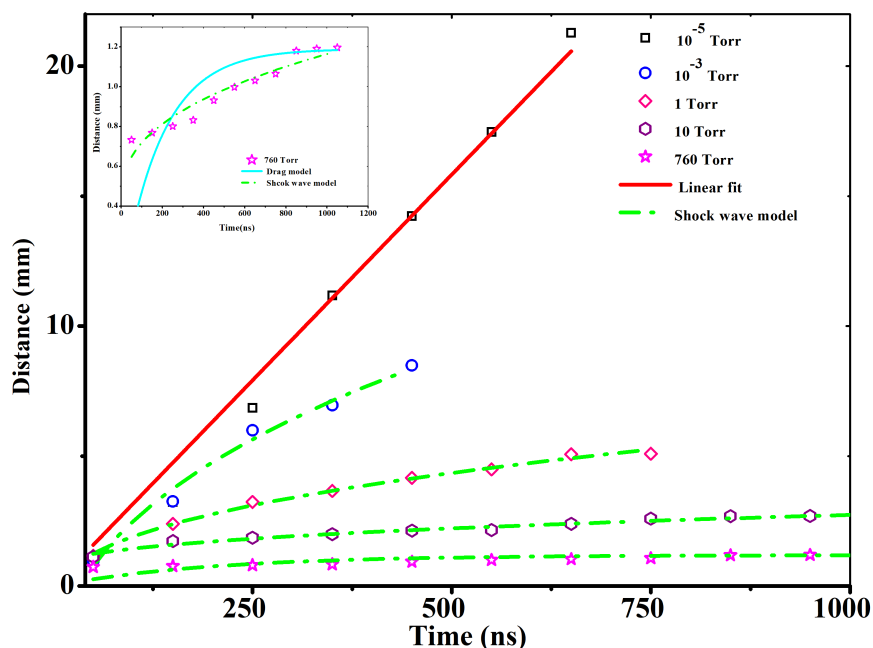


Figure 4.10: Position-time plots for Al^{2+} estimated from the ICCD images of SLA ions, for the ambient pressure range of 10^{-5} Torr to 760 Torr. Symbols denote measured data points, and the dashed curves represent shock wave expansion model. The inset shows the shockwave and drag model fits for the 760 Torr background pressure. For the shock wave model, $kt = (k/p)^{1/5}$ and R_0 found to be $1.832 \text{ mm/ns}^{0.4}$ and 4.63 mm respectively for 10^{-2} Torr, $kt = 0.0144 \text{ mm/ns}^{0.4}$ and 0.79 mm respectively for 1 Torr, $kt = 4.66 \times 10^{-5} \text{ mm/ns}^{0.4}$ and 0.58 mm respectively for 10 Torr, and $kt = 2.233 \times 10^{-7} \text{ mm/ns}^{0.4}$ and 0.12 mm respectively for 760 Torr.

In the case of the ionic components (Al^{2+}) present in the plume, the dynamics are found to be different. The ions located at the frontal region of the plasma acquire high energies during hydrodynamic acceleration. These ions propagate with high kinetic energies close to the free expansion velocity of 32 km/s. This small group of high energy ions transports a significant fraction of the absorbed energy, and they expand into the ambient gas quickly (in comparison, the ions located in the inner plume layers are accelerated much less during hydrodynamic expansion). Ions moving faster than the speed of sound generate transient pressure gradients in the medium, resulting in the generation of shock waves. Since the delayed shock wave fit we obtained for ion

expansion is good up to 760 Torr, it is obvious that the ion dynamics does not enter the drag regime within the entire pressure range studied. Rather, the ambient gas effect is limited to slowing down the expansion at higher pressures by virtue of enhanced collisions with the gas species. When ambient pressure increased, plume-background interaction leads to the so-called snowplough effect. The ablated material pushes the ambient gas away from the target as long as the pressure in the plume overcomes that of the ambient gas. Therefore, as the pressure is increased, the ions travelling in the plume front push the ambient gas away from the target until the pressure in the plume become similar to that of the ambient gas. Because of that, these ionic components also are compressed. This may be due to snowplough effect. This deceleration will in turn bring down the ion kinetic energy closer to that of the whole plume.

Thus, from the discussion and experimental findings, plume expansion as a function of ambient gas can be categorized into three different regimes, viz. vacuum, intermediate, and high pressures. Each of these regimes is characterized by a different plume dynamics. In vacuum a linear dependence of the plume front evolution with time is observed. The validity of the shock wave and drag models in atomic plume has been investigated in intermediate and higher pressure regime.

4.4 Summary

In summary, an expanding plasma plume has been produced by the ablation of an Aluminium target using 800 nm, 100 fs (ULA) and 1064 nm, 7ns (SLA) laser pulses. A comparison study of ultrashort and short laser produced plasma on the dynamics of the species in the plume at different background pressures is provided. From time integrated and time-resolved ICCD imaging of plasma, the spatial and temporal evolutions of the whole plasma plume, as well as that of its ionic component, have been investigated. The intensity of emission and aspect ratios of the whole plume and ions (Al^{2+}) have been measured which are found to be maximum at intermediate pressures in both ULA and SLA. In case of ULA, the plume has an average velocity of 34 km/s at vacuum. The ions in the plume front expand very fast with a velocity of 45 km/s; however, as

the pressure increases, there is a decrease in speed due to energy exchange between the ions and the ambient gas. However, in SLA the plume and the ions expand adiabatically with velocities of 27 km/s and 32 km/s respectively.

The deceleration of the ejected species with increasing ambient pressure is analyzed within the framework of the shock wave and drag force models. The expansion fits a shock wave model for higher ambient pressures up to 10 Torr. When pressure increases to 760 Torr, the velocity reduces drastically and sufficiently to be fitted by the drag model for ULA. Nevertheless, in SLA the expansion of the whole plume is found to fit a delayed shock wave model up to the ambient pressure of 10 Torr and plume slows down sufficiently to fit a drag force model at the highest pressure (760 Torr). However, the ionic component that moves in the plume front behaves differently and contributes most to the snowplough effect, which in turn leads to a shock wave behaviour up to the highest ambient pressure studied. As these results provide a better understanding of the effects of ambient gas pressure on the dynamics of the whole plume and its ionic component for a laser produced aluminium plasma, they are potentially useful from the perspective of a multitude of laser plasma applications.

CHAPTER 5

EFFECT OF LASER BEAM SIZE ON THE DYNAMICS OF ULTRASHORT LASER PRODUCED ALUMINIUM PLASMA IN VACUUM

In this work, the expansion dynamics of an ultrashort laser-produced aluminium plasma is investigated as a function of the laser beam size on the target, using a combination of diagnostic tools; viz. optical emission spectroscopy, fast gated time-resolved imaging, and ion current measurements. In laser-produced plasma experiments, the diameter of the irradiating laser beam on the target surface is a major parameter that influences the ablation mechanisms, plasma emission intensity, charged particle ejection, and plume morphology. These studies are of potential importance for variety of applications, including ion beam generation, pulsed laser deposition, laser welding and micromachining.

“The important thing is not to stop questioning.

Curiosity has its own reason for existing.”

————— *Albert Einstein*

5.1 Introduction

The expansion dynamics of ultrashort pulse laser ablation (ULA) plasma plumes is under extensive investigation owing to a wide variety of applications (Phipps 2007; Gamaly 2011; Eason and Wiley 2007). Compared to short pulse laser ablation (SLA) using nanosecond pulses, ULA offers some unique features for analytical applications such as negligible heat-affected zones, reduced matrix effects, lower continuum emission, higher yields for nanoparticle generation, and better uniformity of particle size distribution (Gamaly 2011; Gurevich and Hergenroder 2007; Russo et al. 2013). A two-temperature heat conduction model is often used to model energy transfer to the lattice immediately following laser irradiation, considering hot electrons and room-temperature ions located within the absorption depth on the target surface (Nolte et al. 1997). Since ultrafast laser-induced phase transformations occur under non-equilibrium conditions, significant efforts have been devoted for modeling the ULA process. According to Stoian et al. (2000), two competing mechanisms are responsible for ablation and material removal during the interaction of an ultrashort pulse with a target. One is Coulomb explosion, where highly-charged ions are pulled out from the lattice surface by the ejected high-energy electrons. The other is thermal vaporization, which occurs within tens of picoseconds to nanoseconds after laser irradiation, as electron-phonon interactions transfer the absorbed energy into the lattice (Gamaly 2011; von der Linde et al. 1997; Stoian et al. 2000). Previous studies show that thermal vaporization provides an order of magnitude higher ablation rate compared to Coulomb explosion (Stoian et al. 2000; Stoian et al. 2002). Coulomb explosion generally dominates at low laser intensities near the ablation threshold, in the regime of gentle ablation (Gamaly 2011; Stoian et al. 2000; Stoian et al. 2002).

One of the important parameters that controls the hydrodynamic expansion of a laser-produced plasma is the laser fluence. The fluence of the incident pulse governs various physical mechanisms taking place during the ablation process. Fluence can be varied by changing either the laser pulse energy or the beam area on the target. Most of the previous reports have explored fluence-dependent dynamics of ULA by varying the laser pulse energy falling on the target (Anoop 2015a;Anoop et al. 2016). For instance, Anoop et al. (2016) has studied ion dynamics of a ULA copper plasma for different fluences by changing the energy of the laser pulse (Anoop et al. 2016). However, a few other studies also have been reported, which investigate plume dynamics with varying beam sizes (Harilal et al. 2015;Harilal 2007). A recent study by Harilal et al. (2015) has shown that plume morphology changes significantly with beam size on the target (Harilal et al., 2015). While Photothermal ablation mechanisms like material evaporation and sublimation are important for larger beam sizes (Abdellatif and Imam 2002;Ciocan, et al. 1998), non-thermal and thermal mechanisms are equally important for smaller beam sizes (Bulgakova and Bulgakov 2001).

In this work we generate an ultrashort laser-produced plasma on an Al target using 100 fs laser pulses, and investigate its features as a function of the irradiation beam size. Optical emission spectroscopy (OES) is used for identifying excited atoms and ions present in the plasma. Morphology of the plume and its expansion into the surrounding space are studied from time-resolved ICCD images. The flux of the ions, their spatial distribution and velocities have been determined from ion time of flight (TOF) measurements. Appropriate plume expansion models are applied to the measured data for both small and large beam sizes.

5.2 Experimental setup

A regeneratively amplified Ti:Sapphire laser (TSA-10, Positive Light) delivering 100 fs (fwhm) pulses at 800 nm is used for target irradiation at a pulse repetition rate of 10 Hz. The laser beam is focused on an Al target (99.99 % pure, ACI Alloys Inc, USA) using a $f=40$ cm plano-convex lens. The target is kept in a vacuum chamber where a base

pressure of 10^{-5} Torr is maintained. Laser irradiation area on the target surface is varied by translating the focusing lens along the beam path. A constant laser pulse energy of ~ 6 mJ is used for irradiation. Beam size on the target is measured using a beam profiler (WinCamD CCD, Thorlabs). The irradiation area of the beam on the target is varied by changing the position (z) of the focusing lens, with $z = 0$ corresponding to the target being exactly at focus. Positive and negative values of z indicate target positions before and after the focus respectively. The lens position, beam diameters and fluences are given in Figure 5.1.

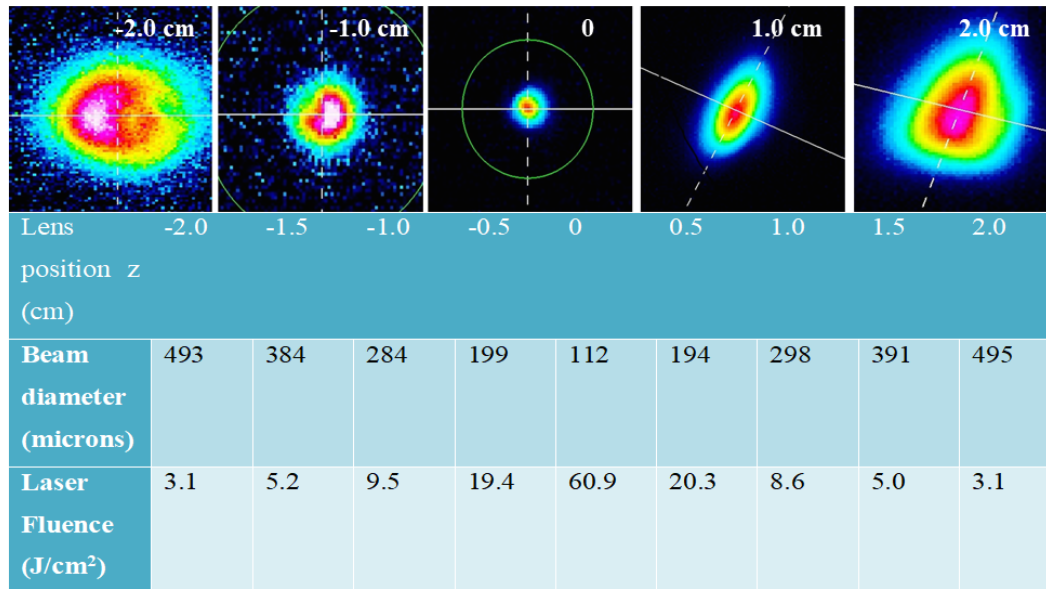


Figure 5.1: Beam diameter and fluence on the target as a function of lens position (z). When $z = 0$ the target is exactly at the beam focus, where the beam diameter is 112 microns and the laser fluence is $60.9 \text{ J}/\text{cm}^2$.

Images of the expanding plasma plume are recorded for different delay times with respect to the laser pulse, using an Intensified Charge Coupled Device (ICCD, Andor istar CCD 334) equipped with an $f/2.8$ aperture lens (Nikon, Micro-NIKKOR-5 mm). A grating spectrometer (iHR 320, Horiba Jobin Yvon 1200 grooves/mm grating) housing a CCD detector (Synapse, Horiba Jobin Yvon), used for OES measurements. Ion emission in time is observed by using a negatively biased Faraday cup (FC-Kimball physics) kept at a distance ~ 10 cm from the target at an angle $\sim 20^\circ$ with respect to the target normal.

5.3 Results and Discussion

Ablation of the surface will occur for laser fluences which exceed the ablation threshold of the target material (Gamaly et al. 2002). The ablation threshold of Aluminium is $\sim 0.1 \text{ J/cm}^{-2}$ for ultrashort laser pulses (Le Drogoff et al. 2001). The laser penetrates the target causing heating of electrons in the skin layer. Electrons will immediately escape from the target if their energy is higher than the Fermi energy, and a plume will be created if the energy of the ions is greater than the lattice binding energy. Due to differences in the drift speed of electrons and ions in the plume, a space charge separation occurs which results in a time-dependent ambipolar electric field. This field will act on both ions and electrons, resulting in a speeding up of ions and slowing down of electrons. These ions will appear as a fast component in time-resolved measurements. On the other hand, part of the laser energy deposited on the target will be transferred to the phonon modes, and the lattice will eventually thermalize, such that the electron and ion temperatures are equalized. As a result thermal ablation occurs, and the species ejected from the target at this stage will form a relatively slow component. Thus the plasma plume will consist of both fast and slow moving species.

We carried out a detailed study to understand the physical mechanisms of plume generation for various beam sizes using OES, ICCD imaging, and ion current measurements. Optical emission spectroscopy (OES) is used to study the emission of atomic and ionic species present in the plasma (Aragón and Aguilera 2008; Coburn and Chen 1980). Each metal plasma has its own characteristic line emission which can be identified from the NIST database to recognize its neutral and ionic species. The emission spectra recorded from the plume at a distance of 2 mm from the target surface, for different lens positions, are given in Figure 5.2. From the measured emission intensities of neutrals and ions shown in the inset, it is clear that intensities are higher for smaller beam sizes. Intensities of the species are slightly higher after the focus compared to that before the focus, which is probably due to astigmatism of the beam.

Time integrated images of the plasma plume recorded using a gate width of 500 ns

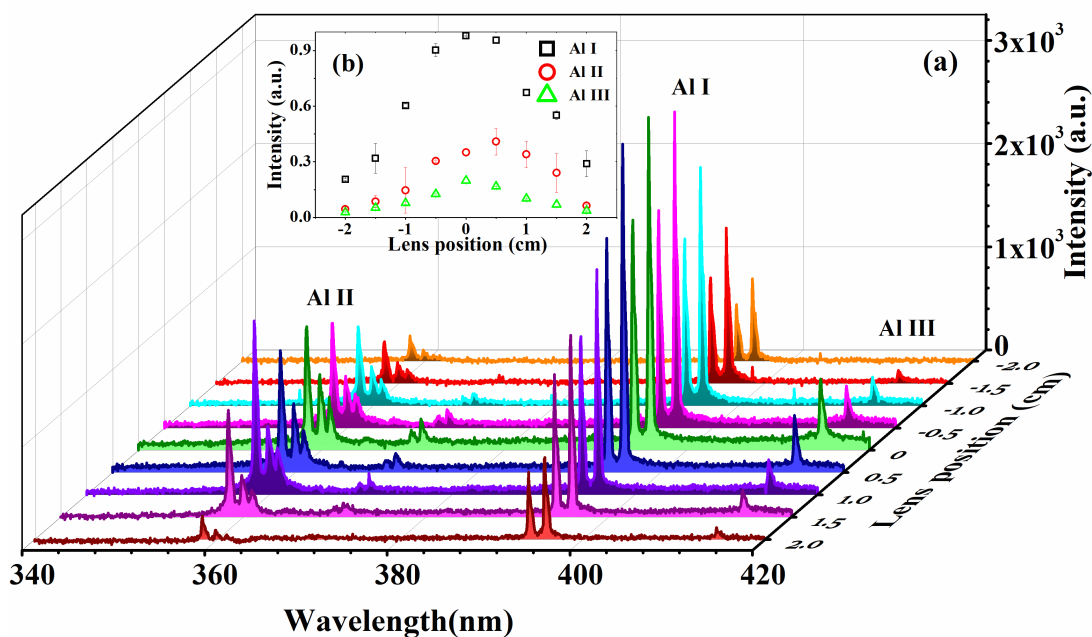


Figure 5.2: Optical emission spectra of the plasma plumes measured at a distance of 2 mm from the target surface, for different laser beam sizes. The spectra are recorded with 100 ns integration time. Inset shows emission intensities measured for Al I (396.15nm), Al II (358.65 nm) and Al III (414.99 nm) respectively.

for the ICCD, for different lens positions, are given in Fig 5.3 Corresponding images of Al^{2+} emission, obtained by keeping a bandpass interference filter (Andover Corporation) centered at 415 nm in front of the ICCD camera, are also shown. Plume shape is spherical when the target is at beam focus. As the beam size increases the plume assumes a near-cylindrical shape because of the increased presence of vaporized particles, which acts as a piston pushing the plume forward (Nadezhda et al. 2000). Intensities of the Al^{2+} plume and the overall Al plume are more comparable at the beam focus, compared to that away from the focus. This is because away from the focus the plume mostly consists of neutrals due to the lower degree of ionization. Ionization is highest at and near the focus.

Time-resolved ICCD images acquired for different beam sizes on the target, at different times within the delay period of 50 to 550 ns, are given in Figure 5.4. In the initial phase of plume expansion the ablated species move away from the target surface with supersonic speeds. While fast-moving ions located at the frontal region of the plasma acquire high energies during hydrodynamic acceleration, neutrals, molecules

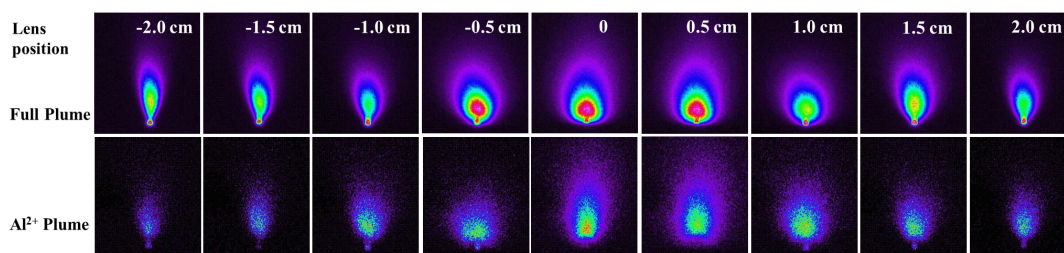


Figure 5.3: Time integrated ICCD images of the full plume and Al^{2+} plume recorded for various beam sizes. Images are acquired for an integration time of 500 ns. Each picture is the average of 10 images taken for successive laser shots.

and electrons propagate relatively slowly (Stoian et al. 2000; Stoian et al. 2002; Reif et al. 2004). Spatial and temporal splitting of the plume into fast and slow species is observed at higher delays. Previous reports for different fluence and ambient conditions (Gurlui et al. 2008; Harilal, et al. 2002; Harilal, et al. 2003), show that space charge separation, thermal ablation and laser-target energy coupling influence plume splitting significantly. Increasing the beam size at constant laser energy on the target leads to an increase in the density of vaporized species (Wolff-Rottke et al. 1995). This dense vapour plume contains solid and liquid clusters of material, which form the slow species. The space charge field that accelerates the ions will provide higher velocities for the higher charged ionic states (Gamaly 2011; Bulgakova et al. 2000). The recoil of slow species by the fast-moving species inside the plume can cause shocks in the slow species (Witanachchi and Mukherjee 1995). A nearly stagnant region can be seen in Figure 5.3 close to the target for larger beam sizes, which is the emission from the slow moving nanoparticles formed in the plasma. Obviously, plume formation and the processes which follow rely significantly on the laser beam size on the target.

To understand the above observations in more detail, we note that an intense laser pulse irradiating a plane target leads to the ejection of electrons and ions, and subsequent heating of a thin plasma layer. The heat wave propagates further into the solid (heat-conduction zone) exerting high pressure on the surrounding solid material. This results in an intense shock wave, which travels to the interior of the target (Kessel 1975; Montross 2002; Fabbro et al. 1990). Due to momentum conservation, the momentum imparted to the compressed solid in the form of the shock wave forces the

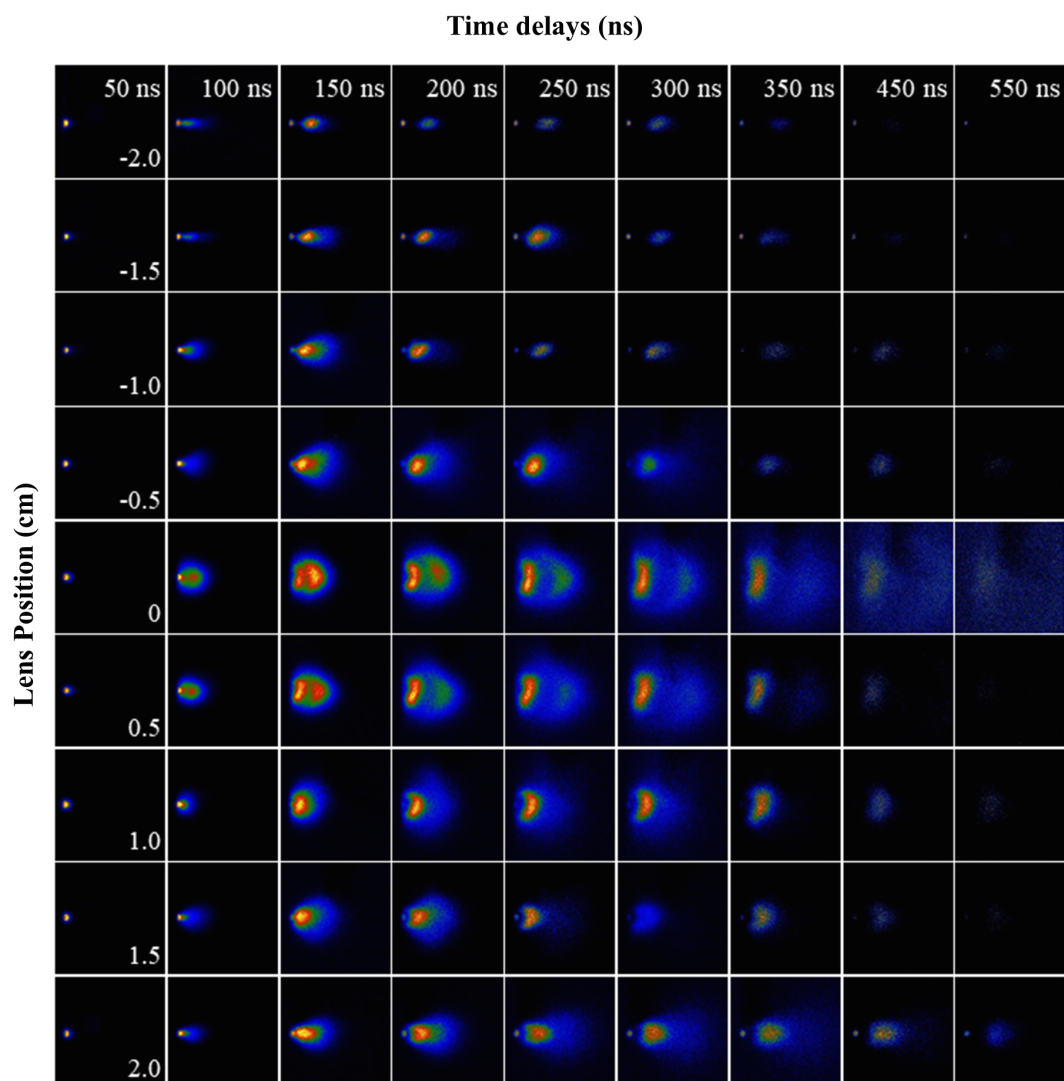


Figure 5.4: Time-resolved ICCD images of plume expansion during the period 50 ns to 550 ns after laser irradiation, for different beam sizes on the target.

out-flowing plasma to balance the momentum at each instant of time (Kessel 1975). Therefore, the slow-moving species resulting from thermal ablation has a kinetic signature similar to that of shock waves. As the beam size increases, number density of the vaporized species also increases. Further heating of the target by the laser-produced plasma can promote enhanced vaporization of the material from the target surface. The vapour leaving the surface carries the shock wave, the magnitude of which depends on the mass flux. Therefore, the shock wave model is well suited for laser produced plasma at higher beam sizes (Kessel 1975). In this regime the pulse energy is distributed to a larger interaction area, resulting in an increase in the thermally ablated species (slow

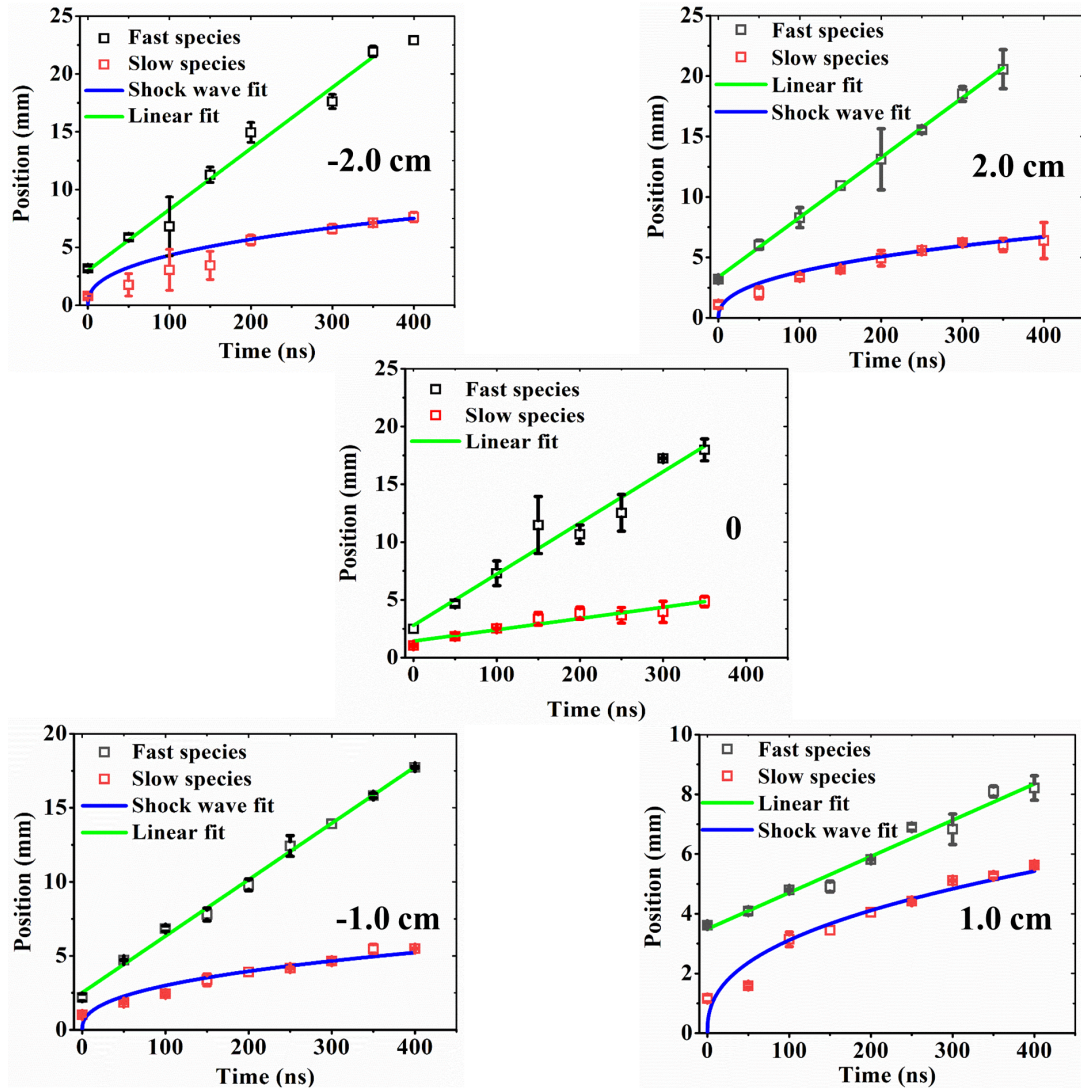


Figure 5.5: R-t plots drawn using the ICCD images. Solid lines and curves are numerical fits to the plume expansion data using the free expansion and shock wave models respectively.

species). The dynamics of the slow species follows the shock wave model, while that of the fast species follows a free expansion model. In the shock wave model the position of the plume is given by (Gonzalo, et al. 1997)

$$R = \zeta_0 \left(\frac{E_0}{\rho_0} \right)^{\frac{1}{5}} t^{\frac{2}{5}} \quad (5.1)$$

where ζ_0 is a constant related to the specific heat capacity, E_0 is the amount of energy released, and ρ_0 is the ambient gas density. Numerical fits of the free expansion and

shock wave models to the position-time (R-t) plots of the plumes are given in Figure 5.5. The velocity of the species is highest at the focus and it decreases with increasing beam size, indicating a corresponding decrease in the species kinetic energy.

From time of flight (TOF) measurements carried out using a Faraday Cup, we have also investigated specifically, the influence of beam size on ion emission from the plasma. For collecting the ions the FC is positioned at a distance of 11 cm from the target surface, at an angle of approximately 20 degrees with respect to the target normal. Ion TOF data shown in Figure 5.6 provides the kinetic distributions of Al ions obtained for different laser beam sizes before and after the focus. While a relatively sharper and higher peak with a low wing is observed for the beam focus, a well resolved double peak is seen for higher beam sizes. Taking time-resolved ICCD images (Figure 5.3) also into consideration, the double peak structure confirms the presence of fast and slow ions which travel at different velocities. The fast peak is sharper and taller for smaller beam sizes because of the ejection of more energetic ions into the plasma plume. As the beam size increases the peaks get spread out, and the slow peak gains more prominence. Bulgakova et al. has reported that a larger target-collector distance facilitates the observation of double-peaked ion data at lower fluences as well (Bulgakova et al. 2000).

Because of the space charge field that constrains their motion, electrons and fast ions move together with a mutual separation which is less than a Debye length (van Ingen 1994). The time scale for ambipolar plasma density redistribution is given by $\tau_d = \frac{r}{C_s}$ where r is the laser beam size and C_s is the ion sound speed. When beam size is increased the time scale of the ambipolar process is increased, limiting the effectiveness of ambipolar diffusion (Zhang et al. 2002). Moreover, the corresponding lower fluence results in a larger contribution from thermal ions, which will be enhanced at relatively later time scales. The energy is spread over a large impact area, and material ejection takes place primarily in the form of atoms and clusters, resulting in reduced ion flux. Thus the fast peak becomes suppressed and ion ejection gets spread out in time. On the other hand, for small beam sizes at and near the focus, the energy density coupled

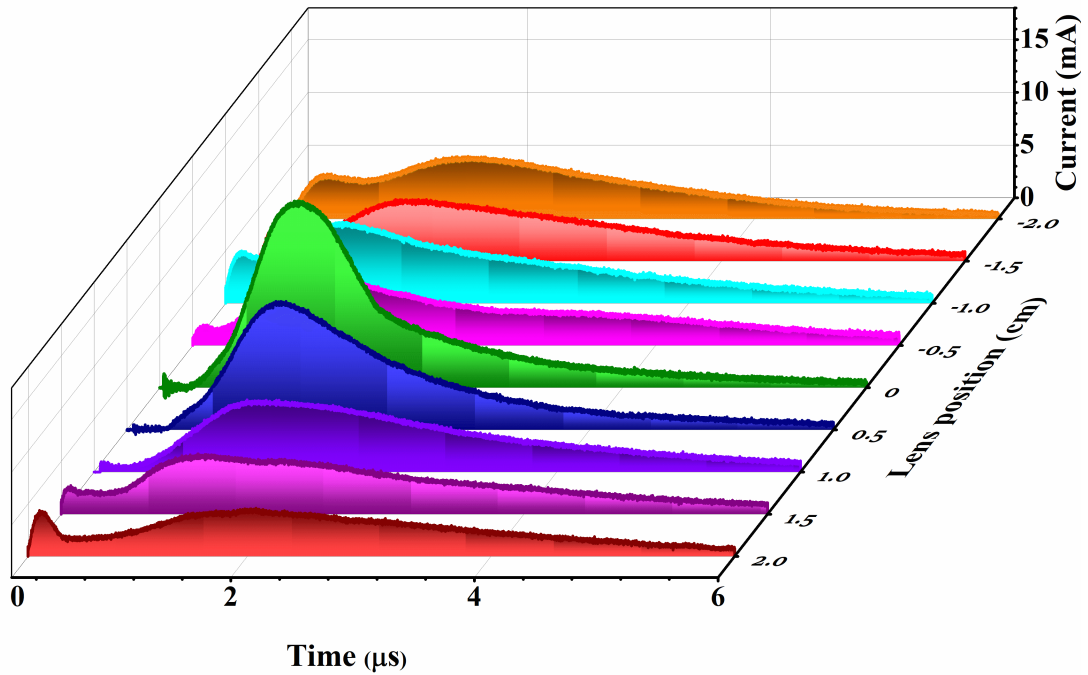


Figure 5.6: Ion TOF spectra of the plasma for different laser beam sizes, acquired using the Faraday cup. The fast peak is very prominent when the target is at the beam focus. The slow peak becomes prominent away from the focus.

to the target will be much higher. At the beam focus a significant overheating of the absorbed volume happens, and the material is directly transformed into the gas phase (Witanachchi and Mukherjee 1995), which leads to higher ionization and higher ion kinetic energies. The timescale for ambipolar diffusion is less, and a significant ejection of accelerated ions will happen during early times after irradiation. Ions produced by the thermal process will be relatively less in comparison. Thus, the fast peak becomes more prominent in this case.

Ion flux and velocities can be determined as a function of beam size using the FC data which is shown in Figure 5.7 and 5.8. We integrate the TOF signal over the fast peak and thermal peak regions separately to get the total collected charge Q (Anoop et al. 2015),

$$Q = \frac{1}{R} \int I(t) dt \quad (5.2)$$

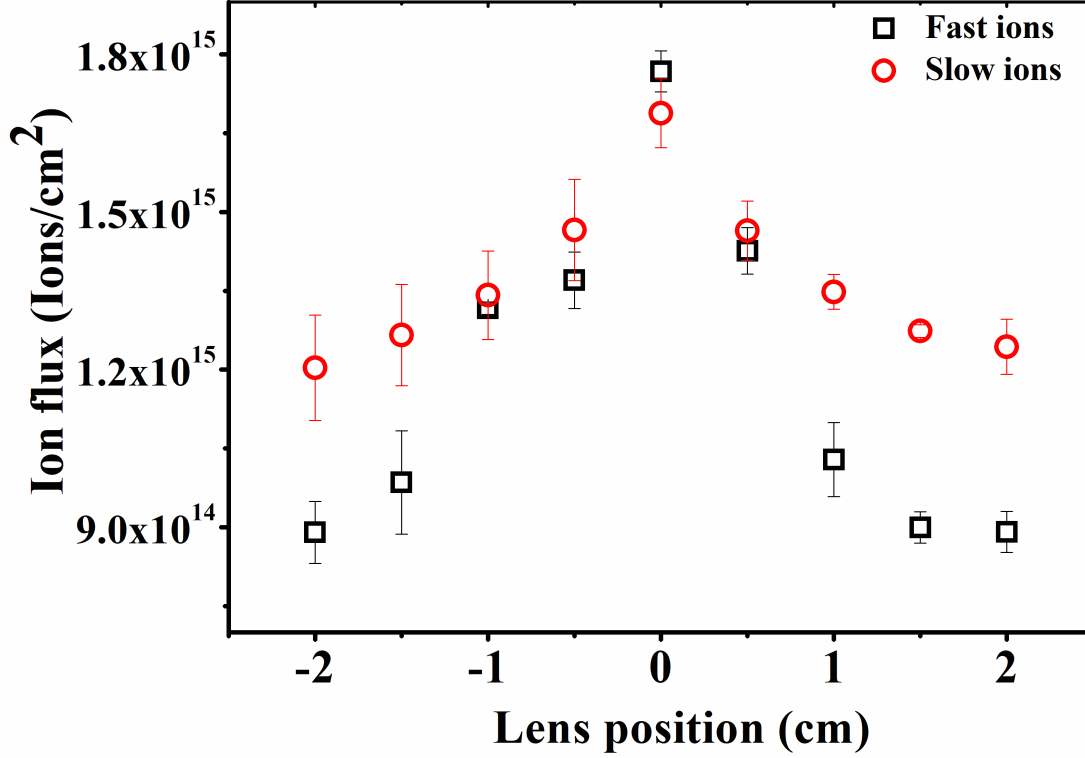


Figure 5.7: Ion flux of fast and slow ions measured for different laser beam sizes using the Faraday cup.

where $I(t)$ and R are the measured time-dependent current and circuit resistance (50 ohms) respectively. The ion flux given by Q/A , where A is the FC area of charge collection (5 mm^2), is in the order of 10^{15} ions/cm². The average ion velocity $\langle v \rangle$ is given by (Donnelly et al. 2010),

$$\langle v \rangle = \frac{\int \frac{L_p}{t} I(t) dt}{\int I(t) dt} \quad (5.3)$$

where L_p is the distance of FC from the target. The velocities of both fast and slow ions are high towards the focus, and they gradually decrease away from the focus. While fast ions reach velocities beyond 500 km/s at the beam focus, that of the slow ions is one order of magnitude lower, at around 50 km/s. The velocity of the ions will depend on their charge state, and the space charge field that accelerates ions will cause higher velocity for the higher charge states (Sankar et al. 2017).

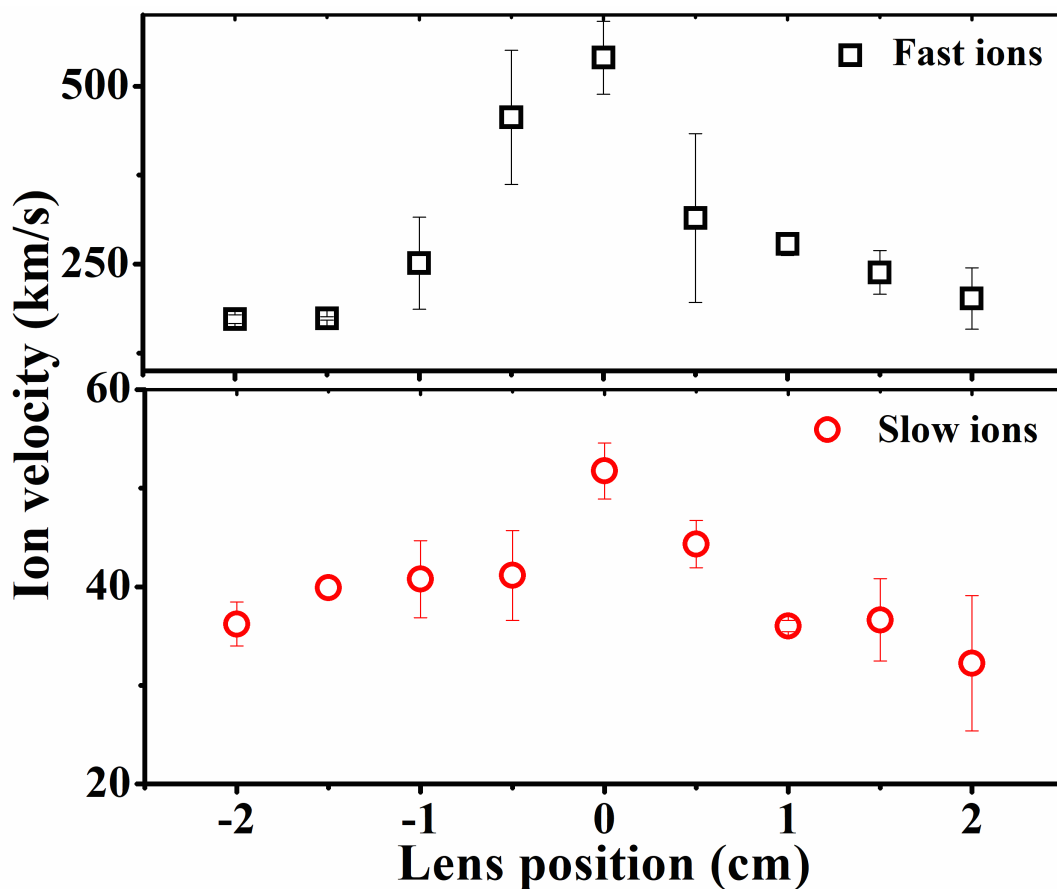


Figure 5.8: Ion velocities of fast and slow ions measured for different laser beam sizes using the Faraday cup.

5.4 Summary

In summary, laser-produced aluminium plasmas have been investigated in low vacuum for different laser beam sizes using the techniques of OES, time-resolved ICCD imaging, and ion current measurements. From OES studies it is seen that smaller beam sizes produce higher emission intensities and ion populations relative to larger beam sizes. While larger beam sizes result in cylindrical plumes, smaller beam sizes result in spherical plumes. ICCD imaging and ion current measurements show spatial and temporal plume splitting during hydrodynamic expansion. The dynamics of fast and slow species is extracted from time-resolved ICCD images. Propagation of the slow-moving species is well predicted by the shock wave model, while that of the fast species fits to a free expansion model. Faraday cup signals show two peaks in the TOF profile, correspond-

ing to distinct fast and slow ion species. Ion flux and velocities are higher for smaller beam sizes compared to larger beam sizes. To sum up, the role played by the laser beam size in determining the nature and dynamics of laser-produced Al plasma plumes will be of importance to several applications including pulsed laser deposition, ion beam generation, micromachining and laser welding.

CHAPTER 6

MULTIDIAGNOSTIC ANALYSIS OF TUNGSTEN PLASMAS GENERATED BY ULTRASHORT AND SHORT LASER PULSES

Tungsten is being widely used in fusion reactors as an effective plasma-facing material. A comparative study of ultrashort pulse laser ablation (ULA) and short pulse laser ablation (SLA) has been carried out. In the present work, we comprehensively investigate the expansion of a laser produced tungsten plasma into ambient air for background pressures ranging from 10^{-5} to 760 Torr, employing the diagnostic tools of optical emission spectroscopy, time-resolved imaging, ion time of flight measurements, and surface morphology analysis.

“Physics is, hopefully, simple. Physicists are not.”

————— *Edward Teller*

6.1 Introduction

Tungsten (W) is a unique candidate for divertor and first wall material in the activated phase of ITER (international thermonuclear experimental reactor), and for plasma facing components in nuclear fusion devices (Yoshida 1999), because of its high melting point, high thermal conductivity, low erosion rate, and low sputtering yield (Yoshida 1999; Roth et al. 2008). Investigation of its properties and behaviour is therefore highly important, in view of its application in withstanding the extreme radiation and heat produced in high energy density plasmas facilitating fusion reactions (Labaune et al. 2013). Therefore, in this work we undertake detailed studies of laser produced plasma (LPP) from a tungsten target excited by ultrashort (100 fs) and short (10 ns) laser pulses, employing the diagnostic tools of optical emission spectroscopy, time resolved plume imaging, and ion time of flight measurements.

Recent experimental observations have revealed that the formation of holes and bubbles by exposure to plasma may lead to the degradation of the characteristic properties of tungsten (Kajita et al. 2006), especially, its thermal diffusivity. Degradation of thermal diffusivity may cause serious problems such as melting. Nanostructures on tungsten samples can degrade the optical reflectivity and thermo-physical properties of the surface (Buzi et al. 2017; Kajita et al. 2018). In fusion experiments such damages can cause problems to the in-vessel metal mirrors and plasma-facing components (Buzi et al. 2017). Therefore, it is essential to investigate the ablation properties and evaporation processes of tungsten targets irradiated with high-power lasers. Hence, investigations of the performance of tungsten under intense electromagnetic radiation and the emissions from it are of fundamental interest for plasma physicists and engineers (Malka et al. 2008).

Laser irradiation of a target is followed by the vaporization of the target resulting in a transient plasma plume, which expands into the ambient gas. The gas environment plays a substantial role in the evolution and expansion of the plasma (Black 2011). Processes such as laser-plasma interaction (Lu et al. 1999), plasma confinement (Gamaly et al. 2002), shielding, and formation of shock waves (McKenna & Scottish Universities Summer School in Physics (68th: 2011: University of Strathclyde), 2013), the environmental conditions, and initial conditions (Effenberger and Scott 2010). Ion emission from tungsten plasma has been studied in the past since it is a rich ion source with applications in devices such as high energy ion implanters and laser ion sources (Radtke et al. 2001; Biedermann et al. 2009; Ilyas et al. 2012). Similarly, there are studies on the effects of applying electric and magnetic fields on laser produced tungsten plasma (Woowski et al. 2002), formation of holes/bubbles on the surface when tungsten is exposed to helium plasma at a sufficiently high temperature (Kajita et al. 2007), and erosion of plasma facing tungsten plates (Beigman et al. 2007). Some groups have investigated the influence of the laser wavelength (IR, Green, UV) on tungsten plasma parameters (Harilal et al. 2013; Farid et al. 2013). Recently, optical emission studies of W using a Nd:YAG laser is reported by some groups (Wu et al. 2017, 2019).

Nevertheless, there are no reports in literature on the role of the ambient gas on the formation and hydrodynamic evolution of laser produced tungsten plasmas. Moreover, a comparative study of ultrashort and short pulse laser produced plasmas from tungsten also has not been carried out. Therefore, in this work, we have employed multiple diagnostic tools (optical emission spectroscopy, Time resolved imaging, ion time of flight measurements, surface morphology analysis) to record and analyze the plasma generated from a tungsten target, which is irradiated using ultrashort (100 fs) and short (7 ns) laser pulses. The free expansion, shock wave and drag models have been used to model the evolution of the plasma for ambient pressures ranging from 10^{-5} to 760 Torr. In addition, craters formed on the target surface by laser irradiation during plasma generation are imaged and analyzed. These studies are of significance to a multitude of applications including Pulsed Laser Deposition (PLD), Ion beam generation, and nuclear fusion.

6.2 Results and discussion

Expansion of laser produced plasma plumes into an ambient of relatively low as well as high background pressures has been studied for a number of target materials in the past. On the other hand, only a couple of studies (Rumsby and Paul 1974; Cveji 2014) have been reported in which plume dynamics at intermediate background pressures (in the range of 1 Torr to 100 Torr) has been investigated (Tsui and Fedosejevs 2004). Because of the importance of collective effects such as compression of the plume and the gas, plume-gas diffusion etc., in this study we have investigated plume expansion in a broad pressure range to understand the phenomenon in more detail.

Ablation of the target will happen for any laser fluence that exceeds the threshold fluence of the material. The threshold fluence for ULA can be calculated using the equation 3.1 (Gamaly et al. 2002). The ULA threshold fluence thus obtained for tungsten is 0.43 J/cm^2 , which is in excellent agreement with the published result (Byskov-Nielsen et al. 2010). For SLA the ablation threshold is given by the equation 3.2 and it is obtained as 5.85 J/cm^2 . The experimental fluence is almost 100 times higher than the ULA ablation threshold but in SLA, fluence is only 8 times higher. It is good that, the fluence used to ablate the tungsten target is well above the threshold fluence.

6.2.1 Optical Emission Spectroscopy (OES)

The optical emission spectra of tungsten plasma for ULA and SLA at different ambient pressures is shown in Figure 6.1. The spectral lines are identified using the standard NIST database.

For the entire pressure range studied, the net plume intensity is found to be higher for SLA compared to ULA. Neutral lines are more prominent than ion lines in both cases. The ULA plume undergoes fast recombination processes resulting in a higher number of neutrals (Labutin et al. 2016). Moreover, due to the absence of laser plasma interaction, further ionization is not possible in the case of ULA (Freeman et al. 2013). However, in SLA, the leading edge of the ns laser pulse deposits energy onto the target

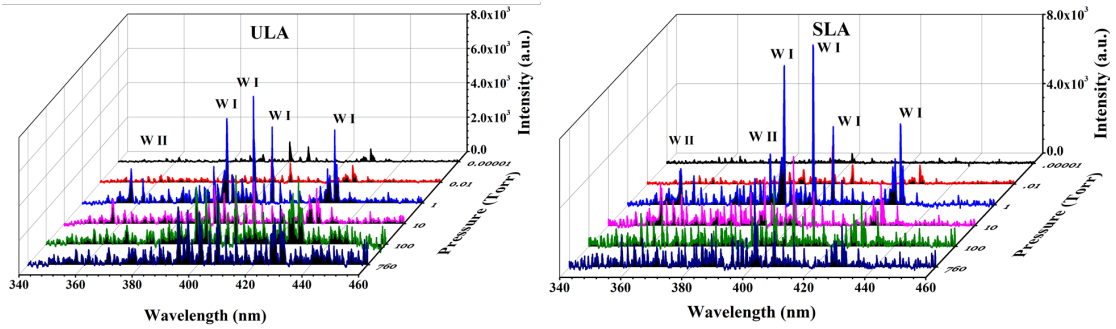


Figure 6.1: Optical emission spectra of the plasma generated by ultrashort (ULA, 100 fs) and short (SLA, 7 ns) laser pulses, measured for $z = 1$ mm, for different ambient pressures (P).

creating the plasma, and much of the remaining pulse (the trailing edge) being absorbed by the expanding plasma, directly heating and ionizing the plume resulting in ionic line emission. The intensity of spectral lines is very low in vacuum. Since the plasma plume expands adiabatically and undergoes free expansion. Thereafter the intensity rises up to 1 Torr, beyond which it drops again. At higher pressures, the energy dissipation of plume to the background gas by elastic collisions cause for the reduction of the emission intensity of the plasma. These two processes balance each other to give maximum emission at a pressure of around 1 Torr.

Assuming local thermodynamic equilibrium (LTE), the electron temperature (T_e) can be evaluated using the Boltzmann distribution function, which is given by the following relationship (Aragón and Aguilera 2008),

$$\ln\left(\frac{\lambda_{ij} I_{ij}}{g_i A_{i,j}}\right) = \frac{-E_i}{K_B T_E} - \ln\left(\frac{4\pi Z}{h C Z_0}\right) \quad (6.1)$$

where λ_{ij} , A_{ij} , g_i , I_{ij} and E_i are the wavelength, transition probability, statistical weight, line intensity, and energy of the excited state respectively, and K_E is the Boltzmann's constant. The spectroscopic constants (A_i and g_i) are taken from the NIST database. Under the LTE, a Boltzmann plot of the logarithmic term k_{ij} , I_{ij} , g_i , A_{ij} versus E_i yields a straight line whose slope is equal to $-1/kT$. The calculated plasma temperatures for different ambient pressures are shown in Figure 6.2a. The neutral transition lines of tungsten used for calculations are taken from the NIST database, which

are given in Table 6.1.

Wavelength (nm)	Excited state energy E_i (eV)	$g_i A_{ij}$ (S^{-1})
386.60	4.914315	1×10^7
393.04	5.010340	7.11×10^6
400.87	3.457880	1.47×10^8
407.43	3.408091	7×10^7
426.02	5.15566	8.7×10^7
429.46	3.252077	6.2×10^7

Table 6.1: Spectroscopic data of tungsten neutral lines (W I) used for the estimation of electron temperature.

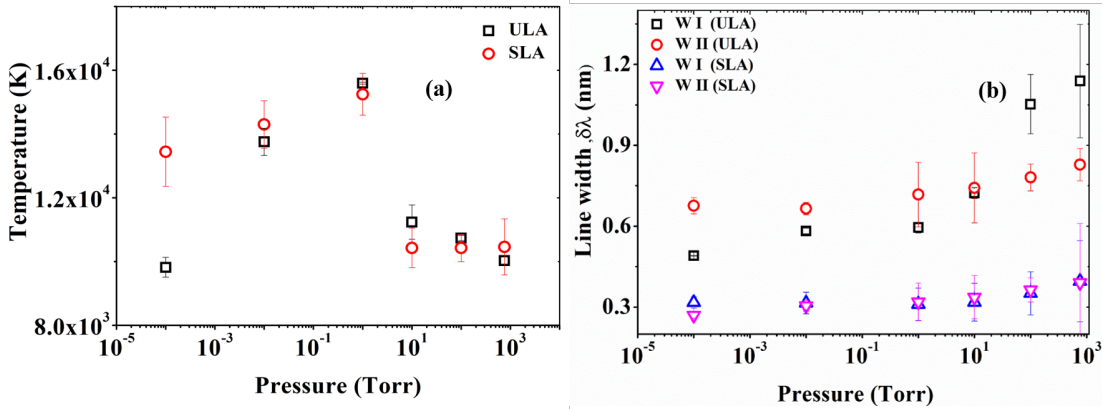


Figure 6.2: (a) Electron temperature and (b) Stark broadening ($\delta\lambda$) plotted against ambient pressure, measured at a distance of 1 mm from the target surface, for a laser fluence of 44 J/cm^2 .

The temperature of the plasma is higher for SLA in comparison to ULA, because of the laser plasma interaction. The temperature of SLA is slightly higher than the temperature of ULA until 1 Torr, and becomes equal at higher pressures. In both cases, adiabatic expansion of the plume results in reduced collisional excitation at lower pressures. While increasing the ambient pressure, enhanced collisions between plasma electrons and ambient gas results in thermal leak from the plasma, reducing the plasma temperature. However, the energy lost (thermal leak) is proportional to the elastic scattering cross section of the electron (σ_{ea}) and the density of the background gas (n_B) through the equation 3.3 as mentioned in third chapter. Similar to emission intensity, tempera-

ture also peaks around 1 Torr due to the optimal balance between collisional recombination, ionization, and thermal leak at that pressure.

The Stark broadening is the most common line broadening mechanism observed in LPPs (Sarkar and Singh 2017; Konjevi et al. 2012) due to the electric fields generated inside the plasma will perturb the energy levels of atoms and ions, shifting their energy levels (Stark effect). We have used 400.87 nm (W I) as neutral line and 357.24 nm (W II) as ionic line in both ULA and SLA. From figure 6.2b it is clear that the line width ($\delta\lambda$) of neutrals and ions remains nearly the same for the pressure range of 10^{-5} to 1 Torr. Beyond this pressure $\delta\lambda$ increases. The spectral full width at half maximum (FWHM) of the emission line (in \AA) is given by the equation 3.5 mentioned in chapter 3. Which is directly proportional to the number density (N_e). At lower pressures reduced collisional interactions between the emitters and perturbers due to the adiabatic expansion of the plume results in lower Stark broadening contributions from both neutrals and ions (Rao et al. 2016). An increase in the ambient pressure leads to the confinement of the plasma plume and increased collisions, resulting in enhanced Stark broadening. The lower line width measured for SLA is due to the relatively lower electric field associated with the short laser pulse. The calculated electric fields are 1.732×10^{11} V/m for the ultrashort pulse and 1.732×10^9 V/m for the short laser pulse, respectively, for the laser fluence 44 Jcm^{-2} .

We also present stroboscopic ICCD images of plasma plume propagation for ULA and SLA. For a qualitative understanding of plasma propagation through ambient air, 2-D images of the plasma are captured by an ICCD camera. Images obtained for time delays ranging from 50 to 1050 ns, and for gas pressures ranging from 10^{-5} -760 Torr, are shown in Figure 6.3 and 6.4. Plasma lifetime is found to be less in ULA compared to SLA due to the absence of laser-plasma interaction (Sankar et al. 2018). The emission intensity, calculated from time-integrated images, is low in vacuum, which is shown in Figure 6.5. It grows with increasing pressure and attains a maximum value near 1 Torr, beyond which it decreases for both SLA and ULA. The intensity of plume species is higher in the case of SLA as compared to ULA due to the laser plasma interaction.

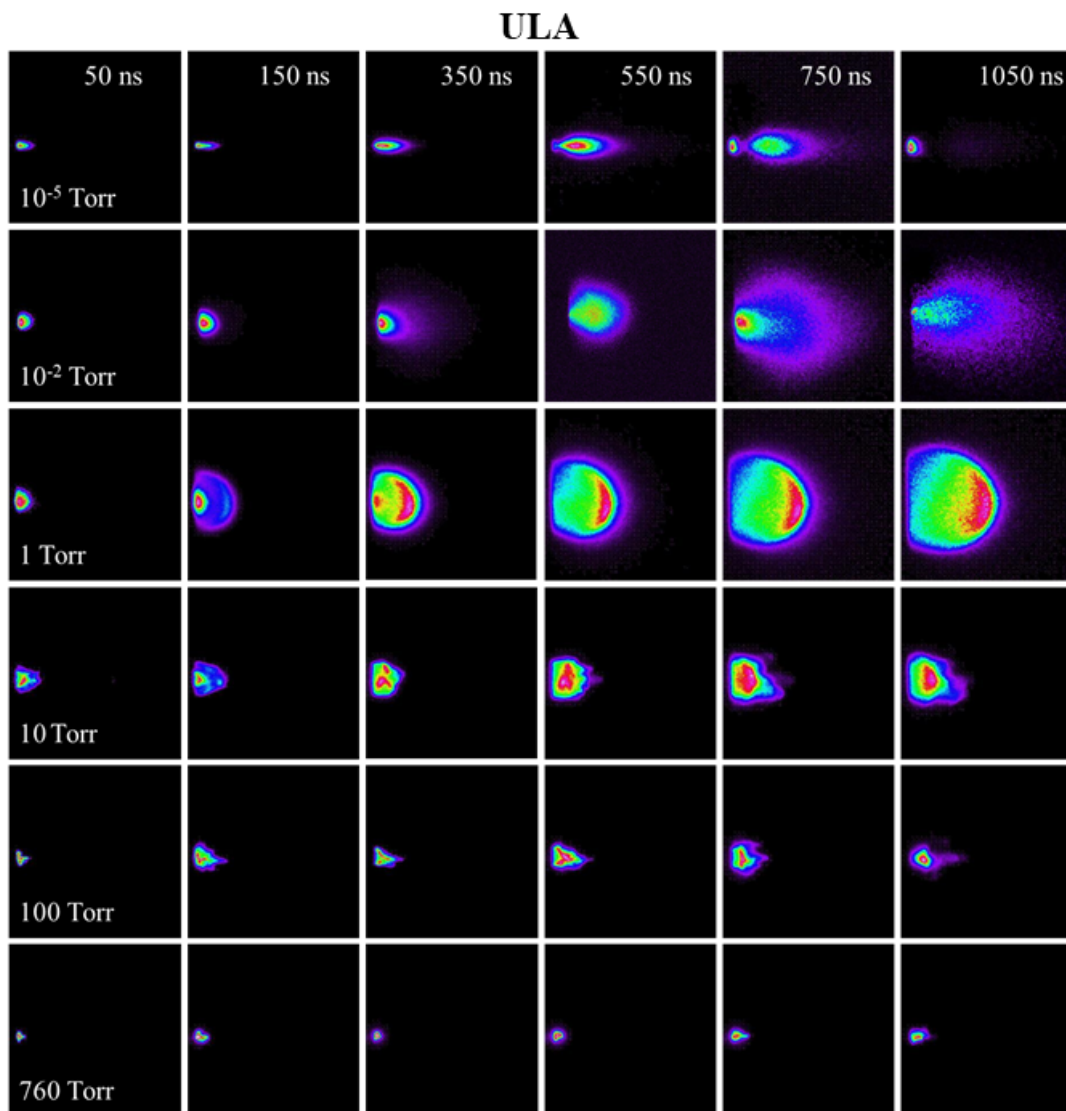


Figure 6.3: Temporal evolution of the ULA plasma plumes from the tungsten target, for ambient pressures ranging from 10^{-5} Torr to 760 Torr, at a laser fluence of 44 J/cm^2 . Each image is normalized to its maximum intensity for better view.

At higher pressures the intensity is reduced due to recombination, and thermal leak to the background gas results in a reduced lifetime of the plasma (Effenberger and Scott 2010).

There are some common observations in both ULA and SLA: in vacuum the plasma plume expands adiabatically and undergoes free expansion, while at higher ambient pressures the plasma is dense and confined to the vicinity of the target surface (Sankar et al. 2018). In vacuum the plasma envelope is cylindrical, but around 1 Torr the plume

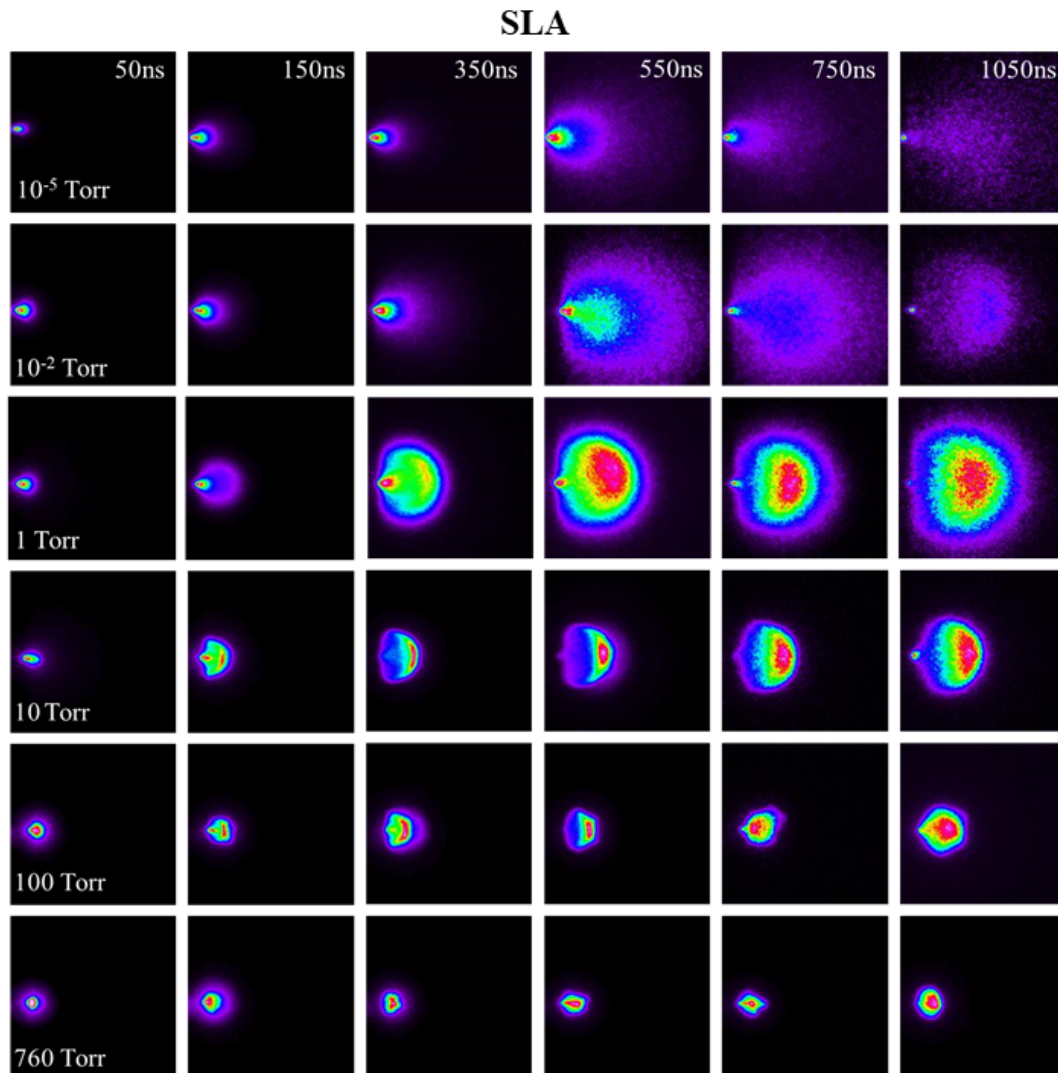


Figure 6.4: Temporal evolution of the SLA plasma plumes from the tungsten target, for ambient pressures ranging from 10^{-5} Torr to 760 Torr, at a laser fluence of 44 J/cm^2 . Each image is normalized to its maximum intensity for better view.

attains a hemispherical shape because the plasma experiences more deceleration in the axial direction as compared to the radial direction. Similarly, in vacuum, bifurcation occurs after a delay of 550 ns, splitting the plume into fast and slow moving components (Harilal et al. 2002). At higher background pressures plume splitting is not observed.

In the case of ULA plume sharpening is found to increase with pressure, as higher kinetic energy particles are emitted normal to the target surface. There are reports about the larger concentration of higher ionized species in the direction normal to the target, and their rapid decrease away from the normal (Harilal et al. 2002; Harilal et al. 2003).

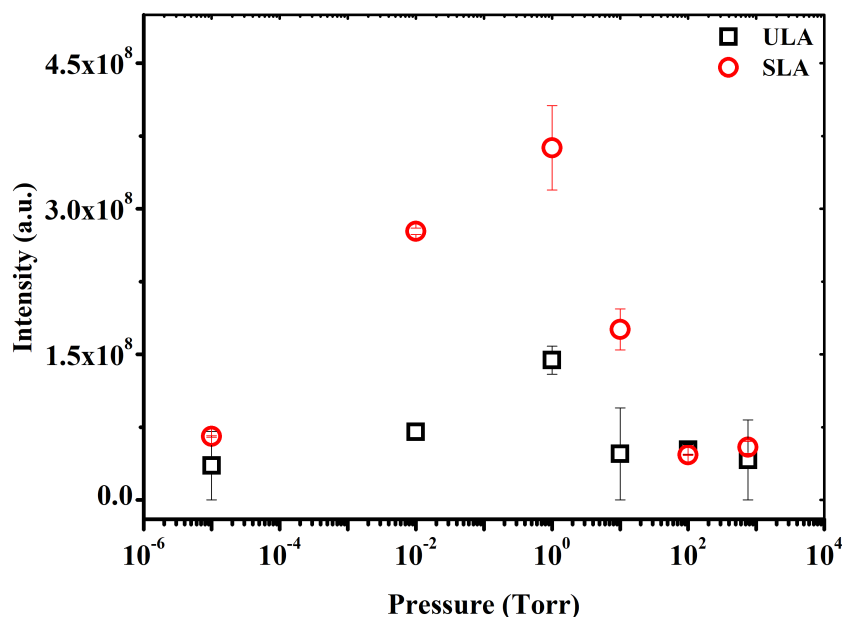


Figure 6.5: Variation of emission intensity with ambient pressure for ULA and SLA plasmas. Maximum intensity is observed in the pressure range of 1 Torr to 10 Torr. ICCD gate width is 1000 ns.

Beyond 1 Torr the plume front tends to become unstable and the boundary between the plasma and background gas is perturbed. This occurs due to the difference in the densities of plasma and background gas at the boundaries, and is known as Rayleigh-Taylor (R-T) instability (Sharma and Thareja 2005).

To explore the expansion dynamics and the velocity of LPP, the distance travelled by the plume front is plotted as a function of time. We use plume images to create the R-t plots for different pressures, which is shown in Figure 6.6 and 6.7. Using these plots, the linear, shock wave and drag models can be used to describe plasma propagation in the low, intermediate, and high pressure regimes (George et al. 2009). In vacuum, the plume expands freely, linearly with time. For ULA the vacuum velocity of the plume is 107 km/s, which reduces to 70 km/s at 10^{-2} Torr. Similarly, in the case of SLA the vacuum velocity of the plume is 112 km/s, which reduces to 83 km/s at 10^{-2} Torr. The velocity of the plume is higher in SLA because of laser-plasma interaction.

The plume propagates with a speed which is higher than that of sound. At intermediate background pressures the plume experiences perturbations due to the background

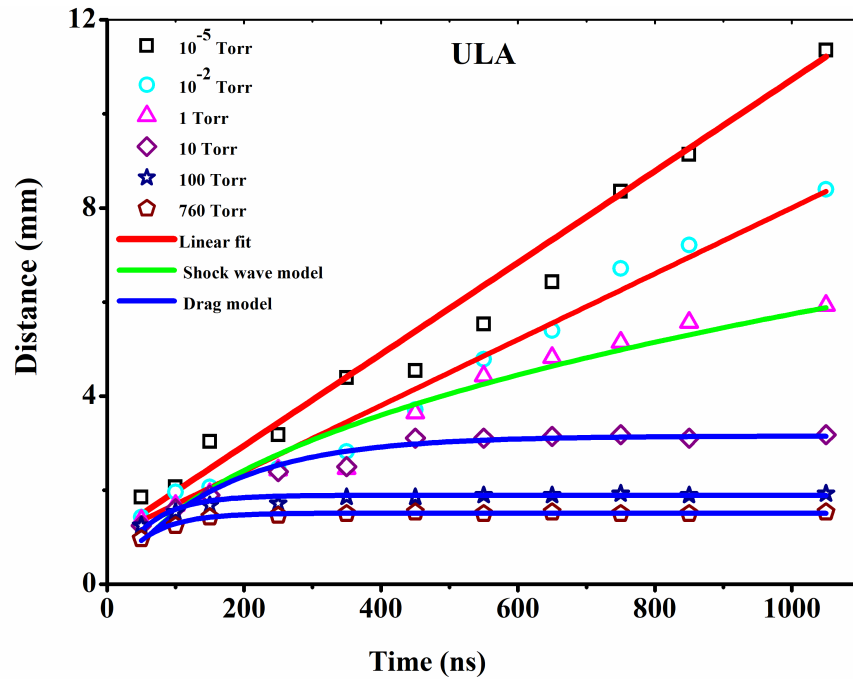


Figure 6.6: R-t plots for ULA estimated from gated ICCD images, for the ambient pressure range of 10^{-5} Torr to 760 Torr. Symbols are the measured data points while lines and curves are numerical fits to the data for different plume expansion models.

gas, resulting in a shock wave (Zhi-Hua et al. 2002). Hence plume expansion at these pressures can be described by a shock wave model, given by $R = \alpha_0 (E_0 / \rho_0)^{1/5} t^{0.4}$, where α_0 is a constant dependent on the specific heat of the ambient gas, and ρ_0 is the density of the background gas. E_0 is the amount of energy released to the background gas during the shock (Gonzalo et al. 1995). This shock wave is limited by two factors: the distance from the target at which the mass of the gas displaced becomes higher than the mass of the ejected material, and the distance from the target at which the plasma pressure becomes equal to the ambient pressure (Sankar et al. 2018). In the case of ULA, the shock is experienced only around 1 Torr but in SLA it is observed for a range of pressures from 1 Torr to 100 Torr. While pressure inside the plasma plume becomes equal to the background gas pressure after 1 Torr in ULA, in SLA this happens beyond 100 Torr. Pressure inside the SLA plume is reduced slowly on propagation compared to ULA because of laser-plasma interaction.

As the plume expands, density of the plume decreases resulting in a weakening

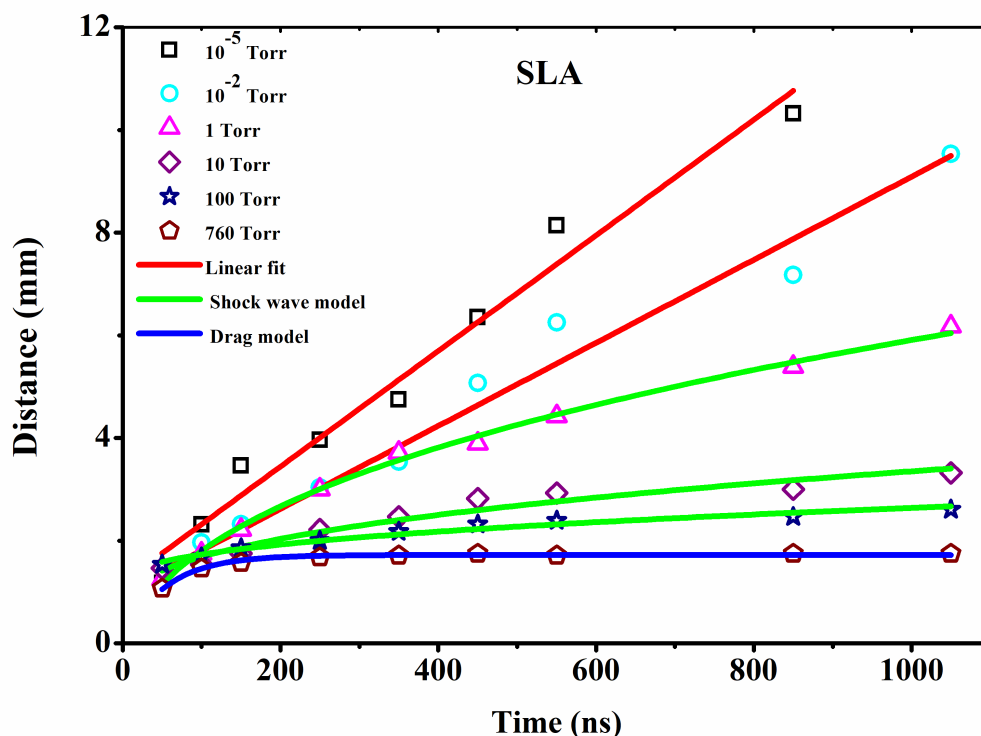


Figure 6.7: R-t plots for SLA estimated from gated ICCD images, for the ambient pressure range of 10^{-5} Torr to 760 Torr. Symbols are the measured data points while lines and curves are numerical fits to the data for different plume expansion models.

of the driving force (Gonzalo et al. 1995). At this stage, the particle front gets separated from the shock front and stops at a finite distance. When the plume pressure and ambient gas pressure become similar, the plume cannot push the ambient gas any further. Thereafter plume expansion is described by a drag model given by $R = R_0(1 - \exp(-\beta t))$, where R_0 is the stopping distance of the plume and β is the deceleration coefficient ($R_0\beta = v_0$). In ULA the ambient gas starts to drag the plume around 10 Torr. On the other hand, in SLA the drag force comes into play only at the highest pressure used (760 Torr).

6.2.2 Ion time of flight (TOF) measurements

A comparison of ion TOF from ultrashort and short pulse laser produced tungsten plasma in vacuum (10^{-5} Torr) is shown in Figure 6.8. To compare the ion signals we used a constant laser fluence of 44 J/cm^2 . ULA ions appear earlier than SLA ions

and both fast and slow ULA ions are not separable. It is due to the faster formation, expansion ULA plasma. Higher intensity of the ultrashort pulse results in a two order of magnitude higher electric field. The main difference is the distinct presence of slow and fast species in SLA, which is absent in ULA (Sankar et al. 2018). The ion TOF (time-voltage) signal can be integrated to get the total collected charge ($Q(t)$) as we done in the previous chapter 5 using the equation 5.2. The average ion velocity $\langle v \rangle$ is calculated by equation 5.3 (Ni et al. 2014).

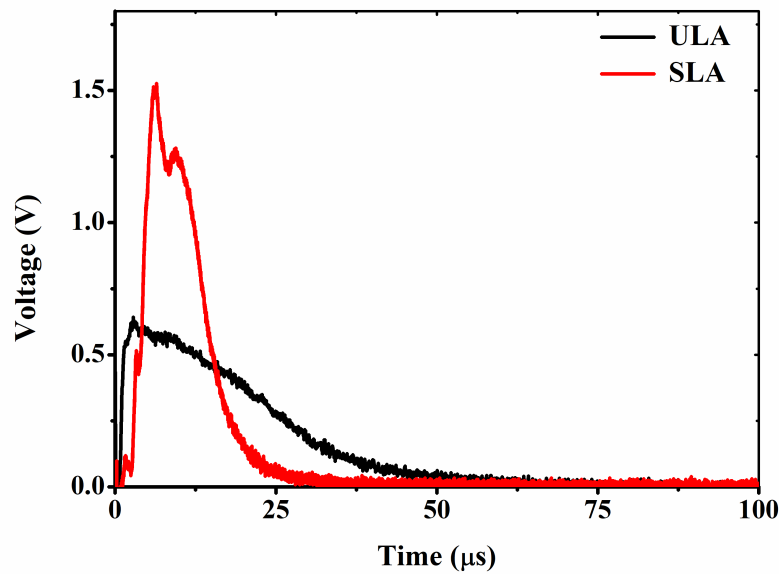


Figure 6.8: Ion TOF spectra of tungsten plasma, acquired at an angle of 20° with respect to the target normal, for ULA and SLA.

In the case of ULA the total ion flux is 3.75×10^{11} ions/mm² and the average velocity of ion species is 7.55 km/s. Fast and slow species in SLA have total ion yields of 2.84×10^{11} ions/mm² and 1.94×10^{11} ions/mm² respectively. The average velocity corresponding to the fast and slow species are 10.5 km/s and 4 km/s respectively. The fast peak in the ion current arises due to the acceleration of ions by space charge within the plasma (Elsied et al. 2016). For SLA, irradiation of the target results mostly in thermal ablation due to its relatively longer pulse duration (Dawood et al. 2015). Subsequent laser-plasma interaction will result in enhanced ionization leading to a higher density of highly charged species. Therefore, the emission and expansion of ionic species essentially depend on laser-matter and laser-plasma interactions (Freeman et al. 2013).

6.2.3 Surface structure analysis

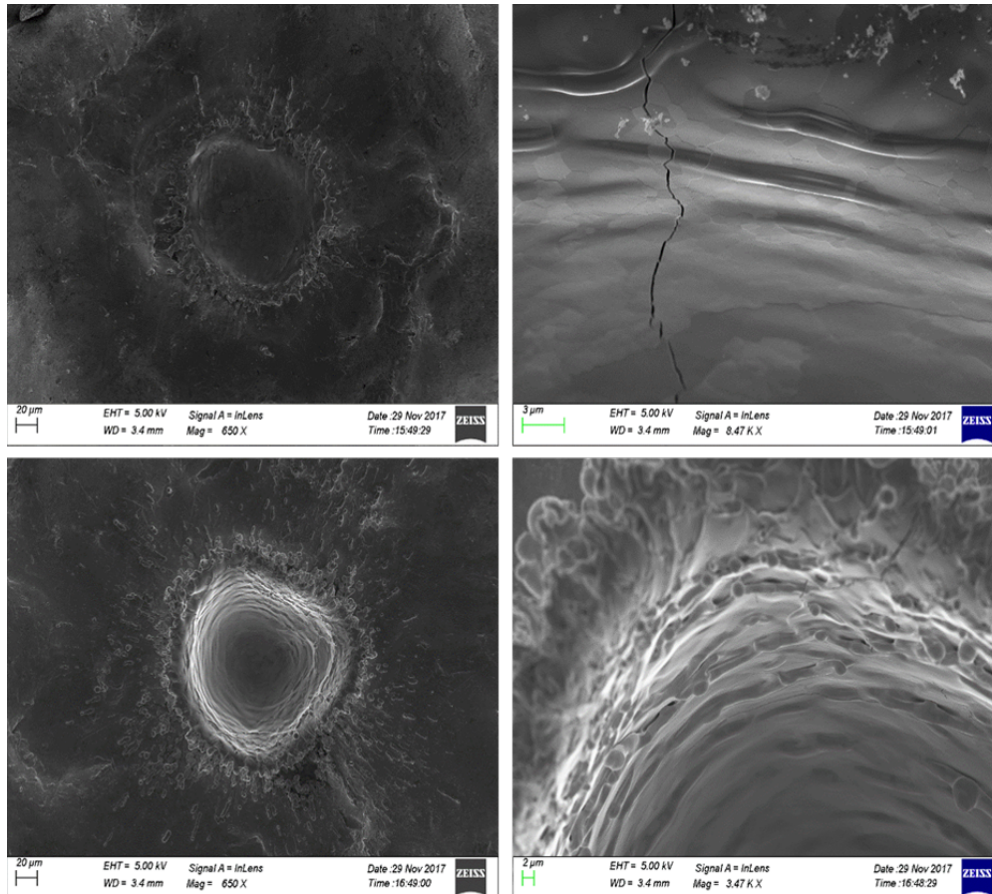


Figure 6.9: SEM micrographs of laser irradiated tungsten targets. First row shows the ULA surface, and a surface crack developed at the edge of the beam. Second row shows the SLA surface, revealing melting and recrystallization.

The SEM micrograph of the ablated surfaces for both ULA and SLA are shown in Figure 6.9. The laser fluence is kept at 44 J/cm^2 in both cases. Images are taken after 10 laser shots in each case. Images on the right side show the edges of the ablated area. In the case of ULA cracks are formed on the surface, which might have happened due to the transient increase in the temperature of the target (Ancona et al. 2009). Since tungsten has high thermal diffusivity, the ultrashort pulse generates larger stress on the target. Therefore, for sub-picosecond pulses, the material removal process is more efficient. For longer pulses the time scale for thermal diffusion is comparatively longer, reducing the stress and facilitating surface evaporation (Han and Li 2011). It is possible that a slight crack is formed after the first pulse, which becomes denser with subsequent

pulses, along with the appearance of new cracks on the surface (Tsibidis et al. 2012; Hertel et al. 2001). As the cracks widen thermal radiation inhomogeneities become more distinguishable. Cracks change the heat conductivity (Hasselman 1978), resulting in a decrease of the melting threshold near them (Li et al. 2015). A wavy surface pattern is observed after the solidification of the molten pool on the target surface.

6.3 Summary

Laser produced plasmas have been generated by irradiating a solid tungsten target with ultrashort (100 fs) and short (7 ns) laser pulses, and the hydrodynamic expansion of the resulting plasma plumes into the ambient air has been investigated for background pressures ranging from 10^{-5} to 760 Torr. Maximum optical emission from the plasma is found to occur around 1 Torr ambient pressure, because of the optimal balance between the competing processes of ionization, recombination and thermal leak. Emission intensity of neutrals is found to be higher for SLA compared to ULA. Electron temperatures of the plasmas have been estimated using the Boltzmann plot method, and Stark broadened profiles of the spectral lines have been recorded. The SLA plasma is found to have a higher electron temperature because of laser plasma interaction. Hydrodynamic expansions of ULA and SLA plumes show different morphologies. At low pressures the plume expands freely but at higher pressures the expanding plume decelerates due to plume confinement. Ion TOF studies reveal both fast and slow ions in SLA are distinguishable while in ULA which is not separable. From the obtained ion TOF signals it is found that ion species with higher average velocities are formed in SLA, and this conclusion is in good agreement with the R-t plots drawn from the ICCD images. SEM images of the irradiated tungsten surface indicate the formation of cracks that are recognizable in ULA because of the relatively faster transient temperature increase. These studies have provided important information for adjusting and optimizing laser produced tungsten plasmas for various applications in ion beam generation and fusion research.

CHAPTER 7

STUDY OF X-RAY EMISSION FROM LASER PRODUCED PLASMAS

This chapter gives a detailed study of X-ray emission from laser produced plasmas of Aluminium (Al) and Tungsten (W) targets irradiated by ultrashort and short laser pulses. X-ray emission from laser produced plasmas of Au and Ag nanoparticle suspensions flowing in the form of a thin liquid jet also is investigated.

“If the facts are not fit with the theory, change the facts”

—Albert Einstein

7.1 Introduction

The interaction of laser pulses with matter leads to the production of hot dense plasma, a rich source of hard X-rays, ‘hot’ electrons and fast ions. These hot super-thermal electrons are the signature of bremsstrahlung X-ray radiation. One of the current challenging issues is the efficient coupling of larger laser energy into a solid plasma to generate hotter electrons in the process. Research efforts are underway to optimize plasma X-ray sources produced by ultrashort laser pulses, which will be useful for X-ray lasing (Elton 1990) and soft X-ray microscopy (Chao et al. 2005), and for probing ultrafast real-time physical, chemical and biological dynamics (Oraevsky et al. 1996; Rischel et al. 1997). Dense plasmas produced by intense ultrashort laser pulses open up additional possibilities like table top acceleration (Fritzler et al. 2003) and synchrotron radiation (Rousse et al. 2004). Solid targets such as metals (Chen et al. 2008) and transparent glasses (Hatanaka et al. 2008) have been used for X-ray generation under intense femtosecond laser irradiation, while compact and efficient soft and hard X-ray sources have been developed from porous and nanocylinder (Nishikawa et al. 2001) targets. Structured surfaces such as gratings (Gordon et al. 1994; Murnane et al. 1993) and “velvet” coatings (Kulcsr et al. 2000) are able to produce enhanced X-rays from their respective metals. There is a great deal of interest in techniques which can enhance the X-ray yield, and the effects of various laser parameters and targets have been the subject of a few studies (Bagchi et al. 2011; Masim et al. 2016). Among different materials, metal nanoparticles and carbon allotropes have received particular attention for generating ultrashort electron bunches with proven ability to generate X-rays (Bagchi et al. 2011).

Liquid targets are increasingly being considered nowadays as laser plasma X-ray sources because emission can be controlled by a proper selection of the solute in solution or suspension. Moreover, liquids can be continuously circulated using a small

pump, to make them durable for long-term laser irradiation and X-ray generation. Regardless, little attention has been paid into improving the yield of hard X-rays (> 10 keV) from liquid targets (Kruer and W.L. 1988).

7.2 Experimental setup

A chirped pulse amplifier (CPA) Ti:Sapphire laser (TSA-10, Spectra-Physics) delivering pulses of 120 fs width (FWHM) at 796 nm, and a Q-switched Nd:YAG laser producing 7 ns pulses at 1064 nm, are used in the current studies for the generation of plasma plumes. A CdTe detector is used for the measurement, which has nearly 100% conversion efficiency in the energy range 10 KeV to 150 KeV. The energy of the incident photon determines the amplitude of the detector output. To reduce pile-up effects in the low energy X-ray regime, an Aluminium filter (0.5 mm) is placed in front of the detector. The detector is gated synchronously with the laser pulse to reduce background noise. The detector is kept at a distance of about 15 cm from the target, at the angle where maximum X-ray emission is detected. The cosmic ray background noise is reduced by using appropriate time gating. An unpolished Aluminium target (99.95% purity, ACI Alloys) of 5 cm \times 5 cm size and Tungsten target of 5 cm diameter (99.95% purity, Kurt J-Lesker) are used for the measurements. The laser is p polarized and is incident on the sample at an angle of 90 degrees. All spectra were collected over 5000 laser shots.

In the case of liquid target, 250 ml volume of the liquid sample (Au or Ag nanoparticle suspension) is taken in a source beaker and allowed to flow through a nozzle, providing a thin planar liquid jet (250 μ m thickness) for irradiation. The jets are irradiated normal to the surface by p-polarized 800 nm, 150 fs laser pulses obtained from a regeneratively amplified Ti:Sapphire laser (TSA-10, Spectra physics) running at 10 Hz, seeded by mode-locked pulses from a Ti:Sapphire oscillator (Tsunami, Spectra Physics). The linear optical transmission of the nanoparticle jets at 800 nm is adjusted to be about 75%, measured by using the unfocused laser beam at low energy. For the experiment the laser beam is focused to the jet using a plano-convex lens of 40 cm focal

length, giving a focal spot size of 96 microns. The volume of liquid irradiated by each laser pulse is estimated to be 2.3×10^{-3} mL. The liquid flow rate is 16 mL/min (i.e., 26.7×10^{-3} ml per 100 ms, which is the time interval between successive laser pulses). Therefore, every laser pulse irradiates a fresh sample of the liquid in the jet. The energy of the laser pulses is 5.5 mJ, which provides an intensity of 7.4×10^{14} W/cm² at the beam focus. X-rays are measured at a distance of 15 cm from the jet at an angle of 20° from the laser beam axis, which is the direction in which the emission is found to be maximum. The same X-ray detector (X-123-CdTe) is used for the measurement. The energy of the incident photon determines the amplitude of the detector output. The schematic of the experimental setup is shown in Figure 7.1.

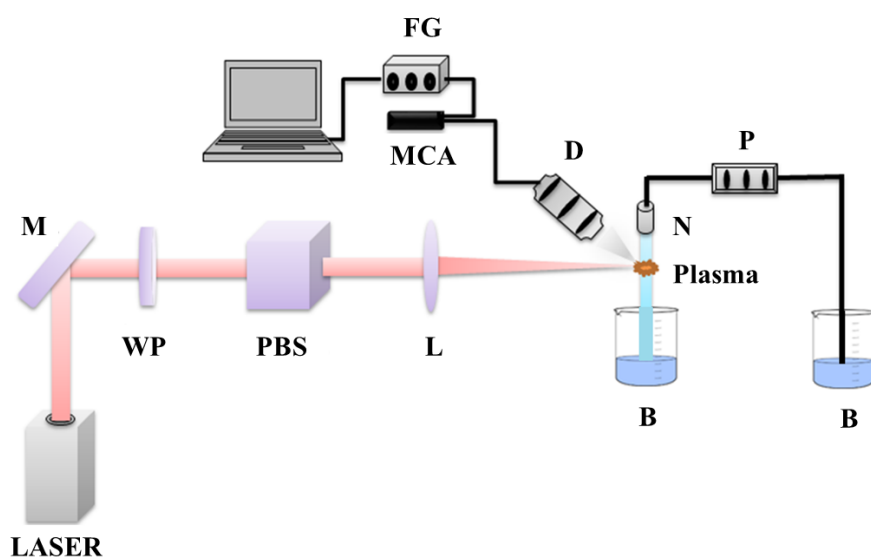


Figure 7.1: Schematic of the experimental setup for bremsstrahlung X-ray generation. A thin ($250 \mu\text{m}$) jet of metal nanoparticles suspended in water is irradiated by 800 nm, 150 fs laser pulses. Pulse energy is 5.5 mJ and pulse repetition rate is 10 Hz. M-mirror, WP - half-wave plate, PBS - polarizing beam splitter, L - lens, B - beaker, N - thin metal nozzle, P - water pump, D - CdTe X-ray detector, FG - function generator, MCA - multi-channel analyzer.

The full sample volume will flow from the source beaker to the drain beaker in a time interval of 15 minutes (9000 laser pulses). A drop of the transferred solution is dried on an ITO sheet to form a film, which is used for taking the SEM image. The irradiated solution is then transferred from the drain beaker to the source beaker, and the process

is repeated. Every 15 minutes (9000 pulses) is counted as one step of irradiation. In total nine steps of irradiation (81000 pulses, 135 minutes) were carried out.

7.3 Calibration of X-ray detector

We have measured the emission of X-rays from laser-produced plasmas using the X-123-CdTe detector. This detector is efficient in the range of 10-150 keV. Cadmium telluride (CdTe) crystals are used as the sensor material in CdTe detectors for direct conversion of the hard X-ray radiation. This high-Z semiconductor material (Cd with $Z=48$, Te with $Z=52$) delivers excellent stopping power, which results in a higher detection efficiency even at high X-ray energies.

The detector measures the X-rays in such a way that it categorizes the detected radiation peaks into different channels. The system needs to be calibrated with a known spectrum of a standard radiation source in order to assign the energy values of the peaks, which are measured in different channels of the MCA. Calibration of the detector at the start of each experiment is a necessary procedure for the authentic detection of X-ray radiation. Moreover, issues related to background noise and pile up during data collection should be eliminated for better radiation measurement.

Cosmic rays are the main cause for the background noise which is random in nature. It can be eliminated or minimized by employing time gated detection. Because plasma is a bright source of X-rays, pile-up becomes prominent during the measurement. It happens when two or more X-ray photons deposit energy in a single channel or in neighbouring channels during the measurement. In such a case these separate events are recorded as one single event having the sum of their energies, resulting in misleading observations. This problem is avoided using an aluminium filter and placing it in front of the detector in order to selectively attenuate, or block out, low-energy X-rays and to reduce the piling up of the X-ray photons.

Energy calibration of the X-ray detection system is done using radioactive sources with well-defined emission lines e.g. Am_{241} , Cs_{137} and Co_{60} . In the required range of

detection Am_{241} has two well-defined lines at 13.95 keV and 59.54 keV respectively. The efficiency curve of the detector is linear here, and hence, calibration is easily obtained. The typical spectrum used for detector calibration is given Figure 7.2. The obtained spectral peaks during the measurement are compared to this standard and the corresponding energy values are assigned to the channel numbers.

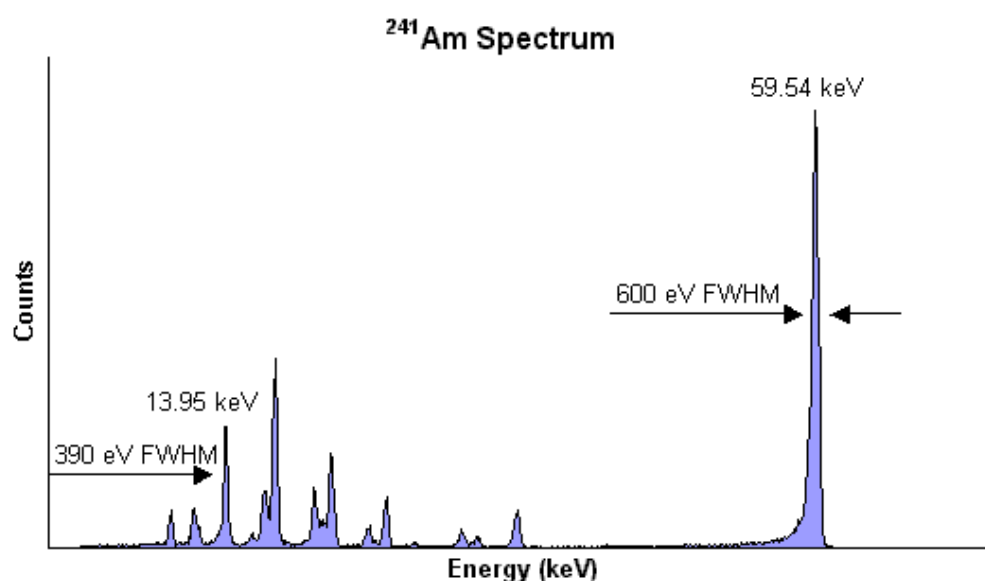


Figure 7.2: Standard radiation spectrum of Am_{241} .

The spectra obtained from the Am_{241} source using the CdTe detector is given in Figure 7.3. The spectra were obtained using the 4 mills Be window and 9 mm^2 detector area with the linear amplifier gain set to 10x. The ADC resolution is kept constant at 2048 channels, for all the measurements.

7.4 X-ray emission from solid targets

When a high intensity laser pulse ($I > 10^9 \text{ W/cm}^2$) is focused on the surface of a target, plasma will be generated which acts as source of photons (from IR to X-ray regions), electrons and ions. X-rays are emitted due to the three fundamental emission processes, i.e., free-free, free-bound and bound-bound electron transitions. Emission of a continuum due to the interaction between electrons and the Coulomb potential of ions (free-free transitions) is called bremsstrahlung radiation. Bremsstrahlung X-rays are

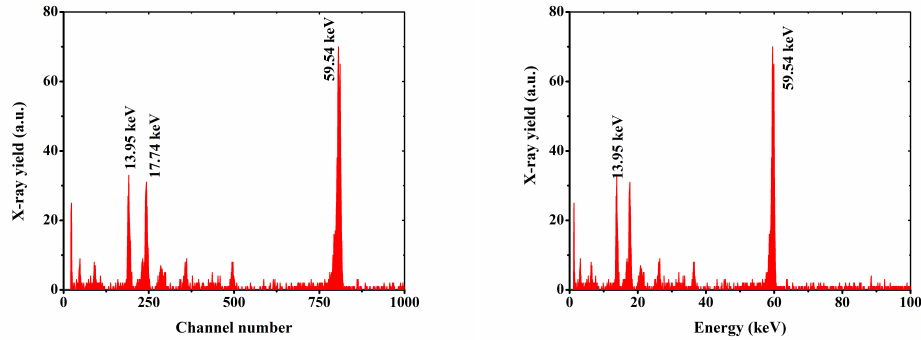


Figure 7.3: X-ray emission spectra obtained from Am_{241} with the amplifier gain set to 10x.

the signature of highly energetic hot electrons in the plasma. Emission of a continuum can happen due to the re-combination of an initial free electron state to a bound electron state as well (free-bound transitions). Bound-bound transitions produce line spectra due to transition between discrete energy levels.

In the following sections we discuss comparative observations of X-ray emission from ultrashort and short pulse laser produced plasmas from solid aluminium (Al) and tungsten (W) targets.

7.4.1 X-ray emission from Aluminium

Angle resolved measurements were done and polar diagrams were plotted for finding the directionality of X-ray emission from the irradiated targets. Because of the cylindrical symmetry of the plasma, most measurements were done only for 180 degrees on the right side of the beam, by assuming similar results for the left side. A few measurements were done on the left side also, which confirmed this assumption.

It is observed that X-rays from aluminium are emitted more in the backward direction for both ULA and SLA. This can be attributed to the reflection of the laser from the critical layer of the target. The scattering of X-rays from the target surface also contributes to the backward intensity of the X-rays. Angle of maximum X-ray emission is not the same for ULA and SLA. For ULA the maximum is observed close to 0 and 90 degrees and in SLA it is at 60 degrees, with respect to the laser propagation direction.

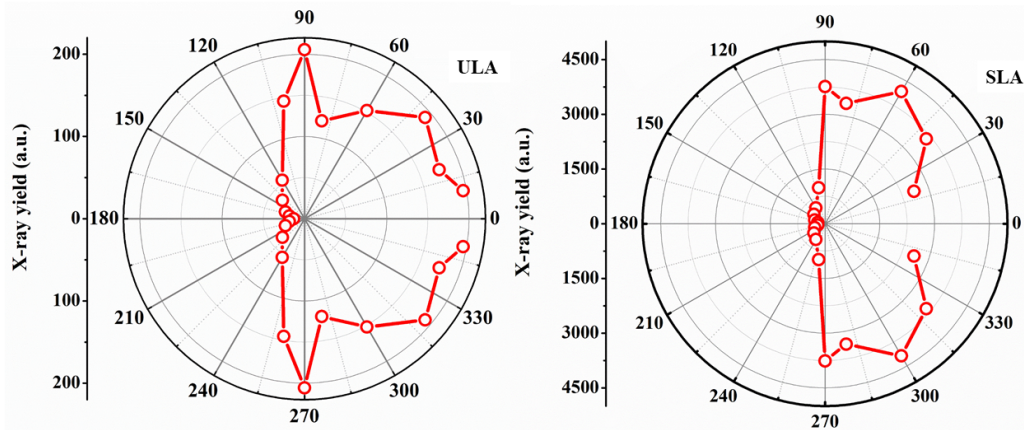


Figure 7.4: Angular distribution of X-ray emission from Aluminium (Al) target irradiated by ultrashort and short laser pulses of intensity $\approx 10^{15}$ W/cm² and 10^9 W/cm² respectively. The 0-180 axis indicates the laser propagation direction.

This difference in the maximum intensity direction is probably due to the difference in plasma plume structures and dynamics, which was discussed in the previous chapters.

Bremsstrahlung emission spectra from Aluminium recorded for ULA and SLA are shown in Figure 7.5. The net X-ray emission from laser produced plasma is a superposition of bound-bound transitions (line spectra) on a broad continuum caused by free-free and free-bound transitions. The X-ray yield depends on plasma parameters such as electron number density and temperature. When the energy of the laser is increased the coupling of the energy to the plasma will be increased, resulting in a higher yield of X-rays. In this aspect ULA and SLA behave in a similar fashion.

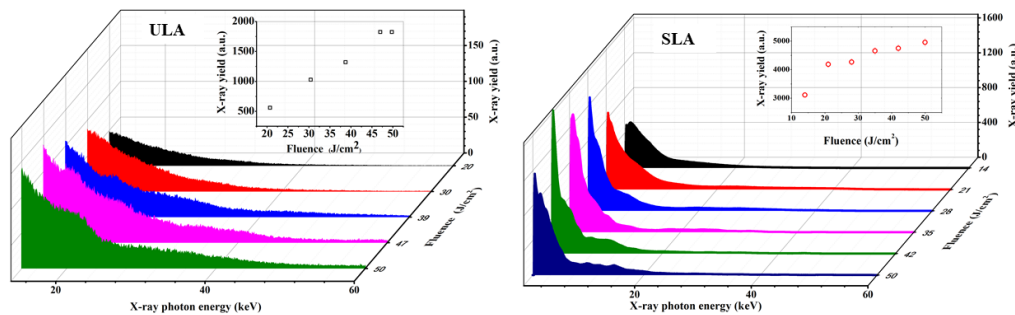


Figure 7.5: Bremsstrahlung emission from an unpolished Aluminium (Al) target kept in air irradiated with ultrashort and short laser pulses respectively.

The pulse duration and wavelength of the laser also are important for the X-ray

yield. There is one recent report on the conversion efficiency from the incident laser light energy to X-ray photons for laser produced plasma. When the laser pulse duration increases there is an increase in the X-ray yield because of ionization to higher ionized states from the lower ionized states. This process is less probable during the ultrashort laser pulse. If the pulse duration is much shorter than the time required to reach ionization equilibrium then the conversion efficiency become less, resulting in lower X-ray yields. In addition, as the hot electron temperature scales as $I\lambda^2$, the effect of wavelength (λ) on hot electron production is more prominent than that of the intensity. The use of longer wavelengths with pulse durations in the ns range leads to lower critical density LPP, which results in efficient laser-plasma heating. Hence, an improved soft X-ray emission from the plasma is achieved.

7.4.2 X-ray emission from Tungsten (W)

Figure 7.6 shows the angular distribution of X-rays measured from the LPP of a tungsten target. For ULA maximum emission is observed close to 90 degree, similar to that seen for Aluminium. In SLA maximum yield is seen in the range of 40 to 80 degrees.

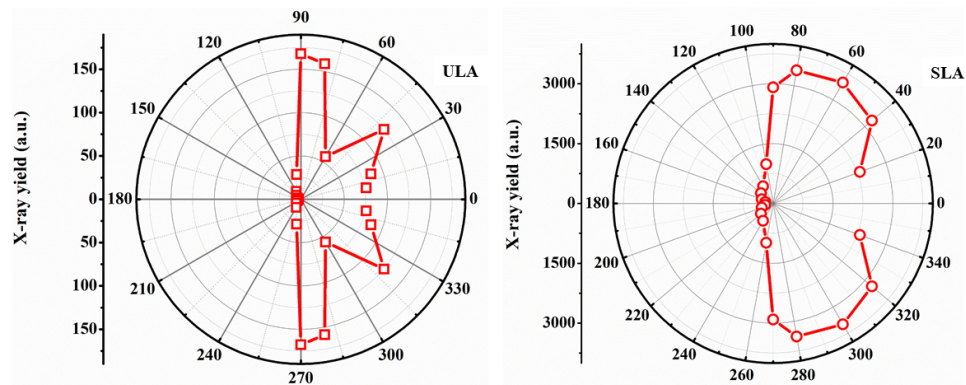


Figure 7.6: Angular distribution of X-ray emission from Tungsten (W) target irradiated by ultrashort and short laser pulses of intensity $\approx 10^{15}$ W/cm² and 10^9 W/cm² respectively. The 0-180 axis indicates the laser propagation direction.

The bremsstrahlung spectra from Tungsten (W) recorded for various input intensities in ULA and SLA are shown in Figure 7.7. The X-ray yield increases with laser energy because of enhanced laser-plasma heating. Higher yield is observed for SLA

compared to ULA, because of the higher conversion efficiency and higher ionization rate of SLA as discussed above.

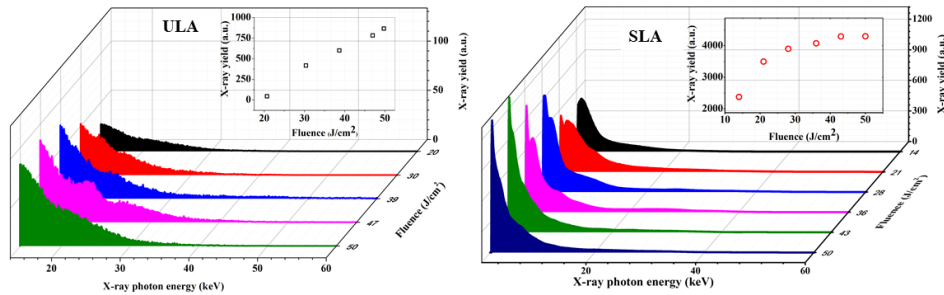


Figure 7.7: Bremsstrahlung emission from an unpolished Tungsten (W) target kept in air irradiated with ultrashort and short laser pulses respectively.

7.5 X-ray emission from liquid targets

7.5.1 X-ray emission from a water jet

Angle resolved X-ray emission measured from ULA of a thin water jet is shown in Figure 7.8a. Emission is stronger in the backward direction, with maximum observed at 60 degrees from the laser propagation direction. Emission spectrum measured at the angle of 30° is shown in Figure 7.8b.

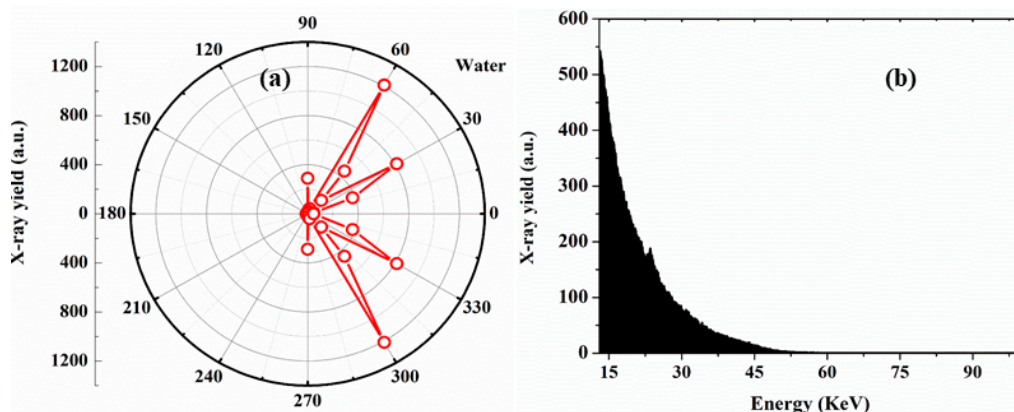


Figure 7.8: X-ray emission from a planar water jet irradiated by ultrashort laser pulses at an intensity of 10^{15} W/cm². (a) angular distribution of emission, (b) emission spectrum obtained for the detection angle of 30°.

7.5.2 X-ray emission from silver and gold nanoparticle colloidal jets

7.5.2.1 Materials and characterization

Silver nanoparticles were synthesized by employing sodium borohydride (NaBH_4) as reductant (Zieliska et al. 2009). A typical procedure is as follows. Required volumes of freshly prepared aqueous solutions containing AgNO_3 and trisodium citrate (TSC) are mixed and heated to 60°C for 30 minutes in the dark with vigorous stirring to ensure a homogenous solution. At the end of 30 minutes the required volume of NaBH_4 solution is added drop-wise to the mixture, and subsequently, the temperature is further raised to 90°C . Heating is continued for 5 minutes, until a change of colour is evident. The nanoparticle suspension is allowed to cool at room temperature and is finally stored at 4°C for future use. The concentration of the nanoparticles is estimated to be $2.45 \times 10^{15} \text{ cm}^{-3}$. In this method sodium borohydride (NaBH_4) is used for reducing Ag atoms which would form the nanoparticle nuclei. Overall the process is similar to reduction using citrate but sodium borohydride provides better monodispersity for the final particle population because NaBH_4 is a stronger reducing agent compared to citrate.

Au nanoparticles were prepared by the Turkevich Method (Turkevich 1951), as outlined by Hsu et al. (2018). In this method, Au nanoparticles are produced in a liquid by the reduction of hydrogen tetrachloroaurate (III) trihydrate ($\text{H}[\text{AuCl}_4]$). After dissolving $\text{H}[\text{AuCl}_4]$ the solution is heated to boiling and rapidly stirred while the reducing agent (sodium citrate) is added. This causes Au^{3+} ions to be reduced to Au^+ ions. Then a disproportionation reaction occurs whereby 3Au^+ ions give rise to Au^{3+} and 2Au^0 atoms. The Au^0 atoms act as centres of nucleation around which further Au^+ ions get reduced. To prevent the particles from aggregating, a stabilizing agent that sticks to the nanoparticle surface is required. Here, citrate initially acts as the reducing agent and finally as the capping agent, which stabilizes the Au nanoparticles through electrostatic interactions between the lone pair of electrons on the oxygen and the metal surface. The concentration of the nanoparticles is estimated to be $1.43 \times 10^{16} \text{ cm}^{-3}$.

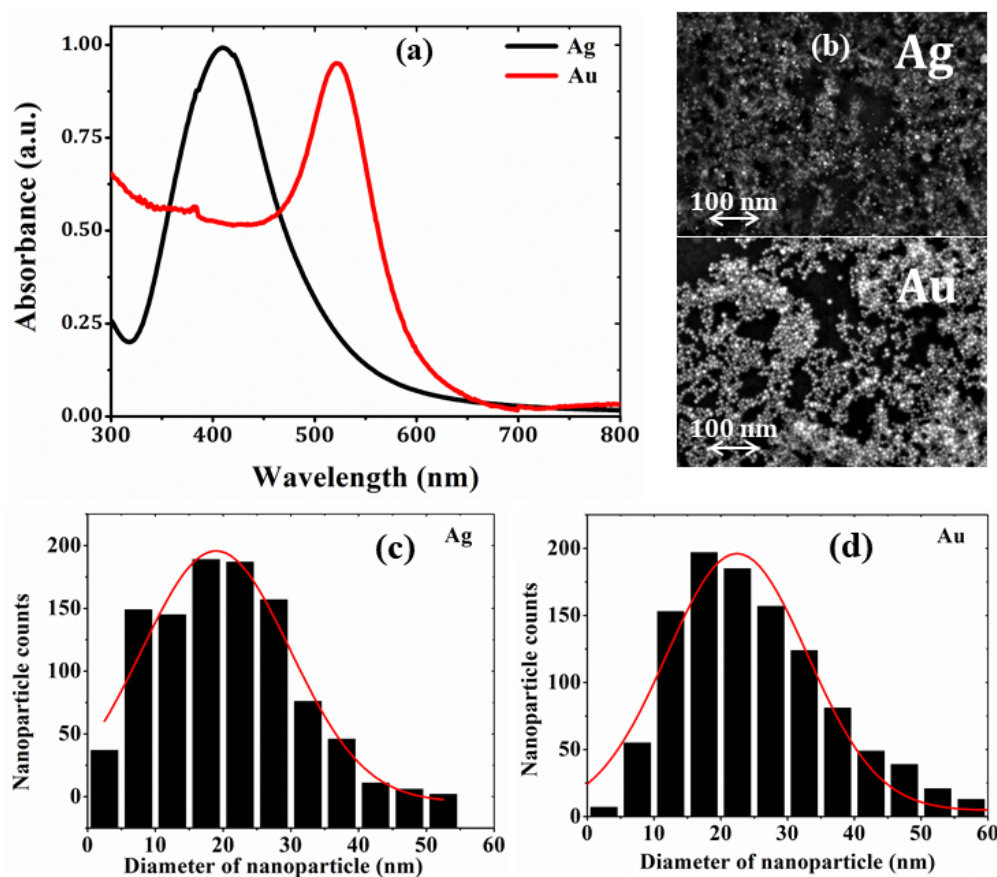


Figure 7.9: (a) Absorption spectra of Ag and Au nanoparticle suspensions showing LSPR bands; (b) SEM images of as prepared Ag and Au nanoparticles; (c) and (d) size distribution histograms for Ag and Au nanoparticles calculated from SEM images.

Linear absorption spectra of the prepared nanoparticle solutions (measured using an Agilent Cary 5000 double-beam spectrophotometer with a resolution of 2 nm) are shown in Figure 7.9a. For measuring these spectra the samples were taken in 5 mm pathlength cuvettes. Absorption bands arising from LSPR can be seen in the region of 380 - 480 nm for Ag nanoparticles, and 520 - 600 nm for Au nanoparticles. From SEM images taken using thin films of the solutions on ITO sheets (Figure 7.9b) it can be seen that the as prepared nanoparticles are not aggregated in solution. Size distribution histograms for the nanoparticles are shown in figures 7.9c and 7.9d. Sizes of the nanoparticles were calculated from SEM images using ImageJ software. The mean size of Ag and Au nanoparticles are found to be 20 ± 2 nm and 21 ± 3 nm respectively.

7.5.2.2 Stability studies of Au and Ag under laser irradiation

Figure 7.10a shows the effect of laser irradiation on the linear absorption spectrum of Ag nanoparticles. The height of the LSPR band (which peaks at 410 nm) gets reduced indicating that the nanoparticle concentration is decreasing with laser irradiation. The concomitant rise of the long-wavelength wing is more obvious from Figure 7.10b, in which the spectra are redrawn with all peak absorbances normalized to unity. The short-wavelength side also gets enhanced. This clearly indicates laser-induced aggregation of Ag nanoparticles (Turkevich 1985). Figure 7.10c gives SEM images showing morphology changes.

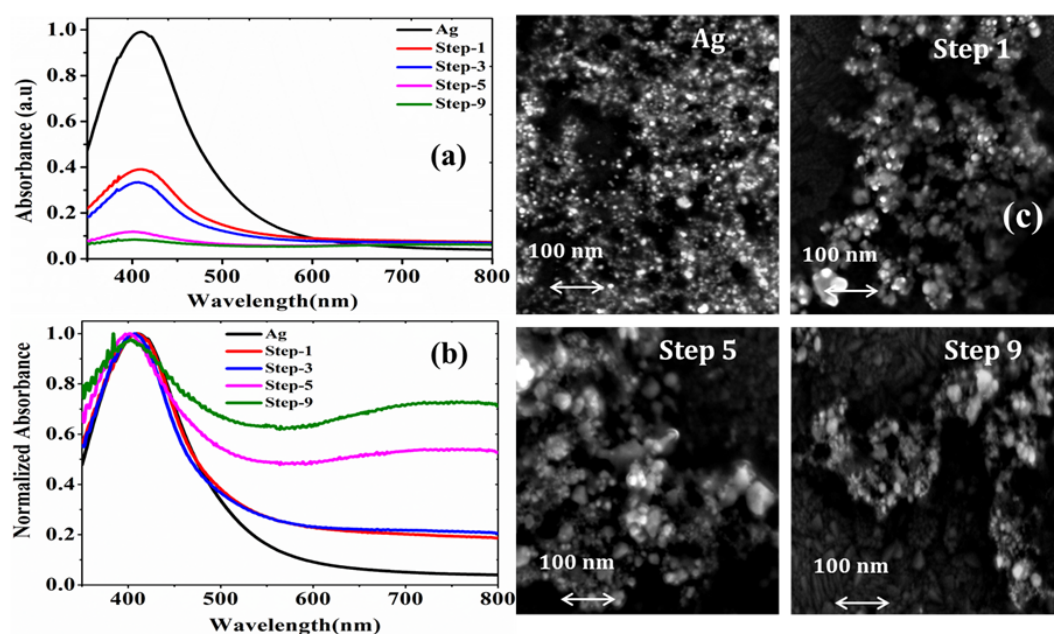


Figure 7.10: (a) Linear absorption spectra of Ag nanoparticle suspension measured after successive steps of laser irradiation (each step is 9000 laser shots), (b) absorption spectra drawn with the peak absorbances normalized to unity, (c) SEM images showing morphology changes.

Figures 7.11(a) to 7.11(c) show corresponding results obtained for Au nanoparticles. Here, the height of the LSPR band (which peaks at 520 nm) is noticeably reduced during the first step of irradiation itself, but thereafter the reduction is minimal. Broadening of the spectra with irradiation indicate agglomeration, but it is not as pronounced as in the case of Ag nanoparticles. This observation mean that Au nanoparticles are more photostable compared to Ag nanoparticles.

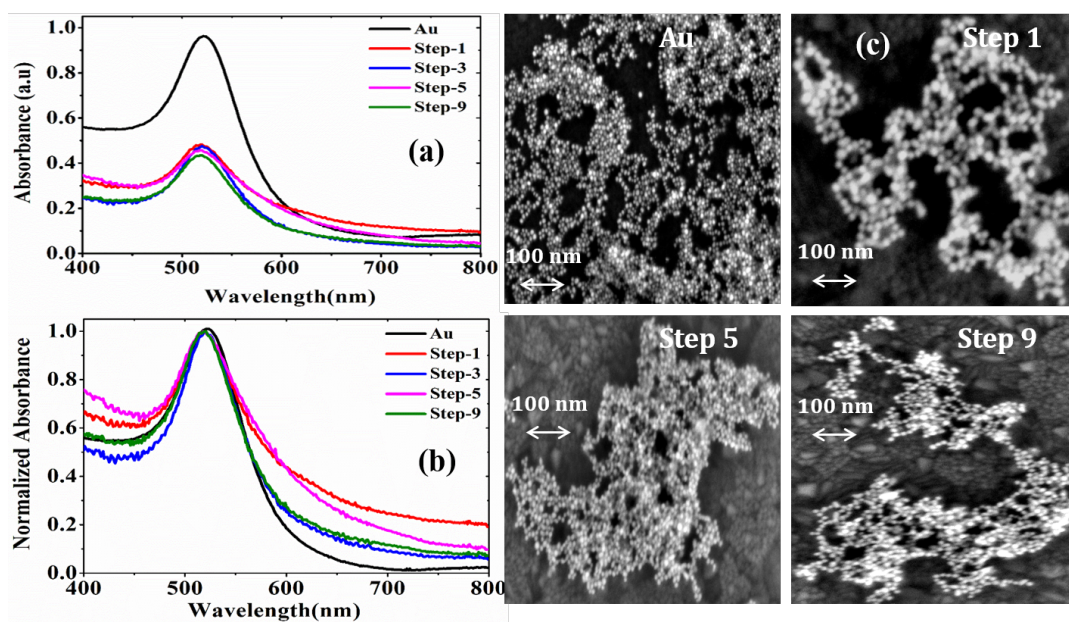


Figure 7.11: (a) Absorption spectra of Au nanoparticle suspension measured after successive steps of laser irradiation (each step is 9000 laser shots), (b) absorption spectra drawn with the absorbances normalized to unity, (c) corresponding SEM images showing morphology changes.

SEM images shown in Figures 7.11c reveal morphology changes due to laser irradiation. For every laser pulse the nanoparticles will absorb a large number of photons, and their temperature will rise significantly, leading to fragmentation. The smaller nanoparticles produced by fragmentation might get further pulverized by multiphoton absorption (Mafune et al. 2001). The heat diffuses into the surrounding medium within picoseconds to nanoseconds, and the temperature of the nanoparticles is lowered, until the arrival of the following pulse. While the fragmentation process occurs for each laser pulse, the fragments will aggregate back into small clusters within nanoseconds, in the interim period between the pulses (at 10 Hz repetition rate the time interval between successive laser pulses is quite long at 100 ms). The aggregation rate increases with the concentration of the fragments (Mafune et al. 2001). Notwithstanding the fact that Ag nanoparticles are less photostable compared to Au nanoparticles, it may be noted that the LSPR peak in Ag is in better resonance for two-photon absorption at the excitation wavelength of 800 nm compared to the LSPR peak of Au. Hence a larger number of Ag nanoparticles are likely to get fragmented and subsequently aggregated during each irradiation step. Broadening of the LSPR wing region indicates moderate aggregation

leading to the formation of larger clusters (Link et al. 1999).

7.5.2.3 X-ray emission from Au and Ag nanoparticles

Figure 5 shows the energy spectrum of bremsstrahlung X-ray emission measured in the 15 - 100 keV region. Compared to Au nanoparticles, peak X-ray emission is brighter by a factor of two for Ag nanoparticles. Similar measurements were carried out in DI water, and also in the precursor salt solutions: silver nitrate (AgNO_3), trisodium citrate and DI water for Ag nanoparticles, and hydrochloroauric acid, citric acid and DI water for Au nanoparticles. Emission from the nanoparticle suspensions were found to be considerably higher compared to that from their precursor solutions, confirming that the nanoparticles are indeed responsible for the observed enhancement.

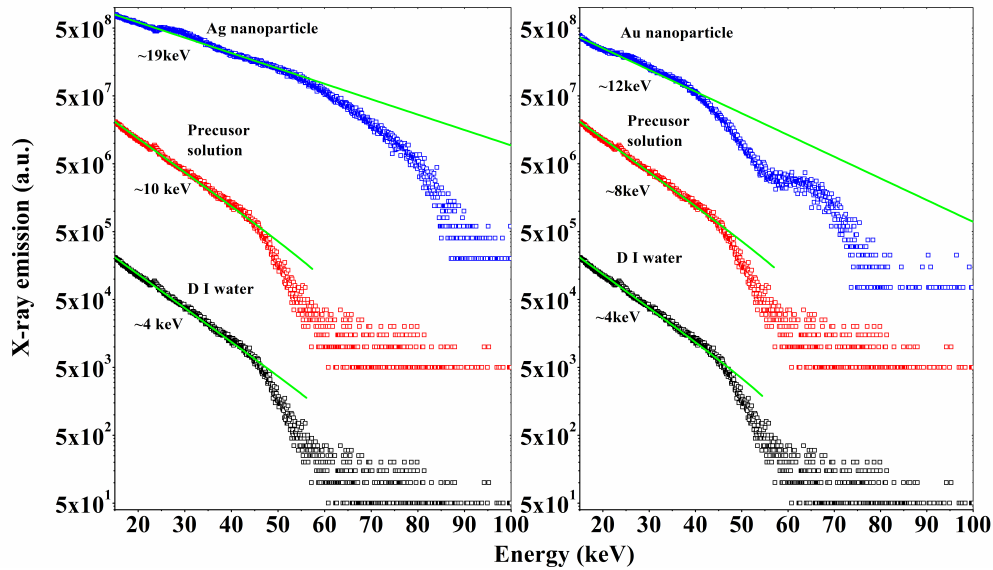


Figure 7.12: Energy spectrum of bremsstrahlung X-ray emission measured in Ag and Au nanoparticle suspensions and their precursor solutions for a laser pulse intensity of $7.4 \times 10^{14} \text{ W/cm}^2$. Total counts measured for the first 9000 laser pulses (step 1) are shown. Solid curves are numerical fits obtained using Eqn. 7.2.

To explain these experimental results, first we note that the enhanced local electric field (E_1) associated with the LSPR is given by (Reza et al. 2012)

$$E_1 = \frac{3\epsilon_d}{\epsilon_m + 2\epsilon_d} E_0 \quad (7.1)$$

where E_0 is the applied electric field (7.2×10^{10} V/m). ϵ_m and ϵ_d are the dielectric constants of the metal nanoparticle and the surrounding medium respectively, for 800 nm wavelength. The local electric fields calculated for Ag and Au nanoparticles are 1.22×10^{11} V/m and 1.16×10^{11} V/m respectively. The local field is thus one order of magnitude higher than the applied electric field, which causes a substantial increase in the MPI efficiency. Silver nanoparticles experience a slightly higher local field, generating relatively more number of hot electrons. Moreover, the ionization potentials of Ag and Au are 7.58 eV and 9.22 eV respectively, so that with 800 nm (1.55 eV) excitation, MPI of Ag is a 5-photon process while that of Au is a 6-photon process. Between these the 5-photon process will be relatively stronger, again resulting in a larger number of hot electrons for Ag.

Secondly, the photon energy (E) distribution of bremsstrahlung from hot electrons is given by (Rajeev et al. 2004)

$$N(E) \propto \frac{1}{T_e^{\frac{1}{2}}} \exp\left(\frac{-E}{kT_e}\right) \quad (7.2)$$

where T_e is the hot electron temperature and k is the Boltzmann constant. Therefore, T_e can be obtained by fitting this function to the measured energy-resolved bremsstrahlung spectrum. Since $T_e^{\frac{1}{2}}$ is relatively slowly varying in comparison to the exponential term, a simple exponential fit to the experimental data is usually sufficient. The hot electron temperatures obtained for DI water, precursor salts of Ag nanoparticles ($\text{AgNO}_3 + \text{Na}_3\text{C}_6\text{H}_5\text{O}_7 + \text{DI water}$), and precursor salts of Au nanoparticles ($\text{HAuCl}_4 + \text{C}_6\text{H}_8\text{O}_7 + \text{DI water}$), are 4 ± 0.07 keV, 10 ± 0.04 keV, and 8 ± 0.06 keV, respectively. Obviously, Ag and Au nanoparticles have higher electron temperatures compared to their precursors.

Finally, Figure 6 depicts the scaling of hot electron temperature with laser intensity, given by (Forslund et al. 1977; Anand et al. 2007)

$$T_e = 14T_c(I\lambda^2)^\alpha \quad (7.3)$$

where $I\lambda^2$ is the intensity in units of $10^{15} \text{ Wcm}^{-2}\mu\text{m}^2$ and T_c is the bulk plasma temperature (both T_c and T_e are given in keV). By taking T_c as 0.1 keV and substituting for the other quantities it turns out that $\alpha = 1/3$, which indicates that the hot electrons are generated by a resonance absorption mechanism (Cui et al. 2013). In resonance absorption the p-polarized electromagnetic wave will resonantly excite electron oscillations in the plasma, the magnitude of which will grow until the oscillations are limited by collisional or collision-less damping processes. The longitudinal electric field component (E_z) plays a key role in electron heating leading to the generation of hot electrons, resulting in X-ray emission from the plasma (Palastro et al. 2018; Hsu et al. 2016).

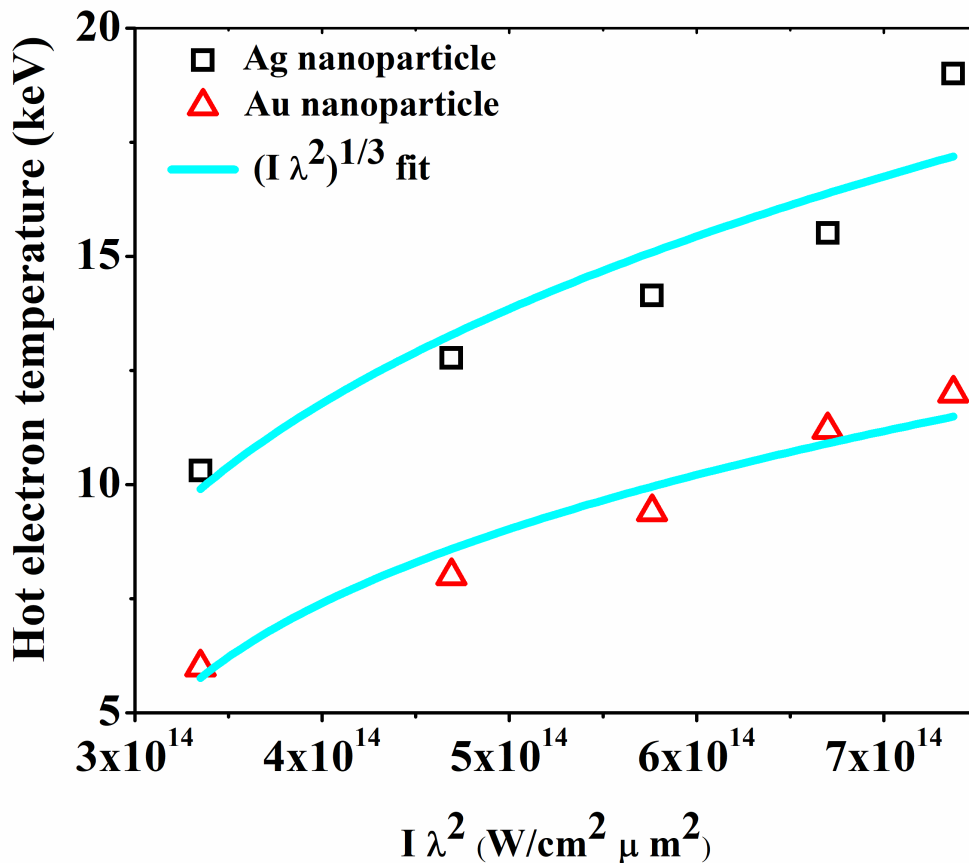


Figure 7.13: Hot electron temperature versus $I\lambda^2$ for the generated plasmas. Solid curves are numerical fits to the data using Equation 7.3

7.6 Summary

A comparative study of X-ray emission from ultrashort and short pulse laser produced plasmas is described in this chapter. Two solid targets, namely Aluminium (Al) and Tungsten (W), and two liquid targets, namely Ag and Au nanoparticle suspensions, have been used for the studies. The pulse duration of the laser is found to be a critical factor that determines features of X-ray emission from the plasma. It is shown that X-ray emission depends also on the temperature and number density of the plasma, as well as on the ionization dynamics. Bremsstrahlung X-ray emission from ULA of flowing thin jets of aqueous Ag and Au nanocolloidal suspensions show 30-fold and 18-fold enhancements in X-ray yield when compared to the precursor salt solutions. The relatively higher emission from Ag nanoparticles is attributed to the lower ionization potential and the higher local electric field, which are favourable for enhanced multi-photon ionization. While Ag nanoparticles exhibit a higher X-ray yield compared to Au nanoparticles, photostability is found to be better for the latter. These results show that liquid jets of noble metal nanoparticles are potential candidates for designing efficient and durable ultrafast laser plasma X-ray sources.

CHAPTER 8

CONCLUSIONS AND FUTURE SCOPE

In this chapter we summarize the main results of the investigations presented in this thesis. Future work also is suggested.

Everything should be made as simple as possible,

But not simpler

————— *Albert Einstein*

The overwhelming interest in the field of high power laser-matter interaction prompted many researchers around the world to carry out fundamental studies in this area. Technological applications such as high harmonic generation, laser-plasma accelerators, ion and X-ray sources and EUV lithography are still in the developing phase. A large body of careful experimentation is still required for a realistic understanding of laser-produced plasmas and their potential applications.

In this thesis we have reported a detailed comparative investigation of plasmas produced from solid targets using ultrashort (100 fs) and short (7 ns) laser pulses. Two prominent aspects are studied: 1) Spatial and temporal evolution of the laser produced plasma under a broad range of ambient pressures, and 2) X-ray emission from the plasma. Essentially, the work presented in this thesis forms a systematic and detailed investigation of the spatio-temporal behaviour of the generated plasma.

Plasmas were generated by irradiating solid aluminium (*Al*) and tungsten (*W*) targets by ultrashort (100 fs) and short (7 ns) laser pulses, and the hydrodynamic expansion of the resulting plasma plumes into the surrounding gas was investigated. Coulomb explosion is prominent in ULA because of the high optical intensity of the laser pulse while thermal ablation and laser-plasma interaction are prevalent in SLA. The experimental techniques of OES, time-resolved ICCD imaging, OTOF and ion current measurements were employed. Maximum optical emission intensity from the plasma was found to occur in the pressure range of 1-10 Torr because of the optimal balance between the competing processes of ionization, recombination and thermal leak. The emission intensity is one order higher for SLA because of laser-plasma interaction. While ions are relatively scarce in ULA, both neutrals and ions are equally abundant in SLA for both the targets. OTOF measurements show distinct fast and slow species of

neutrals and ions in SLA for aluminium, while the distinction is not quite obvious in ULA. The fast neutrals observed in SLA are formed by the recombination of fast ions with electrons. At low pressures the plume expands freely but at higher pressures the expanding plume decelerates quickly due to plume confinement, which is confirmed from ICCD imaging of the ULA and SLA plumes. Ion TOF studies reveal the presence of both fast and slow ions in SLA of tungsten while only the fast species is seen in ULA. Ions with higher average velocities are found for SLA, in agreement with the R-t plots drawn from the ICCD images. SEM images of the irradiated tungsten surface indicate the formation of cracks in ULA because of the relatively faster transient temperature increase.

A comparative study of the dynamics of the ionic species in ULA and SLA plasmas for different background pressures was carried out. From time integrated and time-resolved ICCD imaging, spatial and temporal evolution of the whole plasma plume, as well as that of its ionic component, were investigated. The plumes have velocities of 34 km/s and 27 km/s for ULA and SLA respectively. The ions present in the ULA and SLA plume front expand with velocities of 45 km/s and 32 km/s respectively. However, as the pressure increases there is a decrease in speed due to energy exchange between the ions and the ambient gas. The deceleration of the ejected species with increasing ambient pressure was analyzed within the framework of shock wave and drag force models. The expansion fits a shock wave model for higher ambient pressures. When pressure increases to 760 Torr the velocity reduces sufficiently to be fitted by the drag model in both ULA and SLA. However, the ionic component that moves in the plume front behaves differently and contributes much to the snowplough effect, which in turn leads to a shock wave behaviour up to the highest ambient pressures studied.

We also investigated the effect of laser beam size on LPP. OES studies showed that smaller beam sizes produced higher emission intensities and ion populations. While larger beam sizes resulted in cylindrical plumes, smaller beam sizes resulted in spherical plumes. Ion flux and velocities were higher for smaller beam sizes compared to larger beam sizes.

X-ray emission from ULA and SLA plasmas was studied to investigate conditions for high conversion efficiency of laser energy into X-ray radiation, which has several applications. Both Al and W targets were irradiated with ultrashort and short laser pulses to produce X-rays efficiently. It was found that X-ray emission depends on plasma parameters like temperature, number density and ionization dynamics. In addition, the excitation wavelength and pulse duration of the laser also contributed to X-ray emission from the plasma. Bremsstrahlung X-ray emission from flowing thin jets of aqueous Ag and Au nanoparticle suspensions also was investigated. When compared to the precursor salt solutions, 30-fold and 18-fold enhancements in the X-ray yield were observed for the Ag and Au nano-colloidal suspensions respectively. The relatively higher emission from Ag nanoparticles is attributed to the lower ionization potential and the higher local electric field, which are favourable for enhanced multiphoton ionization. While Ag nanoparticles exhibited a higher X-ray yield compared to Au nanoparticles, photostability was found to be better for the latter.

Comparative studies of ULA and SLA offer opportunities for a deeper understanding of the fascinating fundamental mechanisms, and provide a window to the potential applications of LPPs. Utilizing the ultrashort laser we can achieve conditions for generating short pulse laser plasmas via the double-pulse excitation method. The advantages of both ULA and SLA can be combined by this technique. Therefore, further optimization of ion and X-ray sources from double-pulse plasmas will be the focus of our work in the near future.

REFERENCES

- Albert, O., Roger, S., Glinec, Y., Loulergue, J. C., Etchepare, J., Boulmer Leborgne, C., & Millon, E. (2003). Time-resolved spectroscopy measurements of a titanium plasma induced by nanosecond and femtosecond lasers. *Applied Physics A: Materials Science & Processing*, 76, 319-323.
- Anand, M., Gibbon, P., & Krishnamurthy, M. (2007). Hot electrons produced from long scale-length laser-produced droplet plasmas. *Laser Physics*, 17(4), 408-414.
- Ancona, A., Dring, S., Jauregui, C., Rser, F., Limpert, J., Nolte, S., & Tnnermann, A. (2009). Femtosecond and picosecond laser drilling of metals at high repetition rates and average powers. *Optics letters*, 34(21), 3304-3306.
- Anisimov, S. I., & Luk'yanchuk, B. S. (2002). Selected problems of laser ablation theory. *Physics-Uspekhi*, 45, 293-324.
- Anisimov, S. I., Kapeliovich, B. L., & Perelman, T. L. (1974). Electron emission from metal surfaces exposed to ultrashort laser pulses. *Journal of Experimental and Theoretical Physics*, 39, 375-377.
- Aragn, C., & Aguilera, J. A. (2008). Characterization of laser induced plasmas by optical emission spectroscopy: A review of experiments and methods. *Spectrochimica Acta Part B: Atomic Spectroscopy*, 63(9), 893-916.
- Bagchi, S., Kiran, P. P., Yang, K., Rao, A. M., Bhuyan, M. K., Krishnamurthy, M., & Kumar, G. R. (2011). Bright, low debris, ultrashort hard x-ray table top source using carbon nanotubes. *Physics of Plasmas*, 18(1), 0-4.
- Beigman, I., Pospieszczyk, A., Sergienko, G., Tolstikhina, I. Y., & Vainshtein, L. (2007). Tungsten spectroscopy for the measurement of W-fluxes from plasma facing components. *Plasma Physics and Controlled Fusion*, 49(11), 18331847.

References

- Biedermann, C., Radtke, R., Seidel, R., & Ptterich, T. (2009). Spectroscopy of highly charged tungsten ions relevant to fusion plasmas. *Physica Scripta*, 2009(T134), 014026.
- Black, S. E. (2011). *Laser ablation: effects and applications*. Nova Science Publ.
- Bloembergen, N. (1974). Laser-induced electric breakdown in solids. *IEEE Journal of Quantum Electronics*, 10, 37-386.
- Brabec, T., & Krausz, F. (2000). Intense few-cycle laser fields: Frontiers of nonlinear optics. *Reviews of Modern Physics*, 72, 545591.
- Breech, F., & Cross, L. (1962). Optical microemission stimulated by a ruby maser. *Appl. Spectrosc*, 16, 1.
- Bulgakova, N. M., & Bulgakov, A. V. (2001). Pulsed laser ablation of solids: transition from normal vaporization to phase explosion. *Applied Physics A Materials Science & Processing*, 73, 199-208.
- Buzi, L., De Temmerman, G., Huisman, A. E., Bardin, S., Morgan, T. W., Rasinski, M., ... & Van Oost, G. (2017). Response of tungsten surfaces to helium and hydrogen plasma exposure under ITER relevant steady state and repetitive transient conditions. *Nuclear Fusion*, 57(12), 126009.
- Byskov-Nielsen, J., Savolainen, J. M., Christensen, M. S., & Balling, P. (2010). Ultra-short pulse laser ablation of metals: Threshold fluence, incubation coefficient and ablation rates. *Applied Physics A: Materials Science and Processing*, 101(1), 97-101.
- Campbell, J. D., Yu, M. H., Mangir, M., & Wittig, C. (1978). Optical time of flight spectroscopy: A method for the direct state selective measurement of photofragment recoil energies. *The Journal of Chemical Physics*, 69(8), 3854-3857.
- Chao, W., Harteneck, B. D., Liddle, J. A., Anderson, E. H., & Attwood, D. T. (2005). Soft X-ray microscopy at a spatial resolution better than 15nm. *Nature*, 435(7046), 1210-1213.

- Chen, L., Kando, M., Xu, M. H., Li, Y. T., Koga, J., Chen, M., & Bulanov, S. V. (2008). Study of X-ray emission enhancement via a high-contrast femtosecond laser interacting with a solid foil. *Physical Review Letters*, 100(4), 045004.
- Chichkov, B. N., Momma, C., Nolte, S., Alvensleben, F., & Tnnermann, A. (1996). Femtosecond, picosecond and nanosecond laser ablation of solids. *Applied Physics A Materials Science & Processing*, 63, 109-115.
- Choi, T. Y., & Grigoropoulos, C. P. (2002). Plasma and ablation dynamics in ultrafast laser processing of crystalline silicon. *Journal of Applied Physics*, 92, 4918-4925.
- Corkum, P. B. (1993). Plasma perspective on strong field multiphoton ionization. *Physical Review Letters*, 71, 1994-1997.
- Cristoforetti, G., De Giacomo, A., Dell'Aglio, M., Legnaioli, S., Tognoni, E., Palleschi, V., & Omenetto, N. (2010). Local Thermodynamic Equilibrium in Laser-Induced Breakdown Spectroscopy: Beyond the McWhirter criterion. *Spectrochimica Acta Part B: Atomic Spectroscopy*, 65(1), 86-95.
- Cui, Y. Q., Wang, W. M., Sheng, Z. M., Li, Y. T., & Zhang, J. (2013). Laser absorption and hot electron temperature scalings in laserplasma interactions. *Plasma Physics and Controlled Fusion*, 55(8), 085008.
- Cveji, M. (2014). Diagnostics of laser-induced plasma by optical emission spectroscopy. *Journal of Physics: Conference Series*, 565(1), 0-10.
- Dawood, M. S., Hamdan, A., & Margot, J. (2015). Influence of surrounding gas, composition and pressure on plasma plume dynamics of nanosecond pulsed laser-induced aluminum plasmas. *AIP Advances*, 5(10), 107143.
- Dawson, J. M. (1964). On the Production of Plasma by Giant Pulse Lasers. *Physics of Fluids*, 7, 981.
- De Giacomo, A., Dell'Aglio, M., Santagata, A., & Teghil, R. (2005). Early stage emission spectroscopy study of metallic titanium plasma induced in air by femtosec-

References

- ond and nanosecond-laser pulses. *Spectrochimica Acta Part B: Atomic Spectroscopy*, 60, 935-947.
- Eesley, G. L. (1983). Observation of Nonequilibrium Electron Heating in Copper. *Physical Review Letters*, 51, 2140-2143.
- Eesley, G. L. (1986). Generation of nonequilibrium electron and lattice temperatures in copper by picosecond laser pulses. *Physical Review B*, 33, 2144-2151.
- Effenberger, A., & Scott, J. (2010). Effect of Atmospheric Conditions on LIBS Spectra. *Sensors*, 10(5), 4907-4925.
- Elhassan, A., Giakoumaki, A., Anglos, D., Ingo, G. M., Robbiola, L., & Harith, M. A. (2008). Nanosecond and femtosecond Laser Induced Breakdown Spectroscopic analysis of bronze alloys. *Spectrochimica Acta Part B: Atomic Spectroscopy*, 63, 504-511.
- Elsied, A. M., Termini, N. C., Diwakar, P. K., & Hassanein, A. (2016). Characteristics of Ions Emission from Ultrashort Laser Produced Plasma. *Scientific Reports*, 6(December), 1-10.
- Elton, R. C. (1990). *X-ray lasers*. Academic Press.
- Fabbro, R., Fabre, E., Amiranoff, F., Garban-Labaune, C., Virmont, J., Weinfeld, M., & Max, C. E. (1982). Laser-wavelength dependence of mass-ablation rate and heat-flux inhibition in laser-produced plasmas. *Physical Review A*, 26, 2289-2292.
- Farid, N., Li, C., Wang, H., & Ding, H. (2013). Laser-induced breakdown spectroscopic characterization of tungsten plasma using the first, second, and third harmonics of an Nd: YAG laser. *Journal of Nuclear Materials*, 433(1-3), 80-85.
- Forslund, D. W., Kindel, J. M., & Lee, K. (1977). Theory of Hot-Electron Spectra at High Laser Intensity. *Physical Review Letters*, 39(5), 284-288.
- Freeman, J. R., Harilal, S. S., Diwakar, P. K., Verhoff, B., & Hassanein, A. (2013). Comparison of optical emission from nanosecond and femtosecond laser pro-

- duced plasma in atmosphere and vacuum conditions. *Spectrochimica Acta Part B: Atomic Spectroscopy*, 87, 43-50.
- Fritzler, S., Malka, V., Grillon, G., Rousseau, J. P., Burgy, F., Lefebvre, E., DHumires, E., et al. (2003). Proton beams generated with high-intensity lasers: Applications to medical isotope production. *Applied Physics Letters*, 83(15), 3039-3041.
- Gamaly, E. G., Rode, A. V., Luther-Davies, B., & Tikhonchuk, V. T. (2002). Ablation of solids by femtosecond lasers: Ablation mechanism and ablation thresholds for metals and dielectrics. *Physics of Plasmas*, 9, 949-957.
- Geohegan, D. B., & Puretzky, A. A. (1996). Laser ablation plume thermalization dynamics in background gases: combined imaging, optical absorption and emission spectroscopy, and ion probe measurements. *Applied Surface Science*, 96-98, 131-138.
- George, S., Kumar, A., Singh, R. K., & Nampoore, V. P. N. (2009). Fast imaging of laser-blow-off plume: Lateral confinement in ambient environment. *Applied Physics Letters*, 94(14), 2009-2011.
- Ginzburg, V. L. (1961). *Propagation of Electromagnetic Waves in Plasma Gordon and Breach*. New York.
- Giulietti, D., & Gizzi, L. A. (1998). X-ray emission from laser-produced plasmas. *La Rivista Del Nuovo Cimento*, 21, 1-93.
- Gontier, Y., Poirier, M., & Trahin, M. (1980). Multiphoton absorptions above the ionisation threshold. *Journal of Physics B: Atomic and Molecular Physics*, 13, 1381-1387.
- Gonzalo, J., Vega, F., & Afonso, C. N. (1995). Plasma expansion dynamics in reactive and inert atmospheres during laser ablation of Bi(2)Sr(2)Ca(1)Cu(2)O(7-y). *Journal of Applied Physics*, 77(12), 6588-6593.

References

- Gordon, S. P., Donnelly, T., Sullivan, a, Hamster, H., & Falcone, R. W. (1994). X rays from microstructured targets heated by femtosecond lasers. *Optics Letters*, 19(7), 484-486.
- Griem, H. R. (1963). Validity of Local Thermal Equilibrium in Plasma Spectroscopy. *Physical Review B* , 131(3), 1170-1176.
- Griem, H. R. (1974). *Spectral line broadening by plasmas*. Academic Press.
- Han, J., & Li, Y. (2011). Interaction Between Pulsed Laser and Materials. *Lasers-Applications in Science and Industry*, 109-131.
- Hans R Griem. (1964). *Plasma Spectroscopy*. Mc Graw Hill New York.
- Harilal, S. S., Bindhu, C. V, Tillack, M. S., Najmabadi, F., & Gaeris, A. C. (2002). Plume splitting and sharpening in laser-produced aluminium plasma. *Journal of Physics D: Applied Physics*, 35(22), 2935-2938.
- Harilal, S. S., Bindhu, C. V., Issac, R. C., Nampoori, V. P. N., & Vallabhan, C. P. G. (1997). Electron density and temperature measurements in a laser produced carbon plasma. *Journal of Applied Physics*, 82(5), 2140-2146.
- Harilal, S. S., Bindhu, C. V., Tillack, M. S., Najmabadi, F., & Gaeris, A. C. (2003). Internal structure and expansion dynamics of laser ablation plumes into ambient gases. *journal of Applied Physics*, 93(5), 2380-2388.
- Harilal, S. S., Farid, N., Hassanein, A., & Kozhevin, V. M. (2013). Dynamics of femtosecond laser produced tungsten nanoparticle plumes. *Journal of Applied Physics*, 114(20), 203302.
- Harmon, R. S., Russo, R. E., & Hark, R. R. (2013). Applications of laser-induced breakdown spectroscopy for geochemical and environmental analysis: A comprehensive review. *Spectrochimica Acta Part B: Atomic Spectroscopy*, 87, 11-26.
- Hasselmann, D. P. H. (1978). Effect of Cracks on Thermal Conductivity. *Journal of Composite Materials*, 12(4), 403-407.

- Hatanaka, K., Yomogihata, K. I., Ono, H., Nagafuchi, K., Fukumura, H., Fukushima, M., & Misawa, H. (2008). Hard X-ray generation using femtosecond irradiation of PbO glass. *Journal of Non-Crystalline Solids*, 354(52-54), 5485-5490.
- Hertel, I. V., Stoian, R., Ashkenasi, D., Rosenfeld, A., & Campbell, E. E. (2001). On the physics of material processing with femtosecond lasers. *Riken Review*, 23-30.
- Hopkins, M. B., & Graham, W. G. (1986). Langmuir probe technique for plasma parameter measurement in a medium density discharge. *Review of Scientific Instruments*, 57(9), 2210-2217.
- Hsu, W. H., Masim, F. C. P., Porta, M., Nguyen, M. T., Yonezawa, T., Balytis, A., & Hatanaka, K. (2016). Femtosecond laser-induced hard X-ray generation in air from a solution flow of Au nano-sphere suspension using an automatic positioning system. *Optics Express*, 24(18), 19994-20001.
- Ilyas, B., Dogar, A. H., Ullah, S., Mahmood, N., & Qayyum, A. (2012). Multiply charged ion emission from laser produced tungsten plasma. *Laser and Particle Beams*, 30(04), 651-657.
- Ishikawa, T., Aoyagi, H., Asaka, T., Asano, Y., Azumi, N., Bizen, T., Kumagai, N. (2012). A compact X-ray free-electron laser emitting in the sub-ngstrm region. *Nature Photonics*, 6, 540-544.
- Kajita, S, Ohno, N., & Takamura, S. (2006). Effects of transient heat load on tungsten surface having sub-micron helium holes and bubbles. *33rd EPS Conference on Plasma Physics 2006*, EPS 2006 (Vol. 3).
- Kajita, Shin, Kawaguchi, S., Ohno, N., & Yoshida, N. (2018). Enhanced growth of large-scale nanostructures with metallic ion precipitation in helium plasmas. *Scientific Reports*, 8(1), 56.
- Kajita, Shin, Ohno, N., Takamura, S., Sakaguchi, W., & Nishijima, D. (2007). Plasma-assisted laser ablation of tungsten: Reduction in ablation power threshold due to bursting of holes/bubbles. *Applied Physics Letters*, 91(26), 261501.

References

- Keldysh, L. V. (1965). Ionization in the field of a strong electromagnetic wave. *Sov. Phys. JETP*, 20(5), 1307-1314.
- Kelly, R., & Miotello, A. (1997). On the mechanisms of target modification by ion beams and laser pulses. *Nuclear Instruments and Methods in Physics Research Section B: Beam Interactions with Materials and Atoms*, 122, 374-400.
- Konjevi, N., Ivkovi, M., & Sakan, N. (2012). Hydrogen Balmer lines for low electron number density plasma diagnostics. *Spectrochimica Acta Part B: Atomic Spectroscopy*, 76, 16-26.
- Kruer, W. L. (1988). The Physics of Laser Plasma Interactions. *Addison-Wesley*, 45, 135.
- Kruer, W., & Estabrook, K. (1976). Laser-light absorption with self-generated magnetic-fields. *Bulletin of the American Physical Society*, 21(4), 597-597.
- Kulcsr, G., Al Mawlawi, D., Budnik, F. W., Herman, P. R., Moskovits, M., Zhao, L., & Marjoribanks, R. S. (2000). Intense picosecond x-ray pulses from laser plasmas by use of nanostructured "velvet" targets. *Physical Review Letters*, 84(22), 5149-5152.
- Labaune, C., Baccou, C., Depierreux, S., Goyon, C., Loisel, G., Yahia, V., & Rafelski, J. (2013). Fusion reactions initiated by laser-accelerated particle beams in a laser-produced plasma. *Nature Communications*, 4(1), 2506.
- Labutin, T. A., Lednev, V. N., Ilyin, A. A., & Popov, A. M. (2016). Femtosecond laser-induced breakdown spectroscopy. *J. Anal. At. Spectrom.*, 31(1), 90-118.
- Leitz, K.-H., Redlingshfer, B., Reg, Y., Otto, A., & Schmidt, M. (2011). Metal Ablation with Short and Ultrashort Laser Pulses. *Physics Procedia*, 12, 230-238.
- Lewis, L. J., & Perez, D. (2009). Laser ablation with short and ultrashort laser pulses: Basic mechanisms from molecular-dynamics simulations. *Applied Surface Science*, 255(10), 5101-5106.

-
- Li, M., Werner, E., & You, J.-H. (2015). Cracking behavior of tungsten armor under ELM-like thermal shock loads: A computational study. *Nuclear Materials and Energy*, 2, 1-11.
- Link, S., Wang, Z. L., & El-Sayed, M. A. (1999). Alloy Formation of Gold-Silver Nanoparticles and the Dependence of the Plasmon Absorption on Their Composition. *The Journal of Physical Chemistry B*, 103(18), 3529-3533.
- Lu, Y. F., Hong, M. H., & Low, T. S. (1999). Laser plasma interaction at an early stage of laser ablation. *Journal of Applied Physics*, 85(5), 2899.
- Mafun, F., Kohno, J. Y., Takeda, Y., & Kondow, T. (2001). Dissociation and aggregation of gold nanoparticles under laser irradiation. *The Journal of Physical Chemistry B*, 105(38), 9050-9056.
- Maiman, T. H. (1960). Stimulated optical radiation in Ruby. *Nature*, 187, 493-494.
- Malka, V., Faure, J., Gauduel, Y. A., Lefebvre, E., Rousse, A., & Phuoc, K. T. (2008). Principles and applications of compact laser-plasma accelerators. *Nature Physics*, 4(6), 447-453.
- Margetic, V., Pakulev, A., Stockhaus, A., Bolshov, M., Niemax, K., & Hergenrder, R. (2000). A comparison of nanosecond and femtosecond laser-induced plasma spectroscopy of brass samples. *Spectrochimica Acta Part B: Atomic Spectroscopy*, 55, 1771-1785.
- Marine, W., Gerri, M., Scotto d'Aniello, J. M., Sentis, M., Delaporte, P., Forestier, B., & Fontaine, B. (1992). Analysis of the plasma expansion dynamics by optical time-of-flight measurements. *Applied Surface Science*, 54, 264-270.
- Masim, F. C. P., Porta, M., Hsu, W. H., Nguyen, M. T., Yonezawa, T., Balytis, A., Juodkazis, S., et al. (2016). Au Nanoplasma as Efficient Hard X-ray Emission Source. *ACS Photonics*, 3(11), 2184-2190.
- McKenna, P., Neely, D., Bingham, R., & Jaroszynski, D. (Eds.). (2013). *Laser-Plasma Interactions and Applications*. Switzerland: Springer International Publishing.
-

References

- Miotello, A., & Kelly, R. (1995). Critical assessment of thermal models for laser sputtering at high fluences. *Applied Physics Letters*, 67, 3535-3537.
- Momma, C., Chichkov, B. N., Nolte, S., von Alvensleben, F., Tnnermann, A., Welling, H., & Wellegehausen, B. (1996). Short-pulse laser ablation of solid targets. *Optics Communications*, 129, 134-142.
- Mourou, G., & Umstadter, D. (1992). Development and applications of compact high-intensity lasers. *Physics of Fluids B: Plasma Physics*, 4, 2315-2325.
- Murnane, M. M., Kapteyn, H. C., Gordon, S. P., Bokor, J., Glytsis, E. N., & Falcone, R. W. (1993). Efficient coupling of high-intensity subpicosecond laser pulses into solids. *Applied Physics Letters*, 62(10), 1068-1070.
- Nagel, D. J., Burkhalter, P. G., Dozier, C. M., Holzrichter, J. F., Klein, B. M., McMahon, J. M., ... Whitlock, R. R. (1974). X-Ray Emission from Laser-Produced Plasmas. *Physical Review Letters*, 33, 743-746.
- Ni, X., Anoop, K. K., Wang, X., Paparo, D., Amoruso, S., & Bruzzese, R. (2014). Dynamics of femtosecond laser-produced plasma ions. *Applied Physics A: Materials Science and Processing*, 117(1), 111-115.
- Nishikawa, T., Nakano, H., Oguri, K., Uesugi, N., Nakao, M., Nishio, K., & Masuda, H. (2001). Nanocylinder-array structure greatly increases the soft X-ray intensity generated from femtosecond laser-produced plasma. *Applied Physics B: Lasers and Optics*, 73(2), 185-188.
- Nishimura, H., Endo, T., Shiraga, H., Kato, Y., & Nakai, S. (1993). Xray emission from high Z mixture plasmas generated with intense blue laser light. *Applied Physics Letters*, 62, 1344-1346.
- Nolte, S., Momma, C., Jacobs, H., Tnnermann, A., Chichkov, B. N., Wellegehausen, B., & Welling, H. (1997). Ablation of metals by ultrashort laser pulses. *Journal of the Optical Society of America B*, 14, 2716.

- Oraevsky, A. A., Da Silva, L. B., Rubenchik, A. M., Feit, M. D., Glinsky, M. E., Perry, M. D., Stuart, B. C. (1996). Plasma mediated ablation of biological tissues with nanosecond-to-femtosecond laser pulses: relative role of linear and nonlinear absorption. *IEEE Journal of Selected Topics in Quantum Electronics*, 2, 801-809.
- Oraevsky, A. A., Da Silva, L. B., Rubenchik, A. M., Feit, M. D., Glinsky, M. E., Perry, M. D., Mammini, B. M., et al. (1996). Plasma mediated ablation of biological tissues with nanosecond-to-femtosecond laser pulses: relative role of linear and nonlinear absorption. *IEEE Journal of Selected Topics in Quantum Electronics*, 2(4), 801-809.
- Palastro, J. P., Shaw, J. G., Follett, R. K., Colatis, A., Turnbull, D., Maximov, A. V., Goncharov, V. N., et al. (2018). Resonance absorption of a broadband laser pulse. *Physics of Plasmas*, 25(12), 123104.
- Pearlman, J. S. (1977). Faraday cups for laser plasmas. *Review of Scientific Instruments*, 48(8), 1064-1067.
- Pert, G. J. (1974). Thermal conduction effects in laser solid target interaction. *Plasma Physics*, 16, 1019-1033.
- Popruzhenko, V. S. (2014). Keldysh theory of strong field ionization: history, applications, difficulties and perspectives. *Journal of Physics B: Atomic, Molecular and Optical Physics*, 47, 204001.
- Protopapas, M., Keitel, C. H., & Knight, P. L. (1997). Atomic physics with super-high intensity lasers. *Reports on Progress in Physics*, 60, 389-486.
- Radtke, R., Biedermann, C., Schwob, J. L., Mandelbaum, P., & Doron, R. (2001). Line and band emission from tungsten ions with charge $2 1 +$ to $4 5 +$ in the $45 7 0 \text{ \AA}$ range. *Physical Review A*, 64(1), 012720.
- Rajeev, P. P., Ayyub, P., Bagchi, S., & Kumar, G. R. (2004). Nanostructures, local fields, and enhanced absorption in intense light-matter interaction. *Optics Letters*, 29(22), 2662.

References

- Rao, K. H., Smijesh, N., Nivas, J. J., & Philip, R. (2016). Ultrafast laser produced zinc plasma: Stark broadening of emission lines in nitrogen ambient. *Physics of Plasmas*, 23(4), 043503.
- Rischel, C., Rouse, A., Uschmann, I., Albouy, P.-A., Geindre, J.-P., Audebert, P., Gauthier, J.-C., et al. (1997). Femtosecond time-resolved X-ray diffraction from laser-heated organic films. *Nature*, 390(6659), 490-492.
- Roth, J., Tsitrone, E., Loarer, T., Philipps, V., Brezinsek, S., Loarte, A., Counsell, G. F., et al. (2008). Tritium inventory in ITER plasma-facing materials and tritium removal procedures. *Plasma Physics and Controlled Fusion*, 50(10), 103001.
- Rouse, A., Ta Phuoc, K., Shah, R., Pukhov, A., Lefebvre, E., Malka, V., Kiselev, S., et al. (2004). Production of a keV X-ray beam from synchrotron radiation in relativistic laser-plasma interaction. *Physical Review Letters*, 93(13), 1-4.
- Rumsby, P. T., & Paul, J. W. M. (1974). Temperature and density of an expanding laser produced plasma. *Plasma Physics*, 16(3), 247-260.
- Rundquist, A., Durfee, C. G., Chang, Z., Herne, C., Backus, S., Murnane, M. M., & Kapteyn, H. C. (1998). Phase-matched generation of coherent soft X-rays. *Science*, 280, 1412-1415.
- Russo, R E, Mao, X., Gonzalez, J. J., & Yoo, J. (2013). Femtosecond vs. Nanosecond laser pulse duration for laser ablation chemical analysis. *Spectroscopy (Santa Monica)*, 28.
- Russo, Richard E. (1995). Laser Ablation. *Applied Spectroscopy*, 49(9), 14A-28A.
- Sadrolhosseini, A. R., Noor, A. S. M., & Moksini, M. M. (2012). Application of surface plasmon resonance based on a metal nanoparticle. *Plasmonics-Principles and Applications*. IntechOpen.
- Sankar, P., Shashikala, H. D., & Philip, R. (2018). Ion dynamics of a laser produced aluminium plasma at different ambient pressures. *Applied Physics A: Materials Science and Processing*, 124(1), 1-7.

- Sarkar, A., & Singh, M. (2017). Laser-induced plasma electron number density: Stark broadening method versus the Saha Boltzmann equation. *Plasma Science and Technology*, 19(2), 1-9.
- Sharma, A. K., & Thareja, R. K. (2005). Plume dynamics of laser-produced aluminum plasma in ambient nitrogen. *Applied surface science*, 243(1-4), 68-75.
- Singh, J. P., & Thakur, S. N. (2007). *Laser-induced breakdown spectroscopy*. Elsevier.
- Strickland, D., & Mourou, G. (1985). Compression of amplified chirped optical pulses. *Optics Communications*, 56, 219-221.
- Tsibidis, G. D., Barberoglou, M., Loukakos, P. A., Stratakis, E., & Fotakis, C. (2012). Dynamics of ripple formation on silicon surfaces by ultrashort laser pulses in subablation conditions. *Physical Review B - Condensed Matter and Materials Physics*, 86(11).
- Turkevich, J. (1985). Colloidal gold. *Part I. Gold Bulletin*, 18(3), 86-91.
- Verhoff, B., Harilal, S. S., & Hassanein, A. (2012). Angular emission of ions and mass deposition from femtosecond and nanosecond laser-produced plasmas. *Journal of Applied Physics*, 111(12), 123304.
- Welch, A. J., Motamedi, M., Rastegar, S., LeCarpentier, G. L., & Jansen, D. (1991). Laser thermal ablation. *Photochemistry and Photobiology*, 53, 815-823.
- Whitty, W., & Mosnier, J.-P. (1998). Diagnostic of an expanding laser-produced lithium plasma using ICCD frame photography and shadowgraphy. *Applied Surface Science*, 127-129, 1035-1040.
- Woowski, J., Celona, L., Ciavola, G., Gammino, S., Krsa, J., Lska, L., Parys, P., et al. (2002). Expansion of tungsten ions emitted from laser-produced plasma in axial magnetic and electric fields. *Laser and Particle Beams*, 20(1), 113-118.
- Wu, D., Sun, L., Liu, J., Yu, X., Hai, R., Feng, C., Wang, Z., et al. (2019). Dynamics of prompt electrons, ions, and neutrals of nanosecond laser ablation of tungsten investigated using optical emission. *Physics of Plasmas*, 26(1), 013303.

References

- Wu, D., Zhang, L., Liu, P., Sun, L., Hai, R., & Ding, H. (2017). Diagnostic study of laser-produced tungsten plasma using optical emission spectroscopy and time-of-flight mass spectroscopy. *Spectrochimica Acta Part B: Atomic Spectroscopy*, 137, 70-76.
- Yaln, ., Tsui, Y. Y., & Fedosejevs, R. (2004). Pressure dependence of emission intensity in femtosecond laser-induced breakdown spectroscopy. *Journal of Analytical Atomic Spectrometry*, 19(10), 1295-1301.
- Yoshida, N. (1999). Review of recent works in development and evaluation of high-Z plasma facing materials. *Journal of Nuclear Materials*, 266-269, 197-206.
- Zeng, X., Mao, X. L., Greif, R., & Russo, R. E. (2005). Experimental investigation of ablation efficiency and plasma expansion during femtosecond and nanosecond laser ablation of silicon. *Applied Physics A*, 80, 237-241.
- Zhang, Z., VanRompay, P. A., Nees, J. A., & Pronko, P. P. (2002). Multi-diagnostic comparison of femtosecond and nanosecond pulsed laser plasmas. *Journal of Applied Physics*, 92, 2867-2874.
- Zhi-Hua, L., Duan-Ming, Z., Bo-Ming, Y., & Li, G. (2002). Characteristics of Plasma Shock Waves Generated in the Pulsed Laser Ablation Process. *Chinese Physics Letters*, 19(12), 1841-1843.
- Zieliska, A., Skwarek, E., Zaleska, A., Gazda, M., & Hupka, J. (2009). Preparation of silver nanoparticles with controlled particle size. *Procedia Chemistry*, 1(2), 1560-1566.

Pranitha Sankar

Contact Information:

Research Assistant,
Ultrafast and Nonlinear Optics Lab,
LAMP Group, Raman Research Institute (RRI),
Bangalore-560080, India.
Email: pranithasankar@gmail.com, pranitha@rri.res.in
Mobile: +91-9483002005

Research Interests:

Laser Induced Plasma diagnostics, Intense Laser-matter Interactions, Laser Induced Breakdown Spectroscopy, and Laser Induced Surface Structuring.

Education:

Ph.D. in Physics July 2015 - Till Date
National Institute of Technology Karnataka, Suratkal, India.

Thesis Title : **Multidiagnostic Characterization of Ultrashort and Short Pulse Laser Produced Plasma from Aluminium and Tungsten Targets.**
Advisor : Dr. H. D. Shashikala, Professor, NITK, Suratkal and Dr. Reji Philip, Professor, RRI, Bangalore.

Master of Science in Physics, 2013 CGPA: 3.09/4.00
University of Calicut, Kerala, India.

Bachelor of Science in Physics, 2011 Percentage: 84.60%
University of Calicut, Kerala, India.

Class XII, 2008 Percentage: 85.50%
Board of Higher Secondary Examinations, Kerala, India.

Class X, 2006 Percentage: 86.50%
Board of Public Examinations, Kerala, India.

Professional Experience:

- **Research Assistant** 01st April 2019 - Till Date
Raman Research Institute (RRI), Bangalore, India.
- **Research Assistant** 16th May 2016 - 30th September 2018
Raman Research Institute (RRI), Bangalore, India.
- **Senior Research Fellow** 25th July 2014 - 30th November 2015
Raman Research Institute (RRI), Bangalore, India.
- **Visiting Student** 10th March 2013 - 31st May 2014
Raman Research Institute (RRI), Bangalore, India.

Awards/Honours:

- **Best Poster Award in Ultrafast Science Conference**
University of Hyderabad, Andhra Pradesh, India, 2017.

Journal Publications: (Peer Reviewed)

- **Sankar, P.**, Thomas, J., Shashikala, H. D., & Philip, R. (2019). Enhanced bremsstrahlung X-ray emission from Ag nanoparticles irradiated by ultrashort laser pulses. *Optical Materials*, 92, 30-35.
- **Sankar, P.**, Shashikala, H. D., & Philip, R. (2019). Effect of laser beam size on the dynamics of ultrashort laser-produced aluminum plasma in vacuum. *Physics of Plasmas*, 26(1), 013302.

- **Sankar, P.**, Shashikala, H. D., & Philip, R. (2018). Ion dynamics of a laser produced aluminium plasma at different ambient pressures. *Applied Physics A*, 124(1), 26.
- **Sankar, P.**, Nivas, J. J., Smijesh, N., Tiwari, G. K., & Philip, R. (2017). Optical emission and dynamics of aluminum plasmas produced by ultra-short and short laser pulses. *Journal of Analytical Atomic Spectrometry*, 32(6), 1177-1185.
- Perumbilavil, S., **Sankar, P.**, Priya Rose, T., & Philip, R. (2015). White light Z-scan measurements of ultrafast optical nonlinearity in reduced graphene oxide nanosheets in the 400-700 nm region. *Applied Physics Letters*, 107(5), 051104.
- Nair, A. K., Bhavitha, K. B., Perumbilavil, S., **Sankar, P.**, Rouxel, D., Kala, M. S & Kalarikkal, N. (2018). Multifunctional nitrogen sulfur co-doped reduced graphene oxideAg nano hybrids (sphere, cube and wire) for nonlinear optical and SERS applications. *Carbon*, 132, 380-393.
- Felscia, U. R., Rajkumar, B. J., Nidya, M., & **Sankar, P.** (2018). Electronic and Nonlinear Optical Properties of L-Histidine on Silver: A Theoretical and Experimental Approach. *The Journal of Physical Chemistry A*, 122(4), 1045-1052.
- Felscia, U. R., Rajkumar, B. J., **Sankar, P.**, Philip, R., & Mary, M. B. (2017). Optical nonlinearity and charge transfer analysis of pyrene adsorbed on silver: Computational and experimental investigations. *Spectrochimica Acta Part A: Molecular and Biomolecular Spectroscopy*, 184, 286-293.
- Perumbilavil, S., Sridharan, K., Koushik, D., **Sankar, P.**, Pillai, V. M., & Philip, R. (2017). Ultrafast and short pulse optical nonlinearity in isolated, sparingly sulfonated water soluble graphene. *Carbon*, 111, 283-290.
- Vineeshkumar, T. V., Raj, D. R., Prasanth, S., **Sankar, P.**, Unnikrishnan, N. V., Pillai, V. M., & Sudarsanakumar, C. (2016). Composition-dependent structural, Raman and nonlinear optical properties of PVA capped Zn_{1-x}Cd_xCu_yS quantum dots. *Optical Materials*, 58, 128-135.
- Tejkiran, P. J., Teja, M. B., Kumar, P. S. S., **Sankar, P.**, Philip, R., Naveen, S., ... & Rao, G. N. (2016). DA--D Synthetic approach for thienyl chalconesNLOa structure-activity study. *Journal of Photochemistry and Photobiology A: Chemistry*, 324, 33-39.
- Narendran, N. S., Soman, R., **Sankar, P.**, Arunkumar, C., & Chandrasekharan, K. (2015). Ultrafast and short pulse optical nonlinearities of meso-tetrakis-(2, 3, 5, 6-tetrafluoro-N, N, N-trimethyl-4-aniliniumyl) porphyrin and its metal complexes. *Optical Materials*, 49, 59-66.
- John, J. S., Sajan, D., Umadevi, T., Chaitanya, K., **Sankar, P.**, & Philip, R. (2015). Synthesis, crystal structure, vibrational spectral analysis and Z-scan studies of a new organic crystal N, N dimethylurea ninhydrin: A scaled quantum mechanical force field study. *Optical Materials*, 48, 233-242.
- Nidya, M., Umadevi, M., **Sankar, P.**, & Rajkumar, B. J. (2015). L-Glutamic acid functionalized silver nanoparticles and its nonlinear optical applications. *Journal of Materials Science: Materials in Electronics*, 26(6), 4124-4131.
- Nidya, M., Umadevi, M., **Sankar, P.**, Philip, R., & Rajkumar, B. J. (2015). L-Phenylalanine functionalized silver nanoparticles: photocatalytic and nonlinear optical applications. *Optical Materials*, 42, 152-159.

Conference Publications:

- **Pranitha Sankar**, Jyothis Thomas, Reji Philip, Enhancement of Bremsstrahlung X-Ray Emission from Femtosecond Laser Irradiated Metal Nanoparticles, Ultrafast Science (UFS)- 2017, UOH Hyderabad.
- Kavya H. Rao, N. Smijesh, **P. Sankar**, R. Philip, I. V. Litvinyuk and R. T. Sang, Angle-resolved X-ray emission spectroscopy of laser produced metal plasmas and alloys, 23rd Australian, Institute of Physics Congress (AIP Congress 2018), December 9-December 13, 2018, Perth, Western Australia.
- **Pranitha Sankar**, H. D. Shashikala, Reji Philip, Ion dynamics of laser produced aluminium plasma at different ambient pressure, International Conference on Laser Ablation (COLA -2017), September 2017
- **Pranitha Sankar**, H. D. Shashikala, Reji Philip, Expansion dynamics of aluminum ions in ultrashort plasma at different ambient pressures, National Laser Symposium 26 (NLS-26), December 2017
- **Pranitha Sankar**, H. D. Shashikala, S.S. Harilal, Reji Philip , Effect of beam spot size on the dynamics of ultrashort laser produced plasma generated in vacuum, The 45th IEEE International Conference on Plasma Science (ICOPS 2018).
- **Pranitha Sankar**, Reji Philip, Enhancement of X-ray Emission by Double-pulse Target Ablation in a Laser-produced Plasma, International Workshop on EUV and Soft X-Ray Sources held at Amsterdam, The Netherlands, and November 2016
- **Pranitha Sankar**, Jijil j j Nivas , N. Smijesh, Reji Philip , Fluence Dependent Studies of Laser Produced Plasma Generated by Ultrashort and Short Laser Pulses, ICMST 2016 - St. Thomas College, Pala, KERALA
- Pranitha Sankar, Jijil. J. J Nivas, N. Smijesh and Reji Philip, Nanosecond and Femtosecond laser Produced Aluminum Plasmas: A Comparative Study-International conference on Plasma & Nanotechnology- 2014
- Jemy James, **Pranitha Sankar**, K.N Anju, Reji Philip, N. K kalarikkal, Laser Assisted Synthesis of Silver Nanoparticles: A Green Approach , International conference on Plasma & Nanotechnology-2014
- P.Sreekanth, **Pranitha Sankar**, Priya Rose T and Reji Philip, Spectral dispersion of ultrafast optical limiting in reduced graphene oxide, DAE-BRNS Theme meeting for Ultrafast Science (UFS)- 2014, Manipal University, India.

Technical Skills:

- Expert in Mode-locked femtosecond laser (100 fs, Tsunami, Spectra-Physics) with regenerative amplifier (TSA-10, Spectra-Physics)
- Expert in Q-Switched Nd:YAG lasers (7 ns, Quanta-Ray, Spectra Physics; 5 ns, MiniLite, Continuum).
- Expert in 10 mW He-Ne laser (Research Electro-Optics Inc., USA)
- Expert in Digital storage oscilloscopes (DPO7354 & TDS 2014 from Tektronix; WaveAce 214 from LeCroy; DL 7100 from Yokogawa).
- Expert in Function generators (AFG 3022 from Tektronix, DS345 from Stanford Research Systems).
- Expert in Fiber optic CCD spectrometer (Avantes, AvaSpec 2048 and 2048-2).
- Expert in High-resolution Spectrometers (iHR 320, HORIBA Jobin Yvon, iStar CCD 334 - Andor (Oxford instruments))